NANO-ELECTRO-MECHANICAL SYSTEMS FABRICATED BY TIP-BASED NANOFABRICATION

BY

HUAN HU

DISSERTATION

Submitted in partial fulfilment of the requirements
for the degree of Doctor of Philosophy in Electrical and Computer Engineering
in the Graduate College of the
University of Illinois at Urbana-Champaign, 2014

Urbana, Illinois

Doctoral Committee:

Professor William P. King, Chair
Professor Brian T. Cunningham
Associate Professor Xiuling Li
Assistant Professor Daniel M. Wasserman

ABSTRACT

This dissertation explores the use of a heated AFM tip for fabrication of NEMS devices. Two critical challenges hindering TBN from NEMS fabrication are addressed in this thesis. First, we experimentally found out that polystyrene nanopatterns deposited by a heated AFM tip can serve directly as etch mask and transfer the nanopatterns to solid-state materials such as silicon and silicon oxide through one step of etching, solving the first challenge for NEMS device fabrication using TBN; second, we developed a process that makes this TBN method seamlessly compatible with conventional nanofabrication processes. Polystyrene nanopatterns deposited can serve together with optical lithography patterned mask and transfer both micropatterns defined by optical lithography and nanopatterns defined by the heated AFM tip to silicon.

After solving the two critical challenges, we demonstrated various types of silicon NEMS mechanical resonators such as single-clamped, double-clamped, wavy-shaped, spider-like and spiral-shaped using this TBN method with a heated AFM tip. Laser interferometer measurement on two NEMS resonators showed resonance frequencies of 1.2MHz and 2.2 MHz, close to the simulated resonance frequencies.

Moreover, we demonstrated PDMS nanofluidic channels with arbitrary shapes using this TBN method with a heated AFM tip. Both ion conductance measurement and fluorescence measurement confirmed the functionality of the TBN-fabrication nanofluidic channels.

Finally, we demonstrated a MESFET transistor using this TBN method with a heated AFM tip. MESFET devices with one, two, four and eight fins were fabricated, demonstrating the capability of this TBN method. I-V measurements proved the functionality of the transistor.

This thesis work demonstrated that TBN with a heated AFM tip held great potential in nanodevice fabrication due to its simplicity, robustness, flexibility and compatibility with

existing device nanofabrication process. For example, the whole TBN process takes place in ambient conditions and is very simple. And this TBN method is additive so that the heated AFM tip only deposits polymer where needed, thus only resulting in minimal contamination.

Future work should improve the throughput and scalability to make this TBN method commercially available for NEMS fabrication.

ACKNOWLEDGEMENTS

I would like to first thank my advisor, Prof. William King, for his patience, trust, support and guidance to me through my four years in his group. He has provided first-class research equipment and a productive research atmosphere for his students. I have been very fortunate and honored to be one of his students. I really appreciate the precious education I have received during the years working with him.

I also would like to thank my previous advisor, Prof. Mark A. Shannon (who passed away in 2012 because of ALS), for his encouragement and help to me during my difficult period. Without his help, I would not have had the opportunity to continue my academic pursuit in the US. His spirit will always inspire me in my life.

I also would like to thank Prof. Brian Cunningham, Prof. Xiuling Li and Prof. Daniel Wasserman for their generous support as my committee members.

I also would like to thank colleagues in the King and Shannon groups as well as members of collaborating groups. Special thanks to Dr. Glennys Mensing, Dr. Junghoon Yeom and Dr. Likun Zhu; and to my collaborators Dr. Parsian Mohseni, Chen Zhang, Dr. Xin Miao and Yue Zhuo; and to Suhas Somnath who has provided much technical support to me.

I also would like to thank my parents for their understanding, tolerance of my only two short visits to them within these 8 years, and support of my academic pursuit. They have given me a wonderful childhood and I am very grateful for being their son.

Finally, I would like to thank my wife Xin Chai for staying 7 years with me in the US, through all sorts of hardship and painful experience. She has made many sacrifices in support of my own academic pursuit. Without her support, I would not have had the courage and confidence to finish my PhD. I would also like to thank my son Dayou for coming into my

family just two months before my defense, bringing me so much joy that graduation stress seemed to disappear.

TABLE OF CONTENTS

Chapter 1: Introduction ... 1
1.1 Nano-Electro-Mechanical Systems ... 2
1.2 Existing Nanofabrication Methods for Fabricating NEMS Devices ... 3
1.3 Existing Methods of Tip-based Nanofabrication for Nanodevice Fabrication ... 11
1.4 Deposition of Polystyrene Using a Heated AFM Tip ... 17
1.5 References ... 18

Chapter 2: Fabrication of Arbitrarily-Shaped Silicon and Silicon Oxide Nanostructures Using Tip-based Nanofabrication ... 26
2.1 Introduction ... 26
2.2 Experiment and Results ... 27
2.3 Discussion ... 40
2.4 Conclusions ... 40
2.5 References ... 41

Chapter 3: Silicon Nano-Mechanical Resonators Fabricated Using Tip-based Nanofabrication ... 45
3.1 Introduction ... 45
3.2 Experiments and Results ... 46
3.3 Discussion ... 56
3.4 Conclusions ... 58
3.5 References ... 58

Chapter 4: Nanofluidic Channels of Arbitrary Shapes Fabricated By Tip-based Nanofabrication ... 63
4.1 Introduction ... 63
4.2 Experiment ... 64
4.3 Results and Discussion ... 70
4.4 Conclusions ... 74
4.5 References ... 75

Chapter 5: Silicon Metal-Semiconductor Field Effect Transistors Fabricated by Tip-based Nanofabrication ... 80
5.1 Introduction ... 80
5.2 Experiment ... 81
5.3 Results and Discussion ... 83
5.4 Conclusions ... 88
5.5 References ... 88

Chapter 6: Conclusions and Future Work ... 90
6.1 Future Work ... 90
6.2 References ... 93

CHAPTER 1: INTRODUCTION

Human society has benefited a lot from increased capability of manufacturing in smaller dimensions. For example, the capability of fabricating billions of nanometer scale transistors within several square-inches of CPU chip enables the widespread use of personal computers, smartphones and tablets; the capability of fabricating microfluidic channels enabled the realization of lab-on-chip technology that allows processing of tiny amounts of liquids, thus leading to shorter analyzing time, lower cost and reduced usage of biological samples.

Recently, the capability of fabricating nano-electro-mechanical systems (NEMS) has opened new possibilities in smaller mass sensing down to the single molecular level, smaller force sensing, and measurement of quantum effect. However, existing nanofabrication methods for NEMS devices suffer either from high cost or the difficulty of scaling up. A simple, rapid, scalable, and flexible nanofabrication method for NEMS fabrication is required. Tip-based nanofabrication (TBN) is a very good candidate technology for mass-production of NEMS devices due to its potential of scaling up, low cost, and the capability of fabricating arbitrary nanostructures with resolution down to several nanometers. However, two critical challenges exist that prevent the mass-production of NEMS devices using TBN. The first challenge is the difficulty of fabricating solid-state material nanostructures reliably; the second challenge is achieving seamless compatibility with existing nanofabrication process. As a result, no NEMS device has been demonstrated using TBN so far.

This thesis work addresses the above two critical challenges and demonstrates reliable fabrication of NEMS devices using a TBN process that is seamlessly compatible with current nanofabrication processes. This thesis work is an important step toward making TBN a commercially feasible fabrication method for mass-production of NEMS devices.

1.1 Nano-Electro-Mechanical Systems

Nano-electro-mechanical systems (NEMS) evolved from their preceding technology termed micro-electro-mechanical systems (MEMS). Over the last half century, MEMS technology has nurtured many exciting commercial technologies used in people's daily lives. For example, almost every car is equipped with a MEMS accelerometer for triggering airbags to save lives in car accidents; MEMS-based microphones with cost less than one dollar a piece are embedded in cellphones; huge arrays of tilting micro-mirrors form the essential components for projection display systems; MEMS-based printer heads enable low-cost ink-jet printers widely used in homes and offices. One essential reason for the commercial success of MEMS technology is that it can be fabricated using the planar microfabrication process existing in the semiconductor industry and thus can be integrated with the CMOS circuit to form a complete system of sensor and circuit.

From the last decade, with the advancement of nanofabrication technology, researchers have been exploring the capability provided by nanometer scale mechanical parts. For example, mechanical nano-resonators or NEMS resonators have been demonstrated with the capability of sensing small masses down to single molecular level [1], electrical charges [2], high-frequency signal processing [3], biological imaging [4] and quantum measurement [5-7]. Figure 1.1 shows two applications of NEMS resonators. Figure 1.1(a) shows the SEM images of the silicon-carbide NEMS resonator and Figure 1.1(b) shows the amplitude and the phase spectrum of the NEMS resonator indicating a resonance frequency around 429 MHz. This NEMS resonator was used for the detection of single molecules [8]. Figure 1.1(c) shows the resonance curves of NEMS resonators as shown in Figure 1.1(d) for signal processing. The resonance frequency reached 1 GHz within the range of microwave frequency [9].

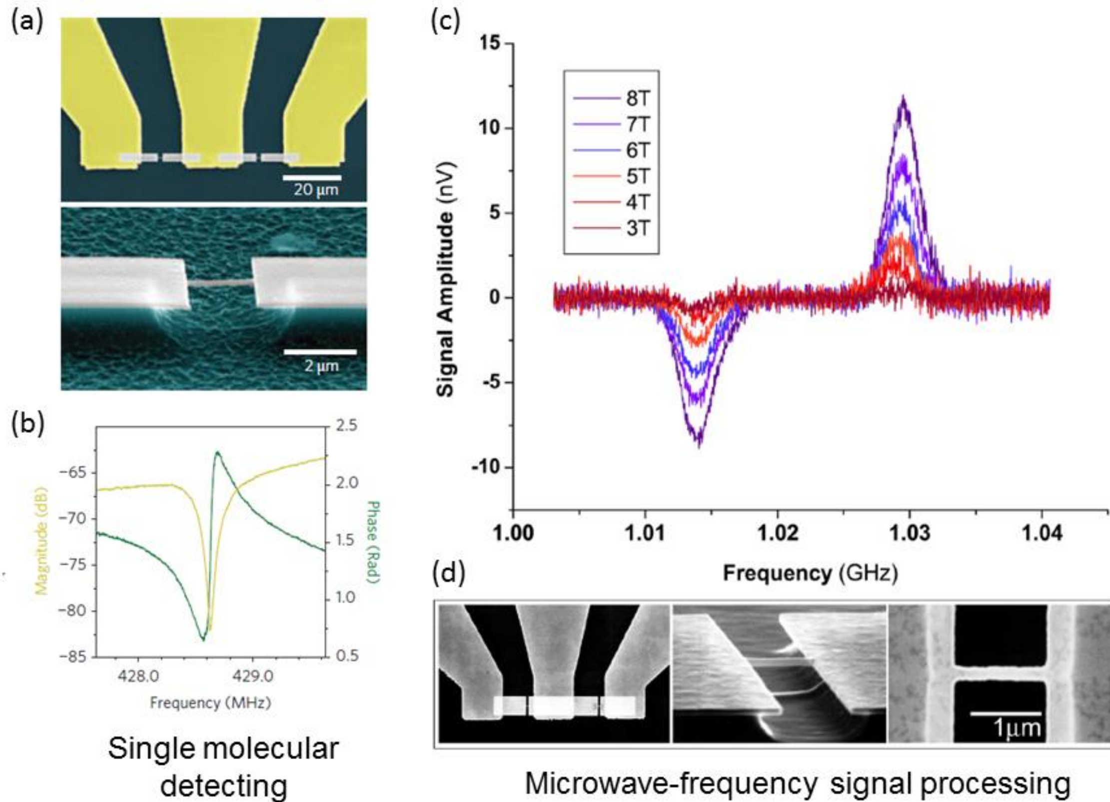

Figure 1.1 Examples of NEMS resonators and their resonance behaviors for single molecular detection and microwave-frequency signal processing.

1.2 Existing Nanofabrication Methods for Fabricating NEMS Devices

Existing nanofabrication methods for fabricating NEMS devices can be categorized into two classes. The first class is the top-down approach that evolves mostly from the conventional lithography technique, in which nanostructures are fabricated from a bulk material by gradually moving or subtracting materials in series [10]. The top-down approach can fabricate nanostructures precisely in terms of position, orientation and size. However, the top-down approach requires complex equipment and expensive maintenance. In addition, many challenges exist when the top-down method approaches its resolution limits. The bottom-up approach employs manipulation or synthesis of biochemistry in assembling nanometer scale building

blocks such as atoms, molecules, DNAs and nanoparticles into desired nanostructures. The bottom-up approach is low-cost and scalable, but it suffers from lack of precision and a low degree of control over the fabricated nanostructures.

Technologies in the top-down approach for NEMS device fabrication include electron beam lithography (EBL) [11-17], focused ion beam lithography (FIB) [18, 19] and nano-imprint lithography (NIL) [20]. The Craighead group has fabricated NEMS mechanical resonators using EBL combined with surface micromachining using the process as shown in Figure 1.2 [21]. The process started with nanopatterning poly(methyl methacrylate) (PMMA) resist layer on top of a silicon-on-insulator (SOI) wafer. Then metal deposition and lift-off were used to form metal nanopatterns. Then metal nanopatterns were transferred to silicon through etching to define resonator beams. After the silicon etching, buried oxide layer was etched to release the silicon resonator beams to form suspended beams. Finally, metal electrodes were deposited for applying oscillating electric bias to generate electrostatic forces for actuating the NEMS resonator. Figure 1.3 shows the SEM images of various types of NEMS resonators fabricated using this process, demonstrating the fabrication capability of EBL in fabricating complex structures for NEMS devices [22-24].

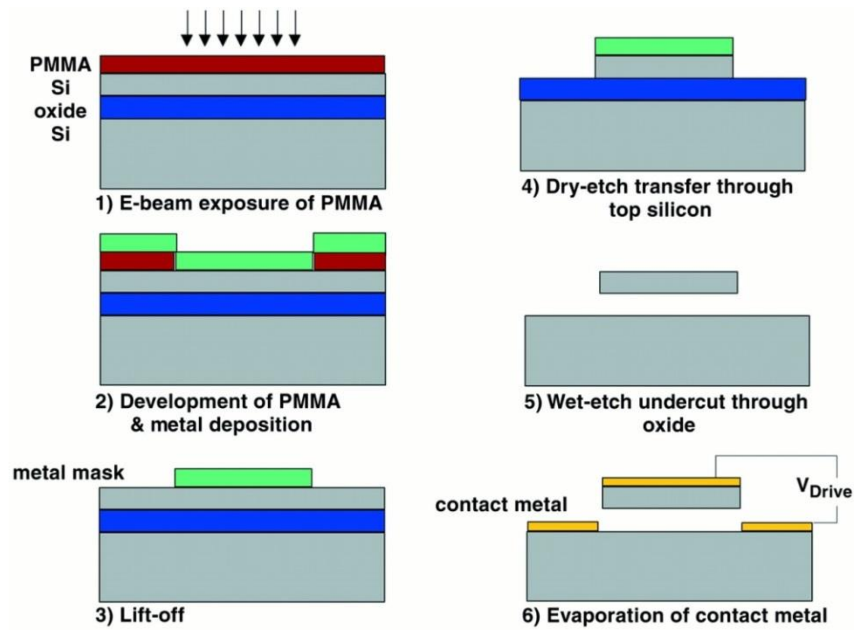

Figure 1.2 A typical fabrication process of NEMS mechanical resonator using EBL.

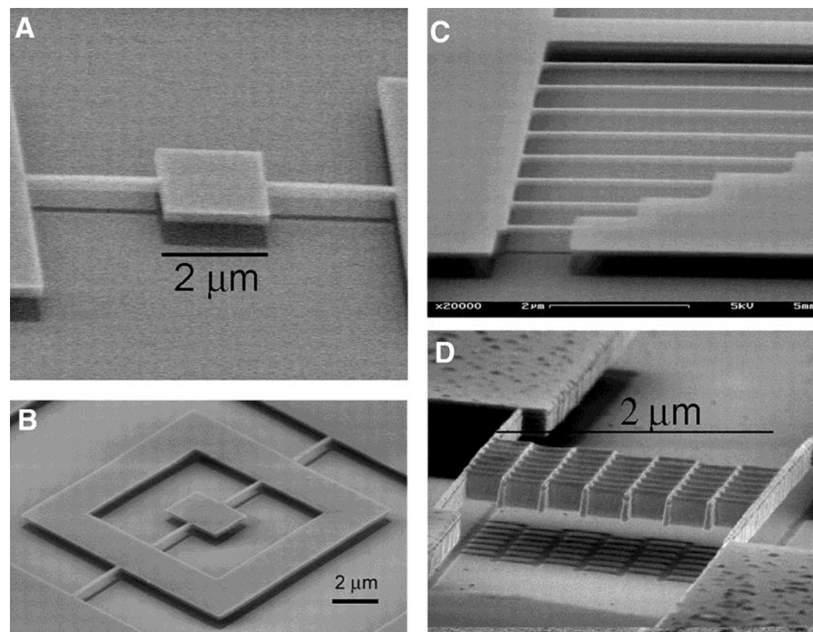

Figure 1.3 SEMs of NEMS resonators fabricated by EBL. (A) torsional NEMS resonator [22]; (B) a compound torsional resonator; (C) double-clamped NEMS resonator with different lengths [23]; (D) oscillating silicon nano mesh mirror [24].

Figure 1.4 shows a fabrication process for a three-terminal NEMS resonator fabricated using FIB as well as SEM images of FIB-fabricated NEMS resonator [25]. First, aluminum patterns were prepared on silicon substrate using conventional lithography and wet etching (step 1). Then SF_6 isotropic dry etching of silicon undercut the silicon underneath the aluminum film (step 2). Following the SF_6 etching, FIB cut a 9 nm wide gap to form a suspended aluminum beam (step 3). FIB was able to cut a gap as small as 9 nm as shown in the SEM image. Other than FIB milling, FIB can also implant impurity to silicon, which renders the implanted silicon region much less susceptible to chemical etching. NEMS resonators have also been demonstrated using this FIB doping method [26-28].

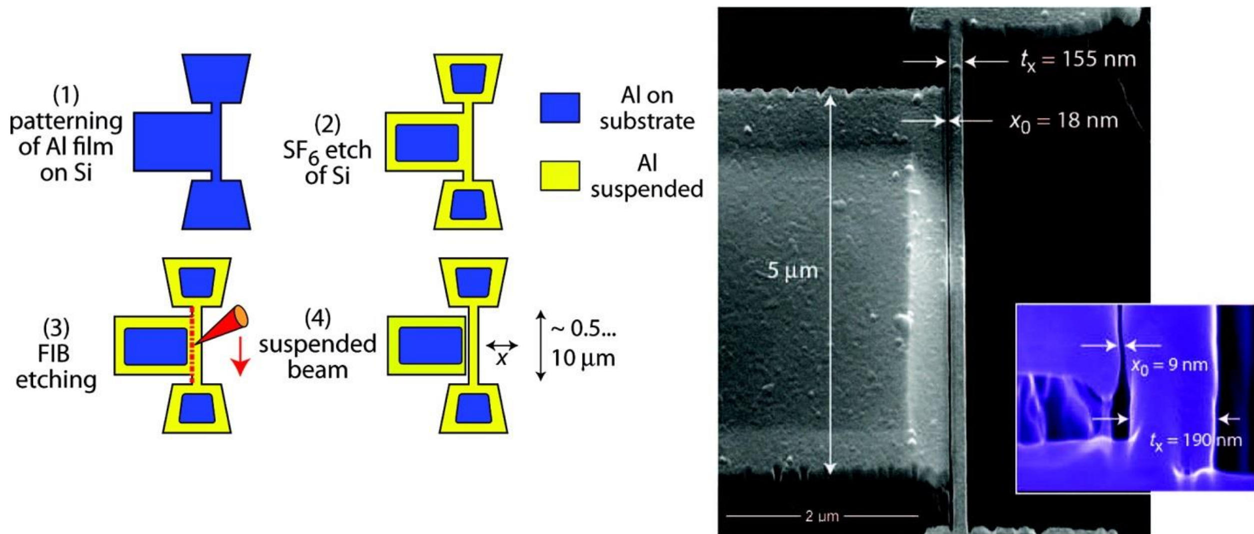

Figure 1.4 (a) Schematics showing the process of fabricating a three-terminal NEMS resonator using FIB. (b) SEM images of FIB-fabricated NEMS resonator.

Figure 1.5 shows a fabrication process of NEMS resonators using NIL as well as the SEM images of the NIL-fabricated NEMS resonator [29]. First, bilayers of PMMA and lift-off resist (LOR) 3A polymers were spincoated on a silicon carbonitride (SiCN) layer atop a silicon wafer (step a). Then a NIL mold pressed the polymer and replicated the pattern to the two

polymer films (step b). After the NIL process, oxygen plasma etched remaining films (step c). Then chrome was deposited and lifted off to form etch mask for silicon (step e). Dry etching of silicon removed silicon unprotected by the chrome mask and fabricated the SiCN beam (step f). Finally, SiCN beam was released from the substrate by anisotropic etching of silicon. Figure 1.5(h) shows a resonator beam with a width of 300 nm and Figure 1.5(i) shows a resonator beam with a width of 120 nm.

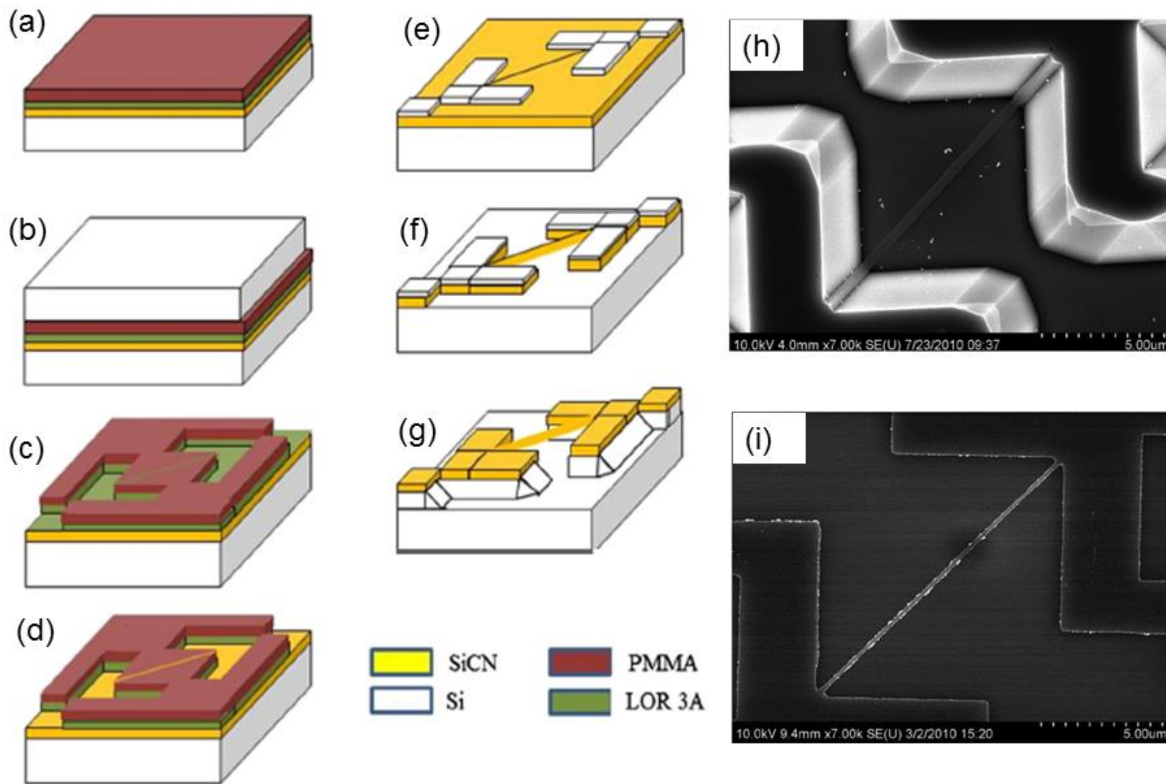

Figure 1.5 Schematics describing the processing steps of NIL-fabricated NEMS resonator (a to g); (h) SEM images of 300 nm wide NIL-fabricated NEMS resonator; (i) 120 nm wide NIL-fabricated NEMS resonator.

Bottom-up approaches have also demonstrated fabrication of NEMS resonators but with the help of top-down approach equipment for identifying and aligning the nanowires [30-32] or carbon nanotubes [33-35] to the anchors. A widely used method for using bottom-up approach is

to first prepare the nanowire or nanotube using synthesis or growth, then use EBL to locate them, and then fabricate electrodes to make connections. Figure 1.6 shows the schematics of this method [36]. First, EBL fabricated some markers on top of a sacrificial layer atop a substrate (step a); second, NWs were distributed over the sample surface randomly (step b); third, the sample was inspected in a EBL machine and electrode patterning areas were chosen, then exposed and developed, then metal was evaporated and lifted off (step c); fourth, a sacrificial layer underneath the NW was etched to suspend the NW (step d); Figure 1.6(e, f) show two SEM images of the NEMS resonators fabricated using this process. This bottom-up method has to rely on top-down equipment such as EBL for alignment, which makes it difficult to scale up.

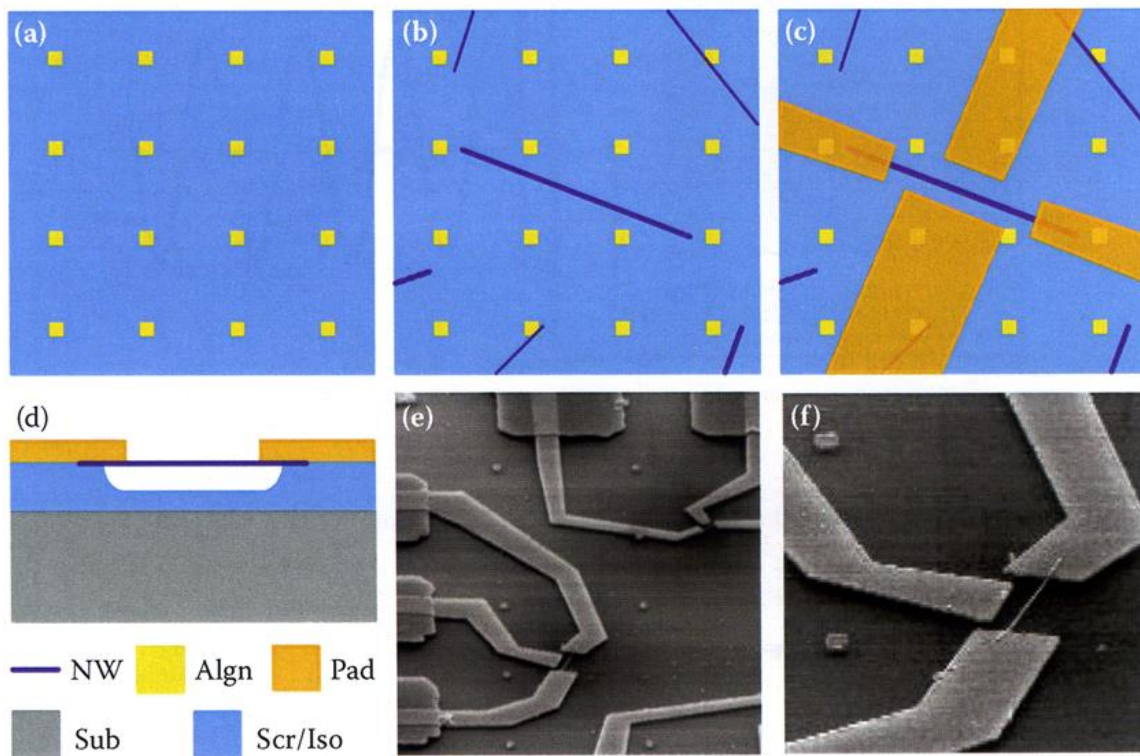

Figure 1.6 Fabrication process of NEMS resonator using nanowire and EBL: (a) EBL patterning markers on top of sacrificial layer; (b) NWs were distributed on the substrate and coordinates were identified; (c) EBL fabricating metal electrodes on sacrificial layer; (d) etching of sacrificial layer to release the resonator; (e, f) SEM images of the fabricated NEMS resonator.

The above method is not scalable. Recently, researchers have developed a scalable method fabricating NEMS resonators using a bottom-up approach. Figure 1.7 shows an example process of using bottom-up approach to assemble silicon nanowires for fabricating arrays of NEMS resonators [30]. First, PNA molecules were attached to the NW surface (step a); second, electric-field forces aligned the NWs in trenches prefabricated in a sacrificial photoresist layer (step b); third, conventional lithography method was used to fabricate individual windows on each NW (step c) and used oxygen plasma to etch all the way down to the electrode; fourth, metal clamps were electrodeposited through the windows to fix NWs to the electrode on the substrate (step d); fifth, NWs were exposed to fluorescence-labelled complementary and non-complementary targets to confirm detection selectivity. Figure 1.7(f to j) shows SEM images of NEMS resonators fabricated using this bottom-up approach. But this method can only fabricate NEMS resonators with very limited geometry. The resonator shape is limited to the straight shape predetermined by the nanowire or nanotube shape.

Other methods also have emerged for fabricating NEMS resonators. One example is nanostencil lithography [37, 38], which uses EBL-fabricated nano stencils to define nanopatterns functioning as a shadow mask. But it can only replicate predefined patterns in a serial process and requires expensive EBL to fabricate the stencils.

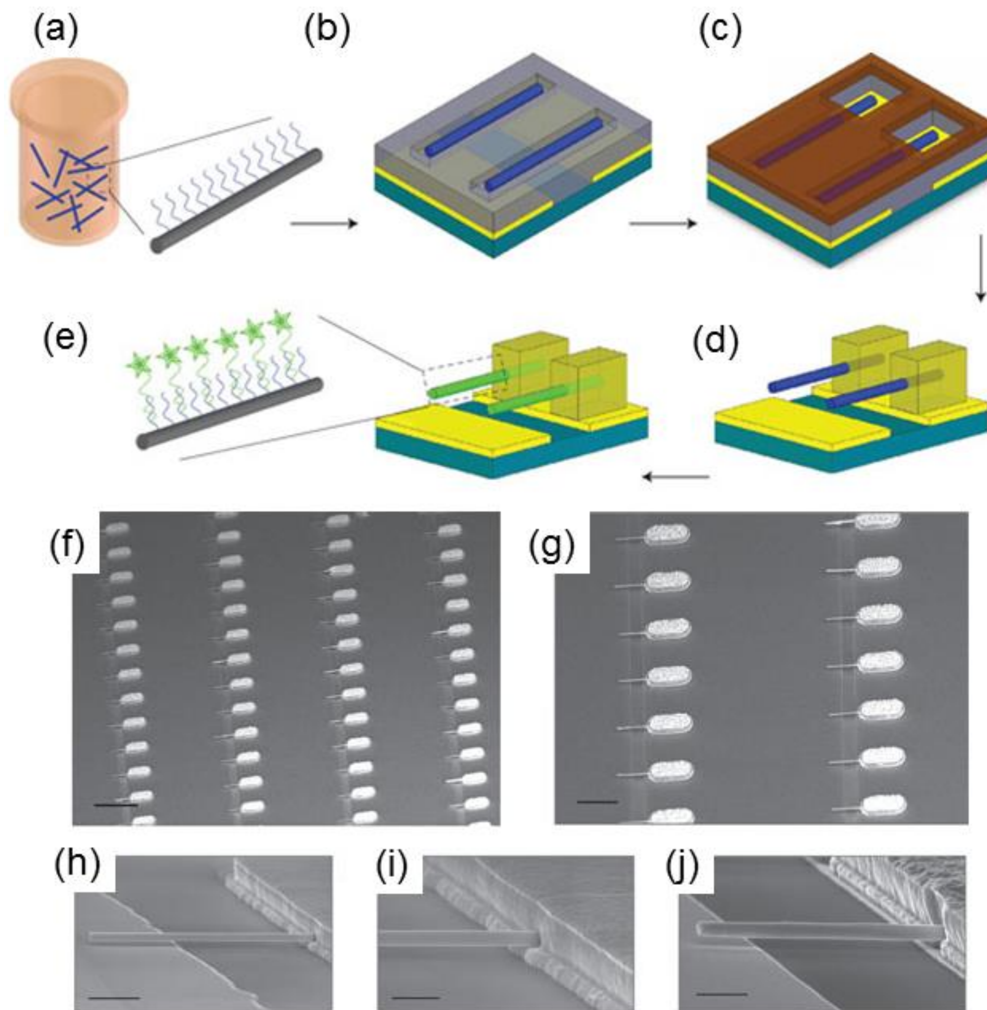

Figure 1.7 Schematics of fabrication process of large array of NEMS resonators using NIL (a to d); SEM images of NIL-fabricated NEMS resonators (f to j).

Overall, there is no method that can satisfy all the requirements for the commercialization of NEMS resonators. For commercialization of NEMS resonators, the fabrication method must be rapid, simple, scalable, low-cost, and flexible in design. Therefore, it is important to explore new fabrication method for NEMS resonators. Tip-based nanofabrication (TBN) has emerged for decades and has demonstrated many nanoscale devices. TBN uses a nanometer scale tip to fabricate nanometer scale features through a variety of mechanisms including mechanical, electrical, electro-chemical, thermal-mechanical, optical, plasma, etc. Table 1.1 compares TBN

with other nano-manufacturing technologies in terms of resolution, contamination, speed, scalability, flexibility, and cost [39]. Among the nano-manufacturing methods, TBN is scalable, low-cost and fast. And TBN can fabricate arbitrary patterns. Therefore, TBN holds great potential for mass-producing NEMS resonators for commercialization.

Table 1.1 Comparison of nano-manufacturing technologies.

Nano-manufacturing Technologies	Resolution & Materials	Defects & contamination	Type & Processing speed	Scalability	Cost	Design flexibility
TBN	<10-80nm; All materials	Occasional pile-up	Deposition, machining, assembly, Fast	Yes	Low	Arbitrary
EBL	5nm; All	Ebeam resist/ development residual	Machining; Slow	No	High	Arbitrary
FIB	30nm; All	Ion implantation and material redeposition	Machining; Slow	No	High	Arbitrary
NIL	10nm; polymers and silicon	Residual /contamination	Molding; Fast	Yes	Low in volume	Fixed
Femtosecond Laser machining	100 nm; all	Laser redeposition	Machining; Fast	Yes	High	Arbitrary
UV lithography	90nm; polymers	Photoresist/ development residual	Machining; Fast	Yes	High	Fixed
X-ray Lithography	1nm; all	No	Machining; Slow	No	High	Arbitrary

1.3 Existing Methods of Tip-based Nanofabrication for Nanodevice Fabrication

Although TBN is promising for creating NEMS devices, very few papers have been published on using TBN for fabricating nanoscale devices. Among all the TBN methods, there are mainly three classes that have been demonstrated with the capability of fabricating devices.

The first class of TBN method is based on electrochemical reaction induced locally by the tip. For example, nanoscale devices such as transistors [40-44] and nanogaps [45] have been fabricated using this type of TBN. For example, one method in this category termed local

oxidation nanolithography (LON) relies on oxidation of materials. LON uses a nanometer scale tip to induce confined oxidation of substrate material for nanopatterning. Figure 1.8 shows a process of fabricating transistors using LON. Transistors with channel width as small as 4 nm are demonstrated [41]. AFM tip converted a thin nanoline of silicon into silicon oxide through local oxidation of silicon (step a). Then the silicon oxide nanoline was used as an etch mask to fabricate silicon nanowire through KOH etching or RIE etching (step b). After etching, silicon oxide nanoline was removed by hydrofluoric acid (HF) etching, leaving only silicon nanowire (step c). Finally, EBL is used to precisely fabricate electrodes to configure the silicon nanowire into a transistor (step d or e). Figure 1.8(f) shows the optical microscopic photo of the transistor with three gold pads serving as the source, drain and gate electrodes. Figure 1.8(g) shows the amplitude modulation AFM image of the lateral gate electrode and the nanowire. Figure 1.8(h) shows the AFM cross-section of the region marked in panel b indicating the height of the electrode is 100 nm while the height of the silicon nanowire is about 40nm. Figure 1.8(i) shows the reconstruction of the SiNWs obtained from Figure 1.8(g); Figure 1.8(j) shows the output characteristics of a 4 nm channel width Si nanowire field-effect transistor.

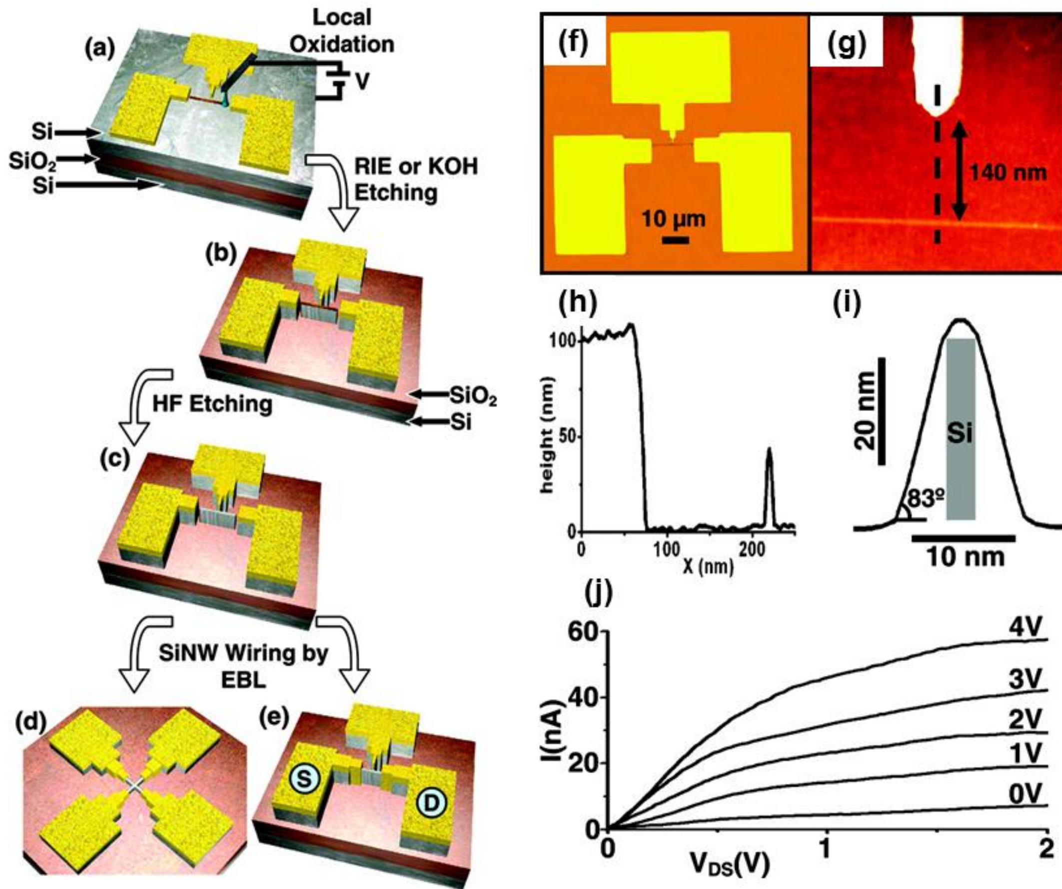

Figure 1.8 (a-e) Fabrication processes of FET device using LON; (f) Optical microscope image of FET device; (g) Amplitude AFM image of the device; (h) AFM cross-section of the region marked in panel b; (i) Reconstruction of the SiNWs obtained from panel c; (j) Output characteristics of a 4nm channel width SiNW field effect transistor.

The second class of TBN method is termed dip pen nanolithography (DPN) [46], which relies on chemical molecule diffusion through the meniscus formed between the tip and the substrate. Only limited types of substrates such as gold are demonstrated for DPN process because it requires specific surface chemistry to ensure stable formation of chemical nanopatterns on the substrate. Researchers have demonstrated fabrication of nanopatterns of gold (Au), silver (Ag), palladium (Pd) and silicon using DPN [47-49]. But the quality of these metal patterns was not reported thus it is not clear whether these fabricated nanostructures can be

used for constructing functional nanodevices. Figure 1.9(a-e) shows a fabrication process of silicon nanostructure using DPN. First, DPN deposited alkythiol nanopatterns onto an Au/Ti/SiO_2 substrate (step a); second, alkythiol nanopatterns served as etch mask to protect Au, Ti, and SiO_2 underneath during a series of wet chemical etching of Au, Ti and SiO_2 (step b). Then silicon etching was performed using the remaining Au as etch mask to form silicon nanostructures (step c and step d). Finally, Au, Ti, and SiO_2 were removed. Figure 1.9(f) shows a series of silicon nanodots with increasing diameters while Figure 1.9(g) shows a series of silicon nanolines with increasing widths.

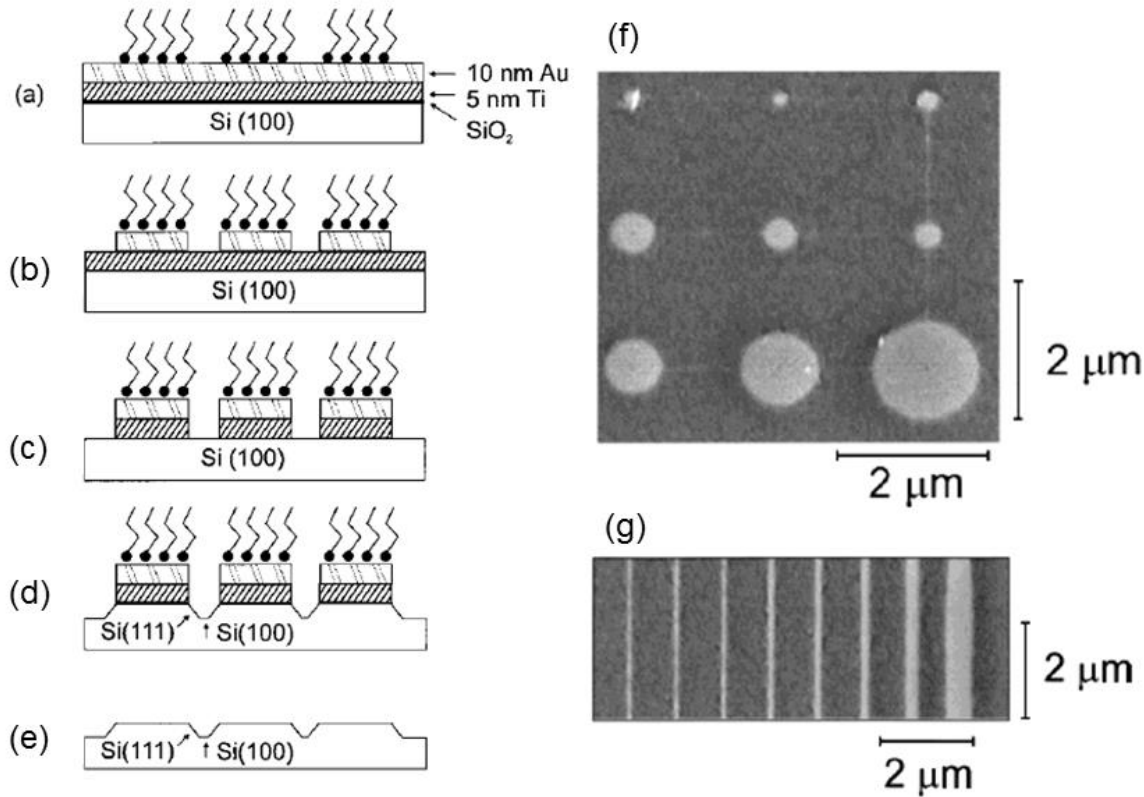

Figure 1.9 (a to e) Schematics showing silicon nanostructure fabrication using DPN; (f) AFM topography image of silicon nanodot structures with different diameters fabricated by DPN; (g) silicon nanowires with different widths fabricated by DPN.

The third class of TBN is mechanically based, in which an AFM tip mechanically fabricates nanopatterns on the substrate [50-54]. Figure 1.10(a) shows one process of fabricating chrome and silicon nanowires using this mechanical TBN method. First, an AFM tip mechanically plowed a trench through a 3 nm thick Ti film atop a 65 nm thick PMMA layer (step a). Then isotropic oxygen plasma etched through the Ti window down to the silicon substrate (step b). After plasma etching step, Cr was evaporated through the Ti/PMMA window and lift-off process followed to fabricate Cr nanowires (step c). Then SF_6 and O_2 reactive ion etching followed up to etch silicon unprotected by the Cr nanowires (step d). Finally, Cr was removed by wet etching and only silicon nanowires remained. Figure 1.10(b) shows SEM images of Cr nanowires as well as the silicon nanowires.

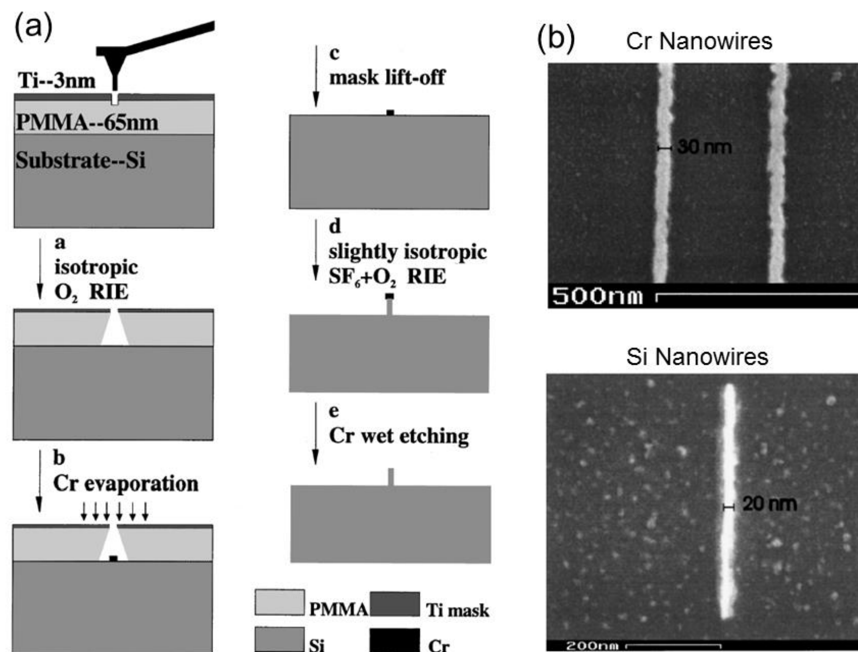

Figure 1.10 (a). Schematics showing the silicon nanostructure fabrication using mechanical AFM technique; (b) SEM images of fabricated Cr nanowires as well as silicon nanowires.

The fourth class of TBN is thermal-based [55], which uses a heated AFM tip to thermally indent a polymer film to form pits on the polymer [56-59], or thermally deposit molten polymer nanostructures onto a substrate [60-63] or low melting point metals [64], or thermally induce chemical reactions [65-69] to fabricate nanostructures. Figure 1.11 summarizes different nanostructures fabricated using heated AFM tips. Figure 1.11(a) shows a 40 nm size PMMA pit array with 120 nm pitch fabricated by thermal indentation of a heated AFM tip array; Figure 1.11(b) shows octadecylphosphonic acid patterns deposited onto a mica surface by a heated AFM tip; Figure 1.11(c) shows a topographical AFM image of a continuous indium metal nanostructure deposited by a heated AFM tip across a 500 nm wide gap (circled) between pre-fabricated gold electrodes; Figure 1.11(d) shows conductive polymer PDDT nanowires deposited by a heated AFM tip across two electrodes. Figure 1.11(e) shows ferroelectric nanolines fabricated by inducing local crystallization by a heated AFM tip; Figure 1.11(f) shows graphene nanoribbons reduced by a heated AFM tip on a single-layer graphite oxide flake;

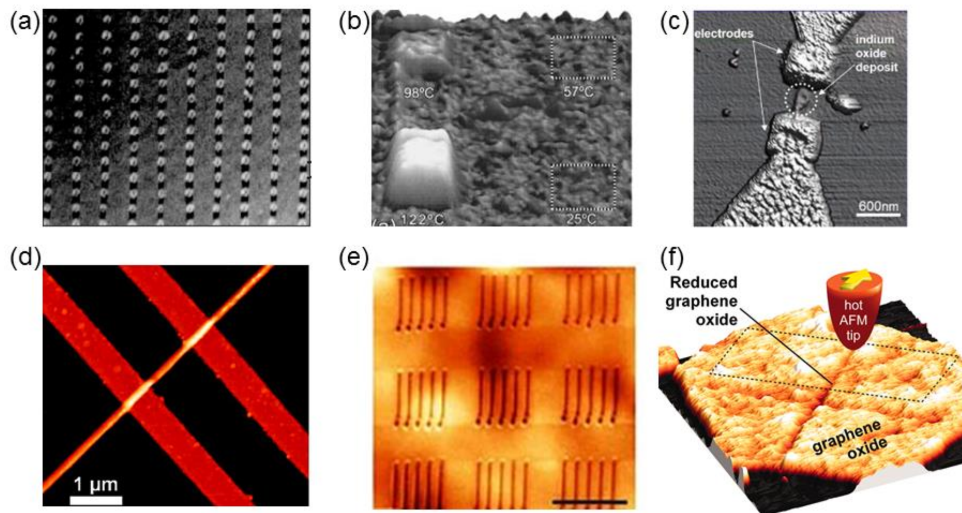

Figure 1.11 Various kinds of nanostructures fabricated using TBN with a heated AFM tip.

This thesis focuses on exploring the method of using heated AFM tip to deposit polymer for fabricating NEMS devices.

1.4 Deposition of Polystyrene Using a Heated AFM Tip

Figure 1.12(a, b) shows the diamond-coated AFM tip used for all the research work in this thesis. Diamond-coated heated AFM tip offers two advantages for depositing polystyrene (PS) over a normal silicon tip without diamond coating. First, the amorphous diamond film can keep the molten polystyrene in place because the diamond film surface has better affinity to the molten polystyrene; second, the diamond film protects the silicon tip from mechanical wear during polymer deposition, ensuring an integral tip radius and maintaining uniform polymer nanopattern sizes over much longer usage [70].

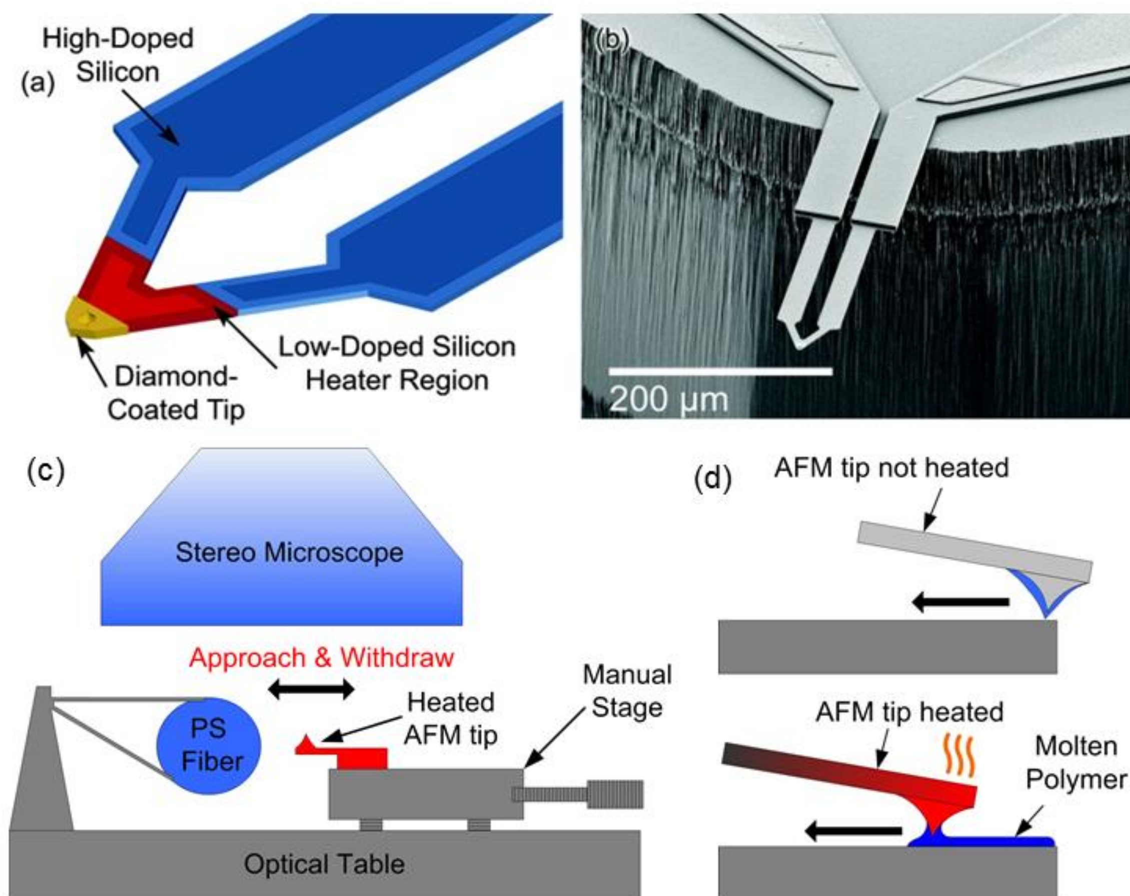

Figure 1.12 (a) Cartoon showing the formation of the diamond-coated AFM tip; (b) SEM image of a diamond-coated AFM tip; (c) Schematics showing the process of inking polystyrene on the heated AFM tip; (d) Cartoon showing the process of depositing polymer on a substrate using a heated AFM tip.

The first step of using heated AFM tip for depositing polymer is to add polymer materials on the tip, which can be achieved either using wet inking or solid inking. Solid inking method is used for all the work in this thesis. Figure 1.12(c) shows a cartoon describing the process of solid inking. We first placed a flake of polystyrene (molecular weight 50,000 Polyscience Inc.) on a glass slide and heated to 180 °C on a hotplate until the polymer started to melt. Then we used a metal wire to manually draw a fiber from the molten polystyrene and cut it into about 10 cm long fibers. After preparing the polystyrene fibers, we attached one end of a polystyrene fiber to a fixture. Then we brought a heated AFM tip into contact with the fiber under a stereo microscope with the help of a manipulator. Upon contact, the molten polymer would wet the heated tip, and then we withdrew the heated tip away from the fiber, completing the inking process.

Following inking, the AFM tip was fit into a commercial AFM (Asylum MFP-3D) and brought into contact with a substrate. The AFM tip was scanned along a programmed path with temperature maintained around 260°C using a closed-loop temperature control circuit. The molten polymer flowed to the substrate and became solid upon cooling by the substrate as shown in Figure 11(d).

1.5 References

[1] M. Hanay, et al., "Single-protein nanomechanical mass spectrometry in real time," Nature Nanotechnology, vol. 7, pp. 602-608, 2012.

[2] A. N. Cleland and M. L. Roukes, "A nanometre-scale mechanical electrometer," Nature, vol. 392, pp. 160-162, 1998.

[3] C. T. C. Nguyen, et al., "Micromachined devices for wireless communications," Proceedings of the IEEE, vol. 86, pp. 1756-1768, Aug 1998.

[4] J. A. Sidles, et al., "Magnetic-Resonance Force Microscopy," Reviews of Modern Physics, vol. 67, pp. 249-265, Jan 1995.

[5] A. Cho, "Physics - Researchers race to put the quantum into mechanics," Science, vol. 299, pp. 36-37, Jan 3 2003.

[6] M. Zhang, et al., "Quantum dynamics of a single cooper-pair box with a single-mode cavity field," International Journal of Modern Physics B, vol. 16, pp. 4767-4774, Dec 2012

[7] M. F. Bocko and R. Onofrio, "On the measurement of a weak classical force coupled to a harmonic oscillator: Experimental progress," Reviews of Modern Physics, vol. 68, pp. 755-799, Jul 1996.

[8] A. K. Naik, et al., "Towards single-molecule nanomechanical mass spectrometry," Nature Nanotechnology, vol. 4, pp. 445-450, Jul 2009.

[9] X. M. H. Huang, et al., "Nanodevice motion at microwave frequencies," Nature, vol. 421, pp. 496-496, Jan 30 2003.

[10] A. A. Tseng, Nanofabrication: fundamentals and applications: World Scientific, 2008.

[11] C. Vieu, et al., "Electron beam lithography: resolution limits and applications," Applied Surface Science, vol. 164, pp. 111-117, 2000.

[12] L. Sekaric, et al., "Nanomechanical resonant structures in nanocrystalline diamond," Applied Physics Letters, vol. 81, pp. 4455-4457, Dec 2 2002.

[13] L. Sekaric, et al., "Nanomechanical resonant structures in silicon nitride: fabrication, operation and dissipation issues," Sensors and Actuators a-Physical, vol. 101, pp. 215-219, Sep 30 2002.

[14] Y. T. Yang, et al., "Monocrystalline silicon carbide nanoelectromechanical systems," Applied Physics Letters, vol. 78, pp. 162-164, Jan 8 2001.

[15] B. Ilic, et al., "Virus detection using nanoelectromechanical devices," Applied Physics Letters, vol. 85, pp. 2604-2606, Sep 27 2004.

[16] A. N. Cleland, et al., "Single-crystal aluminum nitride nanomechanical resonators," Applied Physics Letters, vol. 79, pp. 2070-2072, Sep 24 2001.

[17] D. M. Tanenbaum, et al., "Dual exposure glass layer suspended structures: A simplified fabrication process for suspended nanostructures on planar substrates," Journal of Vacuum Science & Technology B, vol. 19, pp. 2829-2833, Nov-Dec 2001.

[18] R. L. Seliger, et al., "A high - intensity scanning ion probe with submicrometer spot size," Applied Physics Letters, vol. 34, pp. 310-312, 1979.

[19] J. Y. Chang, et al., "Synthesis and Bidirectional Frequency Tuning of Cantilever-Shape Nano Resonators Using a Focused Ion Beam," ACS Applied Materials & Interfaces, vol. 5, pp. 9684-9690, Oct 9 2013.

[20] S. Y. Chou, et al., "25-nanometer resolution," Science272, pp. 85-87, 1996.

[21] H. G. Craighead, "Nanoelectromechanical systems," Science, vol. 290, pp. 1532-1535, 2000.

[22] S. Evoy, et al., "Nanofabrication and electrostatic operation of single-crystal silicon paddle oscillators," Journal of Applied Physics, vol. 86, pp. 6072-6077, 1999.

[23] D. W. Carr, et al., "Measurement of mechanical resonance and losses in nanometer scale silicon wires," Applied Physics Letters, vol. 75, pp. 920-922, 1999.

[24] D. W. Carr, et al., "Measurement of nanomechanical resonant structures in single-crystal silicon," Journal of Vacuum Science and Technology B, vol. 16, pp. 3821-3824, 1998.

[25] J. Sulkko, et al., "Strong Gate Coupling of High-Q Nanomechanical Resonators," Nano Letters, vol. 10, pp. 4884-4889, Dec 2010.

[26] A. J. Steckl, et al., "Localized Fabrication of Si Nanostructures by Focused Ion-Beam Implantation," Applied Physics Letters, vol. 60, pp. 1833-1835, Apr 13 1992.

[27] J. Brugger, et al., "Silicon micro/nanomechanical device fabrication based on focused ion beam surface modification and KOH etching," Microelectronic Engineering, vol. 35, pp. 401-404, Feb 1997.

[28] P. Sievila, et al., "The fabrication of silicon nanostructures by focused-ion-beam implantation and TMAH wet etching," Nanotechnology, vol. 21, Apr 9 2010.

[29] A. Janzen, et al., "Fabrication of nanoresonator biosensing arrays using nanoimprint lithography," Journal of Micro-Nanolithography Mems and Moems, vol. 11, Apr-Jun, 2012

[30] M. W. Li, et al., "Bottom-up assembly of large-area nanowire resonator arrays," Nature Nanotechnology, vol. 3, pp. 88-92, Feb 2008.

[31] X. L. Feng, et al., "Very high frequency silicon nanowire electromechanical resonators," Nano Letters, vol. 7, pp. 1953-1959, Jul 2007.

[32] T. Henry, et al., "Directed growth of horizontally aligned gallium nitride nanowires for nanoelectromechanical resonator Arrays," Nano Letters, vol. 7, pp. 3315-3319, Nov 2007.

[33] A. K. Huttel, et al., "Carbon Nanotubes as Ultrahigh Quality Factor Mechanical Resonators," Nano Letters, vol. 9, pp. 2547-2552, Jul 2009.

[34] B. Lassagne, et al., "Ultrasensitive Mass Sensing with a Nanotube Electromechanical Resonator," Nano Letters, vol. 8, pp. 3735-3738, Nov 2008.

[35] H. Y. Chiu, et al., "Atomic-Scale Mass Sensing Using Carbon Nanotube Resonators," Nano Letters, vol. 8, pp. 4342-4346, Dec 2008.

[36] A. B. Kaul, Microelectronics to Nanoelectronics: Materials, Devices & Manufacturability: CRC Press, 2012.

[37] J. Arcamone, et al., "Nanomechanical Mass Sensor for Spatially Resolved Ultrasensitive Monitoring of Deposition Rates in Stencil Lithography," Small, vol. 5, pp. 176-180, Jan 19 2009.

[38] J. Arcamone, et al., "Full wafer integration of NEMS on CMOS by nanostencil lithography," 2006 International Electron Devices Meeting, Vols 1 and 2, pp. 250-253, 2006

[39] A. P. Malshe, et al., "Tip-based nanomanufacturing by electrical, chemical, mechanical and thermal processes," Cirp Annals-Manufacturing Technology, vol. 59, pp. 628-651, 2010

[40] R. V. Martinez, et al., "Silicon nanowire circuits fabricated by AFM oxidation nanolithography," Nanotechnology, vol. 21, Jun 18 2010.

[41] J. Martinez, et al., "Silicon Nanowire Transistors with a Channel Width of 4 nm Fabricated by Atomic Force Microscope Nanolithography," Nano Letters, vol. 8, pp. 3636-3639, Nov 2008.

[42] R. Held, et al., "In-plane gates and nanostructures fabricated by direct oxidation of semiconductor heterostructures with an atomic force microscope," Applied Physics Letters, vol. 73, pp. 262-264, 1998.

[43] S. C. Minne, et al., "Fabrication of 0.1 μm metal oxide semiconductor field - effect transistors with the atomic force microscope," Applied Physics Letters, vol. 66, pp. 703-705, 1995.

[44] L. Pellegrino, et al., "SrTiO3 Based Side Gate Field Effect Transistor Realized by Submicron Scale AFM Induced Local Chemical Reactions," Journal of Electroceramics, vol. 13, pp. 331-337, 2004/07/01 2004.

[45] M. Villarroya, et al., "AFM lithography for the definition of nanometre scale gaps: application to the fabrication of a cantilever-based sensor with electrochemical current detection," Nanotechnology, vol. 15, pp. 771-776, Jul 2004.

[46] R. D. Piner, et al., ""Dip-pen" nanolithography," Science, vol. 283, pp. 661-663, Jan 29 1999.

[47] H. Zhang, et al., "Fabrication of Sub-50-nm Solid-State Nanostructures on the Basis of Dip-Pen Nanolithography," Nano Letters, vol. 3, pp. 43-45, 2003/01/01 2002.

[48] H. Zhang and C. A. Mirkin, "DPN-Generated Nanostructures Made of Gold, Silver, and Palladium," Chemistry of Materials, vol. 16, pp. 1480-1484, 2004/04/01 2004.

[49] D. A. Weinberger, et al., "Combinatorial generation and analysis of nanometer- and micrometer-scale silicon features via "dip-pen" nanolithography and wet chemical etching," Advanced Materials, vol. 12, pp. 1600-1603, Nov 2 2000.

[50] S. Hu, et al., "Fabrication of silicon and metal nanowires and dots using mechanical atomic force lithography," Journal of Vacuum Science & Technology B, vol. 16, pp. 2822-2824, Sep-Oct 1998.

[51] A. Notargiacomo, et al., "Atomic force microscopy lithography as a nanodevice development technique," Nanotechnology, vol. 10, pp. 458-463, Dec 1999.

[52] T. H. Fang, et al., "Machining characterization of the nano-lithography process using atomic force microscopy," Nanotechnology, vol. 11, pp. 181-187, Sep 2000.

[53] Y. J. Chen, et al., "Fabrication of metal nanowires by atomic force microscopy nanoscratching and lift-off process," Nanotechnology, vol. 16, pp. 1112-1115, Aug 2005.

[54] L. A. Porter, et al., "Metallic nanostructures via static plowing lithography," Nano Letters, vol. 3, pp. 1043-1047, Aug 2003.

[55] W. P. King, et al., "Heated atomic force microscope cantilevers and their applications," Annual Review of Heat Transfer, vol. 16, 2013.

[56] U. Durig, et al., ""Millipede" - An ultrahigh density, high-data-rate AFM data storage system," Precision Engineering, Nanotechnology, Vol 1, Proceedings, pp. 482-485, 1999.

[57] U. Durig, et al., ""Millipede" - an AFM data storage system at the frontier of nanotribology," Tribology Letters, vol. 9, pp. 25-32, 2000.

[58] P. Vettiger, et al., "The "Millipede" - More than one thousand tips for future AFM data storage," Ibm Journal of Research and Development, vol. 44, pp. 323-340, May 2000.

[59] S. Somnath, et al., "Parallel nanoimaging and nanolithography using a heated microcantilever array," Nanotechnology, vol. 25, p. 014001, 2014.

[60] P. E. Sheehan, et al., "Nanoscale deposition of solid inks via thermal dip pen nanolithography," Applied Physics Letters, vol. 85, pp. 1589-1591, Aug 30 2004.

[61] W. K. Lee, et al., "Maskless nanoscale writing of nanoparticle− polymer composites and nanoparticle assemblies using thermal nanoprobes," Nano Letters, vol. 10, pp. 129-133, 2009.

[62] W. K. Lee, et al., "Chemically Isolated Graphene Nanoribbons Reversibly Formed in Fluorographene Using Polymer Nanowire Masks," Nano Letters, vol. 11, pp. 5461-5464, Dec 2011.

[63] M. Yang, et al., "Direct writing of a conducting polymer with molecular-level control of physical dimensions and orientation," Journal of the American Chemical Society, vol. 128, pp. 6774-6775, May 31 2006.

[64] B. Nelson, et al., "Direct deposition of continuous metal nanostructures by thermal dip-pen nanolithography," Applied Physics Letters, vol. 88, p. 033104, 2006.

[65] D. Wang, et al., "Thermochemical Nanolithography of Multifunctional Nanotemplates for Assembling Nano-Objects," Advanced Functional Materials, vol. 19, pp. 3696-3702, 2009.

[66] Z. Wei, et al., "Nanoscale Tunable Reduction of Graphene Oxide for Graphene Electronics," Science, vol. 328, pp. 1373-1376, June 11, 2010 2010.

[67] A. S. Basu, et al., "Scanning thermal lithography: Maskless, submicron thermochemical patterning of photoresist by ultracompliant probes," Journal of Vacuum Science & Technology B, vol. 22, pp. 3217-3220, Nov-Dec 2004.

[68] S. Kim, et al., "Direct Fabrication of Arbitrary-Shaped Ferroelectric Nanostructures on Plastic, Glass, and Silicon Substrates," Advanced Materials, vol. 23, pp. 3786-3790, 2011.

[69] W. K. Lee, et al., "Nanoscale Reduction of Graphene Fluoride via Thermochemical Nanolithography," Acs Nano, vol. 7, pp. 6219-6224, Jul 2013.

[70] P. C. Fletcher, et al., "Wear-Resistant Diamond Nanoprobe Tips with Integrated Silicon Heater for Tip-Based Nanomanufacturing," ACS Nano, vol. 4, pp. 3338-3344, Jun 2010.

CHAPTER 2: FABRICATION OF ARBITRARILY-SHAPED SILICON AND SILICON OXIDE NANOSTRUCTURES USING TIP-BASED NANOFABRICATION

2.1 Introduction

Tip-based nanofabrication (TBN) uses a nanometer-scale tip to interact with a sample to fabricate nanostructures. TBN has the potential for fabricating nanostructures with controlled size, shape and orientation at precise substrate locations and nanometer-scale precision and resolution[1]. In TBN, a tip can interact with the sample to fabricate nanostructures, with the tip influencing the surface through any of a number of mechanisms, including mechanical [2], electro-chemical [3], optical [4], chemical diffusion [5], thermal [6], electrical polarization [7], and plasma [8].

Although TBN has many advantages, there are only a few published articles that describe the use of TBN for nano-device fabrication [9-16]. A key challenge to realizing TBN-fabricated nanodevices is to incorporate TBN fabrication steps with other processing steps. Unfortunately, most TBN methods are not easily compatible with nanofabrication [17-22]. For example, dip pen nanolithography (DPN) can fabricate silicon nanostructures only when combined with intermediate chemical processing steps. One publication showed the use of DPN to fabricate gold nanostructures using DPN; and then used these gold nanostructures as a masking step for subsequent etching [23]. Oxidation-based TBN can fabricate silicon oxide nanostructures with only a few nanometers in thickness due to the slow oxidation rate. One publication showed that

---

This work previously published: H. Hu, P. K Mohseni, L. Pan, X. Li, S. Somnath, J. R. Felts, M. A. Shannon, W. P. King, Journal of Vacuum Science & Technology B. 31:06FJ01, 2013

the oxidation rate falls dramatically due to self-limiting behavior resulting from the build-up stress and a reduction of electrical field strength [24]. To achieve device fabrication using TBN, a simpler strategy would allow for better compatibility with silicon fabrication processes.

Here, we show that a heated AFM tip can deposit thick polymer nanostructures and transfer the written structures into both silicon and silicon oxide films in a one-step etching process. Moreover, we show the flexibility of the technique by demonstrating the fabrication of arbitrary shapes of solid structures of silicon oxide. Our TBN method is compatible with existing nanofabrication methods and especially suitable for device fabrication.

2.2 Experiment and Results

2.2.1 Nanostructures Formed Using Tip-Based Nanofabrication and Wet Chemical Etching

Figure 2.1 shows the process used to fabricate silicon oxide nanostructures by TBN. First we grew a 50 nm thick silicon oxide layer via thermal oxidation at 1000 °C for 80 minutes. Then, a heated AFM tip deposited polystyrene (PS) on top of the oxide layer via TBN. Following polymer deposition, we etched the 50 nm thick silicon oxide layer by dipping the sample into buffered hydrofluoric acid (BHF) for 60 seconds. BHF etched the silicon oxide that was not masked by the PS nanopatterns. The last step was to remove PS by acetone and oxygen plasma reactive ion etching (RIE).

A key step in the process is to provide polymer ink onto the cantilever tip, and to then deliver the polymer ink onto the surface. The polymer was loaded onto the cantilever tip by bringing the heated AFM tip end onto a PS fiber. The heated tip melted the PS, and then the PS flowed onto the tip [25]. After inking, we mounted the tip in an Asylum Research MFP-3D AFM and scanned the tip along a programmed path with a constant force at a speed of 150 nm/second

[25]. A closed-loop feedback circuit maintained the cantilever heater temperature at 260 °C [26]. When the tip was hot, the molten polymer would flow from the moving tip to the substrate and form solid PS nanostructures [6]. The force between the tip and the substrate was maintained around 200 nN during the deposition. During heating, the tip-sample adhesion force, measured by pulling the tip off of the surface, was about 425 nN.

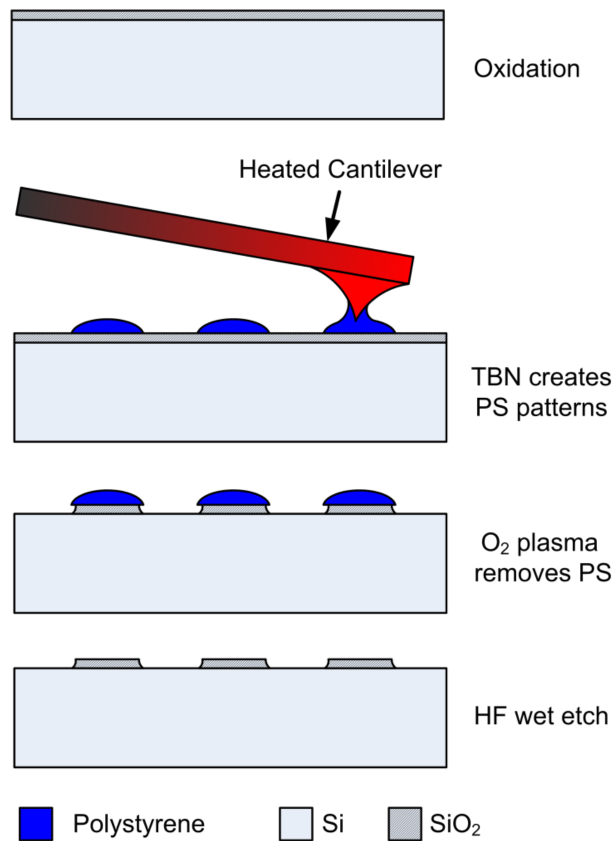

Figure 2.1 Schematics showing processing steps for fabricating silicon oxide nanostructures via TBN. The tip deposits molten polymer onto silicon oxide. The polymer nanostructures serve as an etch mask.

Figure 2.2(a) shows an AFM contact mode image of various PS linear nanostructures deposited using the heated AFM tip at different tip scanning speeds. The PS linear nanostructures from right to left as shown in Figure 2.2(a) are deposited by the heated AFM tip

at 0.1, 0.2, 0.4, 0.6, 0.8, 1.0, 1.5 and 2.0 μm/second tip scanning speeds. Figure 2.2(b) summarizes the PS nanostructure heights at different tip scanning speeds. As the tip scanning speed increases, the deposited polymer lines are thinner. This is consistent with a previous publication, which showed that polymer deposition rate is relatively independent of tip speed [25]. Thus a faster moving tip deposits less polymer per unit length, and therefore produces a thinner line.

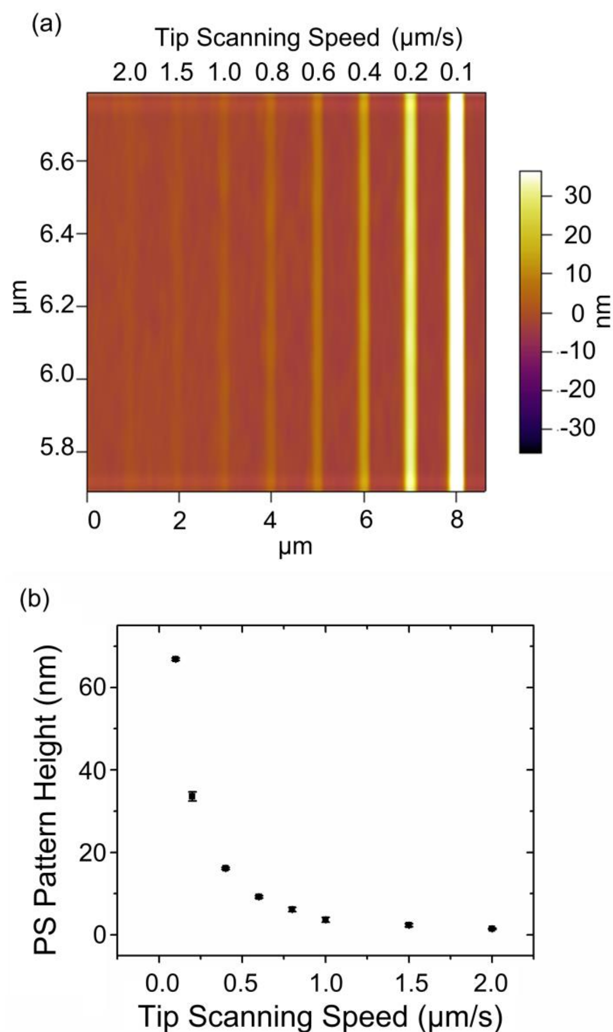

Figure 2.2 (a) An AFM topography of linear PS nanopatterns deposited by the heated AFM tip at different tip scanning speeds as shown. (b) Summary of PS nanopattern heights at different tip scanning speeds.

Figure 2.3(a) shows a scanning electron microscope (SEM) image of silicon oxide nanostructures fabricated by TBN at different writing speeds from 0.1 μm/second to 2 μm/second. Figure 2.3(b) shows AFM tapping mode image of the silicon oxide nanostructures. Figure 2.3(c) summarizes the silicon oxide nanostructure height versus the tip writing speed. All three figures show that silicon oxide nanostructures fabricated at slow tip writing speeds are taller than at those fabricated at fast tip writing speeds. The slower tip speeds correspond with thicker polymer structures on the surface, which better protect the silicon oxide during etching. As shown in Figure 2.3, when the tip speed exceeds 0.6 μm/second, the silicon oxide nanostructures become discontinuous. To fabricate unbroken silicon oxide nanostructures, the tip writing speed should be less than 0.6 μm/second. To ensure good quality silicon oxide nanostructures, we choose the tip writing speed to be 150 nm/second for all the experiments, with the exception of the dot-writing experiments, where the tip was stationary.

Figure 2.4(a) shows SEM images of two sets of circular silicon oxide nanostructures fabricated by TBN. In this case, the masking layer was TBN-fabricated PS nano-dots, which served as the mask for HF etching of the silicon oxide layer. The polymer nano-dots were deposited by a stationary heated tip with dwelling times from 2 seconds to 16 seconds with an incremental step of 2 seconds. Figure 2.4(b) shows an AFM tapping mode image of a single oxide dot pattern fabricated by dwelling the tip for 4 seconds and followed by BHF etching. The indentation on the circular silicon oxide nanostructure was formed because of the indentation of its etching mask, the molten polymer nano-dot. When the heated AFM tip finished depositing the polymer nanostructure, the heating was turned off. The indentation on the nanostructure was formed during polymer cooling with the tip still in contact with the polymer deposit. Figure 2.4(c) summarizes how the tip dwelling time impacts the size of the circular silicon oxide

nanostructures. The diameter of the circular silicon oxide nanostructure increases with the incremental increase of the tip dwelling time, which is consistent with previous publications [27].

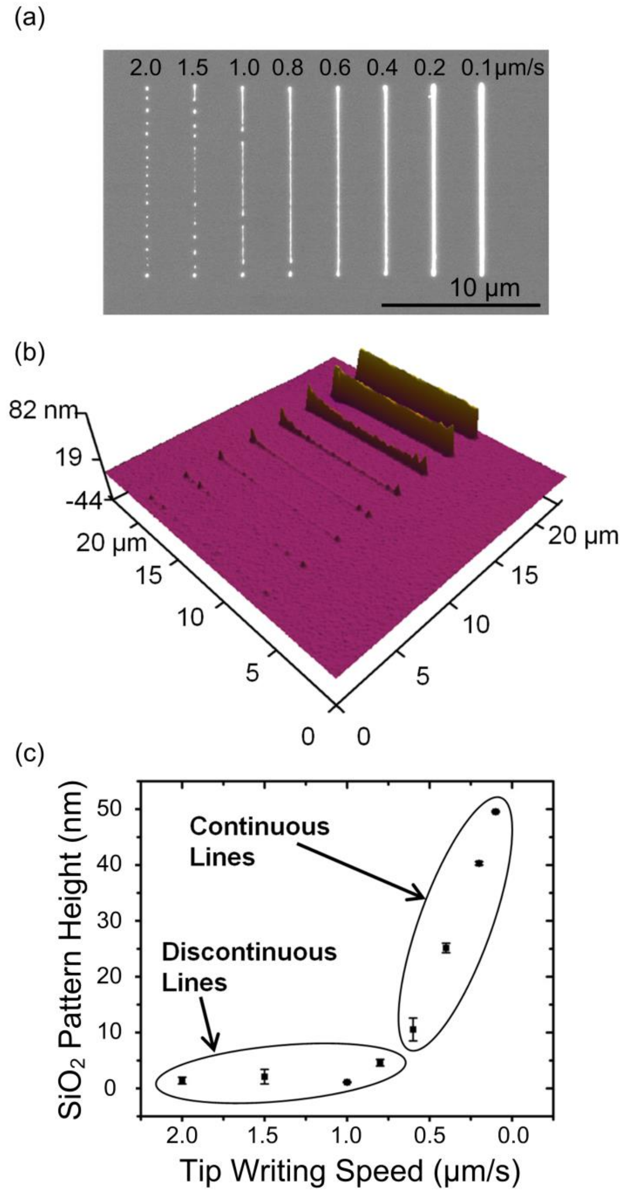

Figure 2.3 (a) SEM image of silicon oxide nanostructures fabricated via BHF wet etch. The PS nanostructures were deposited at different tip speeds, and served as an etch mask. (b) AFM tapping mode image of the silicon oxide structures. (c) Silicon oxide nanostructure height versus tip writing speeds. When tip writing speed is above 600 nm/s, silicon oxide nanostructures are no longer continuous.

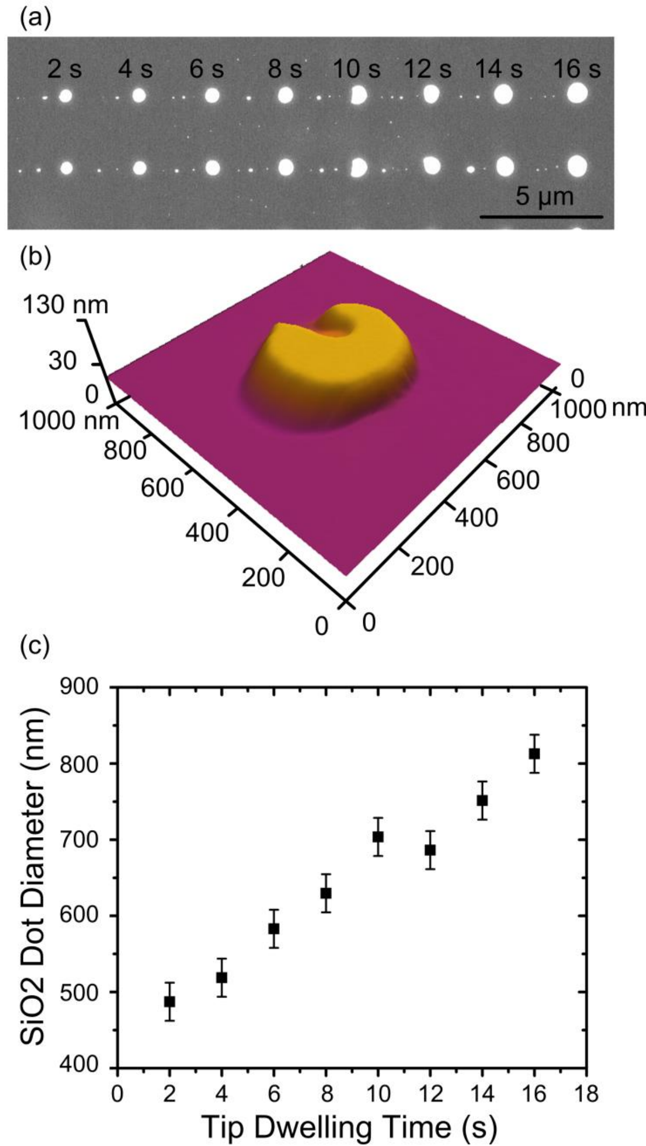

Figure 2.4 (a) SEM image of two sets of circular silicon oxide nanostructures fabricated using different tip dwelling times. (b) AFM tapping mode topography image of a circular silicon oxide nanostructure fabricated by TBN. The dwelling time was 4 seconds for the nanostructure. (c) Diameter of the circular silicon oxide nanostructures as a function of tip dwelling times.

Figure 2.5 shows SEM images of various basic silicon oxide nanostructures fabricated using the process described in Figure 2.1. All the structures are 50 nm in height. Figure 2.5(a, b) show an array of silicon oxide fin structures, each fin is 20 μm in length and 250 nm in width. Figure 2.5(c, d) show an array of curved silicon oxide fins structures. Each curved fin structure

consistis of a series of short linear fin structures. The heated AFM tip dwells longer in the joints between two short linear lines and therefore results in thicker nodes as shown in Figure 2.5(c, d). Figure 2.5(e, f) show an array of 8×8 circular silicon oxide nanostructures and each circular nanostructure is about 250 nm in diameter.

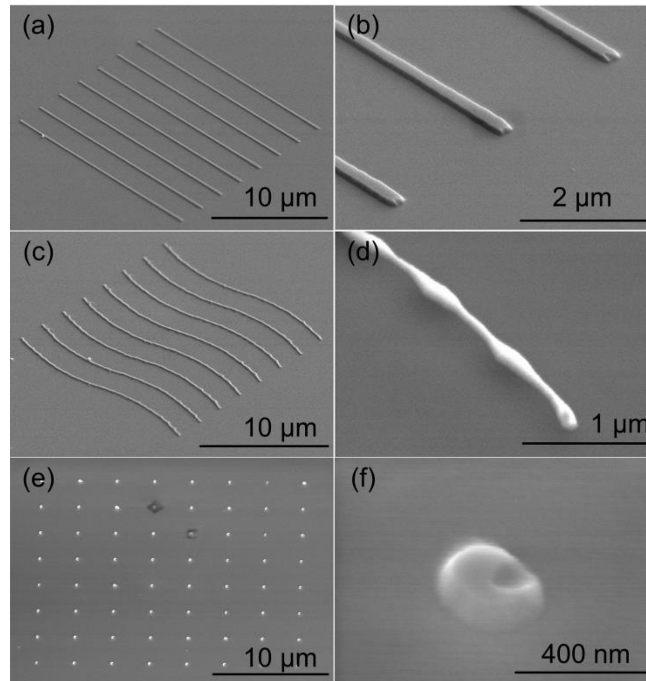

Figure 2.5 SEM images of basic types of silicon oxide nanostructures fabricated via TBN. (a) Array of silicon oxide fin structures; each fin is 20 μm long and 250 nm wide. (b) Zoomed-in view of silicon oxide fin structure. (c) Array of 8 curved silicon oxide fins. The curved fin consists of a series of linear fins. (d) Zoomed-in view of a section of a single curved fin. The thicker region joins between two adjacent linear fins where the heated tip paused. (e) Array of silicon oxide circular nanostructures, where each circular nanostructure is about 250 nm in diameter. (f) Zoomed-in view of a single circular silicon oxide nanostructure.

Figure 2.6 shows SEM images of various complex shapes of silicon oxide structures fabricated using the process described in Figure 2.1. Figure 2.6(a, b) show a circular ring silicon

oxide structure with a diameter of 7.8 μm. The ring consists of 32 individual line segments. Figure 2.6(c) shows a series of silicon oxide nanostructures mimicking ancient Chinese characters. Figure 2.6(d) shows the zoomed-in view of one character. Figure 2.6(e, f) show a lotus flower structure. The difference in the width of the pattern is due to different tip dwelling times. The tip dwells longer in the joints between two lines and, therefore, results in thicker patterns. All the above images demonstrate that our TBN method can fabricate arbitrary patterns of PS and transfer the patterns to solid silicon oxide structures. Since wet etching is an isotropic process, resulting in undercutting, the PS nanopatterns cannot mask the silicon oxide that is thicker than the width of the PS nanopatterns.

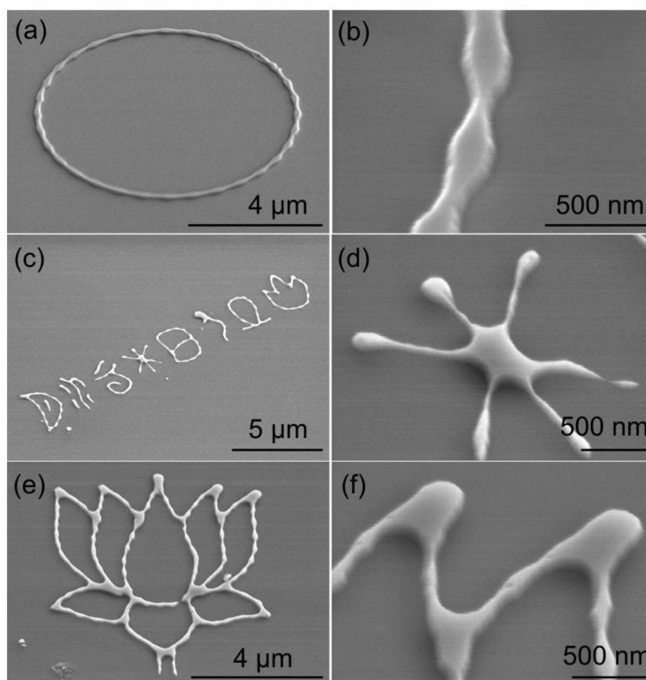

Figure 2.6 SEM images of complex silicon oxide nanostructures fabricated via TBN. (a) Ring structure with 6 μm diameter. (b) Zoomed-in view of a section of ring structure. (c) Set of ancient Chinese characters. (d) Zoomed-in view of a single character. (e) Nanostructure in the shape of a lotus flower. (f) Zoomed-in view of a section of the lotus flower.

2.2.2 *Nanostructures Formed Using Tip-Based Nanofabrication and Metal-Assisted Chemical Etching*

Figure 2.7 shows our process to fabricate nanostructures using TBN and metal-assisted chemical etching (MacEtch) [27, 28]. First, we fabricated a 9 μm square array of a photoresist pattern using conventional micro optical lithography to assist the MacEtch process. The micro-patterning process ensured that the extent of the gold layer, used as the MacEtch catalyst, could be limited to a finite area for improved control over vertical etching of high-aspect ratio features compared to MacEtch of a sample with no micro-patterning of gold films. Limiting the gold within a small finite area allows MacEtch solution to penetrate through the sides of the micropatterned region to etch the oxidized silicon more uniformly. If gold is not limited within a small area, the MacEtch solutions will reach the oxidized silicon on the peripheral region much more easily than the oxidized silicon in the middle, resulting in non-uniform etching. Next, a heated AFM tip deposited PS nanopatterns on the silicon within the 9μm hole. We then etched silicon via the Bosch process consisting of alterative steps of passivation and etching to form a shallow silicon structure having a profile amenable to gold lift-off. After Bosch etching, we evaporated a 35 nm thick gold layer onto the sample. Finally, we dipped the sample into a MacEtch solution to produce the silicon nanostructures. MacEtch was performed for a period of 25 minutes at room temperature in a solution of hydrofluoric acid (HF), hydrogen peroxide (H_2O_2), and ethanol (EtOH), with a volumetric ratio of 1:2:2, respectively (molar concentration of [HF] = 5.75 M, [H_2O_2] = 3.88 M, [EtOH] = 6.86 M).

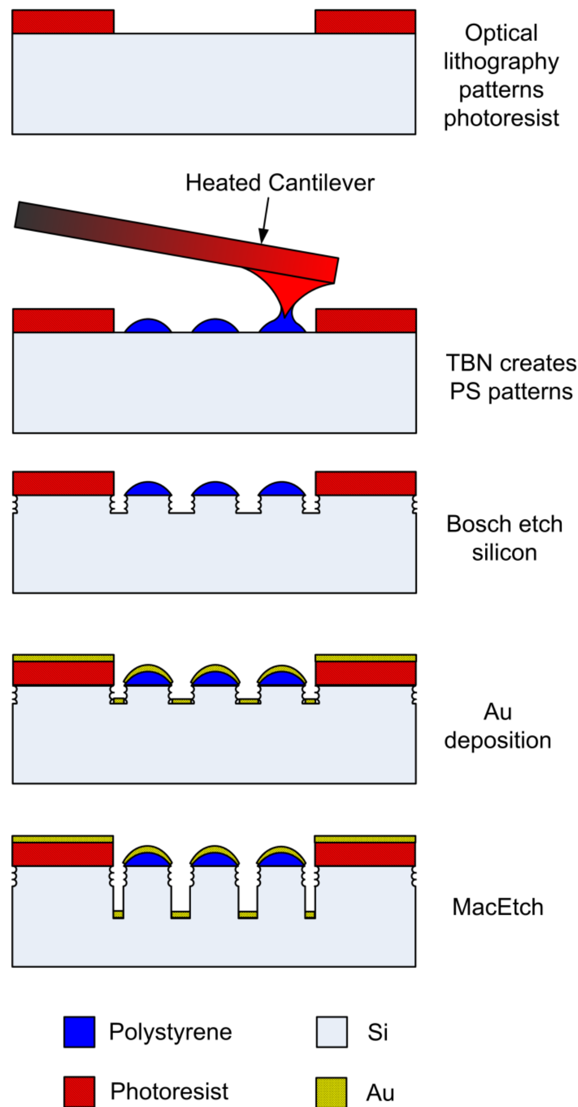

Figure 2.7 Schematics showing the major steps for transferring PS nanostructures to a gold film and creating silicon nanostructures by TBN and MacEtch.

Figure 2.8 compares the results of using Bosch etch to the results of using normal RIE etch before the MacEtch step. Figure 2.8(a) shows the silicon fin structures after Bosch silicon etch for 4 cycles using PS patterns as mask and Figure 2.8(b) shows the results after evaporating 35 nm thick gold film. The subset image of Figure 2.8(b) shows that the gold film on the bottom is separated from the gold film on the sidewall of the fin. Figure 2.8(c) shows silicon nitride nanostructures fabricated using TBN. We first deposited PS nanostructures using the heated

AFM tip on top of a 250 nm thick silicon nitride layer prepared by plasma enhanced chemical vapor deposition (PECVD). Then we etched the silicon nitride using PS nanostructures as etch mask in RIE for 5 minutes. The RIE etching conditions are 35mTorr pressure, 90 W RF power and 60 sccm flow of CHF_3 gas. Figure 2.8(d) shows the silicon nitride structure after evaporation of a 35 nm thick gold layer. The subset image inside Figure 2.8(d) shows that the gold film on the sidewall is connected with the gold film on the substrate surface, thereby covering the entire silicon nitride structure and preventing controlled MacEtch from proceeding.

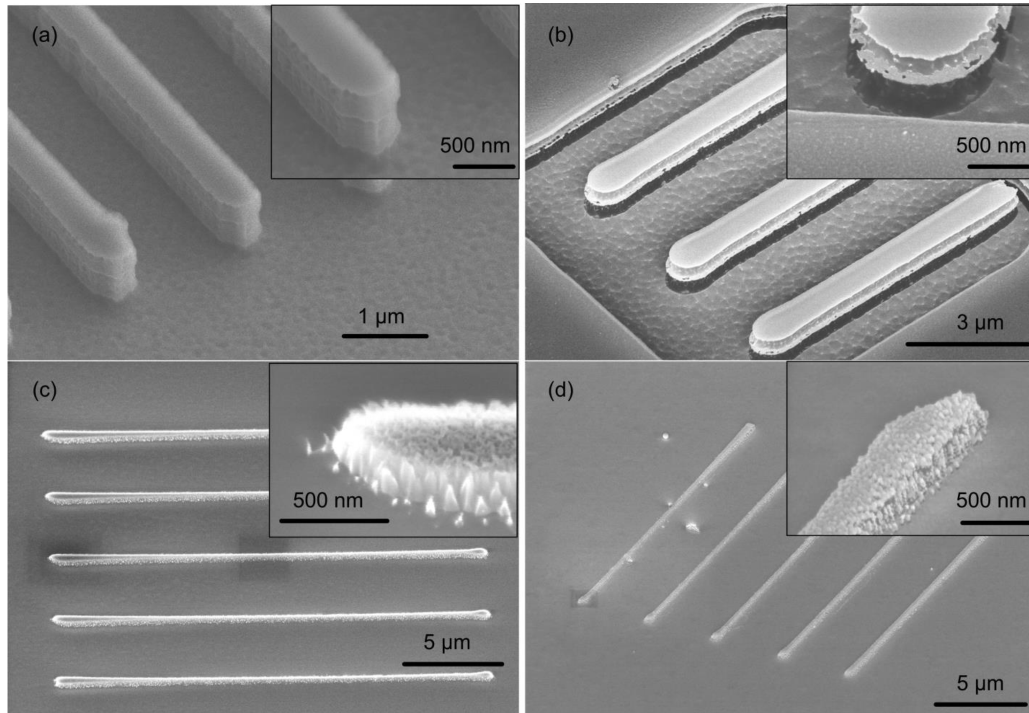

Figure 2.8 Comparison of Bosch silicon etch and RIE nitride etch. (a) SEM image of silicon fins after Bosch etch using PS nanostructures directly as an etching mask. (b) SEM image of silicon fins after 35 nm thick gold evaporation. The gold film on the sidewall of the fin is separated from the gold film on the bottom. (c) SEM image of 250 nm thick SiNx fins after 5 minutes RIE etching using PS nanostructures as etch mask. (d) SEM image of the SiNx fins after 35 nm thick gold evaporation. The gold film on the fin sidewall is contiguous with the gold film on the bottom, blanketing the entire SiNx fin and, thus, preventing the MacEtch from occurring.

Figure 2.9 shows the SEM images of various silicon nanostructures fabricated using TBN and MacEtch. Figure 2.9(a, b) show an array of six silicon fin structures, where each fin is 6 μm in length, 400 nm in width and 500 nm in thickness. The lower part of the silicon fin fabricated by MacEtch is smoother than the upper part of the silicon fin structure formed by Bosch silicon etch. With optimized MacEtch conditions, the sidewall roughness of the silicon nanowires fabricated by MacEtch can be as low as 2 nm [29]. Figure 2.9(c, d) show a lotus flower shaped structure that is about 4 μm in size and 500 nm in thickness. Figure 2.9(e, f) show an array of 3×3 vertical silicon nanowires (Si NW) with diameter about 500 nm for each Si NW.

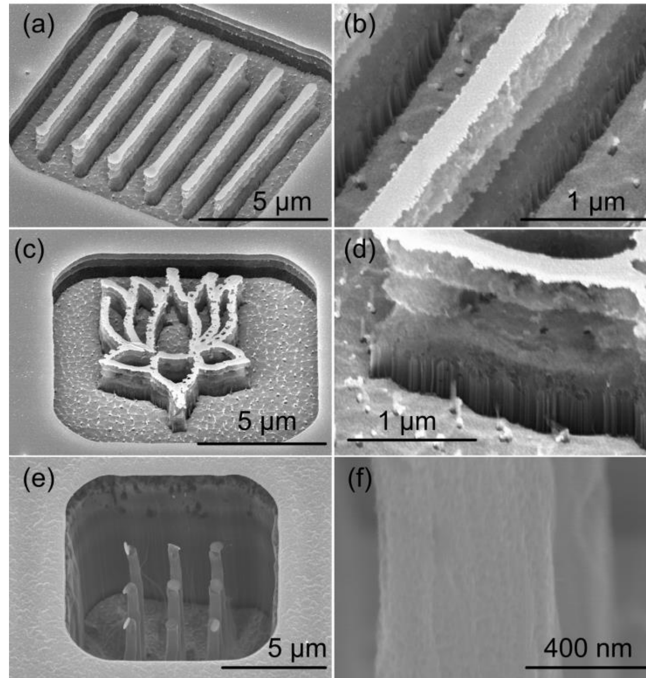

Figure 2.9 SEM images of different types of structures fabricated by TBN and MacEtch. (a) Array of six fins with 500 nm thick silicon. (b) Zoomed-in view of a single fin with bottom part silicon formed by MacEtch smoother than top part silicon formed by Bosch etch. (c) Lotus flower shape with bottom part silicon formed by MacEtch and top part silicon formed by Bosch Etch. (d) Zoomed-in view of the profile of the structure of (c). (e) Array of 9 μm tall vertical Si nanostructures. (f) Zoomed-in view of one Si nanostructure showing the smoothness of the sidewall rendered by MacEtch.

Figure 2.10 shows many arrays of Si NWs with different spacing and matrix sizes. Figure 2.10(a) shows an overview of 20 vertical arrays of Si NWs, within each square cell. All the Si NWs are 500 nm in diameter and 8μm in height. Figure 2.10(b) shows a 3×3 array of vertical Si NWs with a spacing of 2 μm. Figure 2.10(c) shows a 4×4 array of vertical Si NWs and each nanowire is spaced by 1.5 μm. Figure 2.10(d) shows a 6×6 array of vertical Si NWs and the spacing is 1 μm. The Si NWs stick to adjacent NWs and form bundles due to the surface tension of wet liquids when Si NWs are packed very closely.

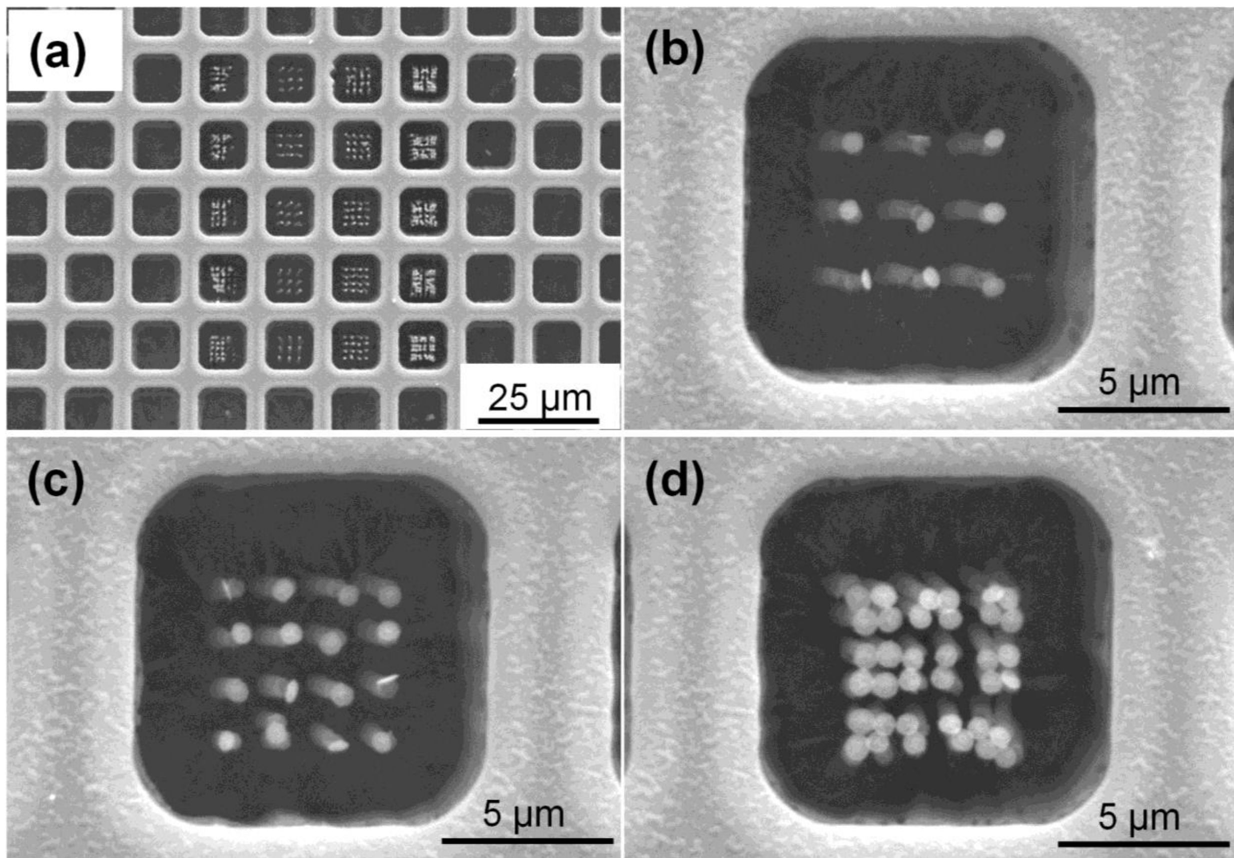

Figure 2.10 High aspect ratio vertical silicon nanostructures fabricated using TBN and MacEtch. (a) Overview of many arrays of smooth vertical silicon nanostructures. (b) Array with 2 μm spacing. (c) Array with 1.5 μm spacing. (d) Array with 1 μm spacing. These silicon nanostructures can form bundles when the spacing is small.

2.3 Discussion

There are three criteria that qualify a polymer material to serve as an etching mask. First, the polymer must survive through the wet chemical etching or reactive ion etching that follows the polymer deposition. Second, the polymer should be removed easily in order to limit further contamination. Third, the polymer must adhere to the substrate well. PS satisfies all the above criteria. We found 60 nm thick PS patterns deposited by the heated AFM tip can survive for 2 minutes in a standard Bosch etch process, 5 minutes of CHF_3 RIE etching (60 sccm gas flow, 35 mTorr pressure, 90 W RF power), more than 2 minutes in BHF wet etching. Moreover, PS can easily be removed by acetone or oxygen plasma RIE, both of which are very common processes in nanofabrication and will not result into contamination.

TBN offers many advantages over other nanolithography methods. In terms of cost, TBN can be performed using equipment that is much less expensive than equipment used by EBL or FIB. TBN can fabricate arbitrary shapes of nanostructures while nanoimprint lithography requires a mask to be fabricated before imprinting. TBN can also fabricate nanostructures onto a non-flat substrate. Finally, the AFM function of TBN can be used to perform metrology during fabrication.

2.4 Conclusions

We have presented a TBN technique that enables fabrication of silicon and silicon oxide through one step of etching, which makes it compatible with existing nanofabrication methods and suitable for device nanofabrication. PS nanostructures deposited from a heated AFM cantilever serve as etching mask and transfer the PS nanostructures to silicon or silicon oxide through etching. We demonstrated arbitrary shapes of silicon and silicon oxide nanostructure

such as rings, curved lines and a lotus flower. We also demonstrated the integration of TBN with both conventional wet etching and MacEtch. Moreover, due to the additive nature of our TBN method, it results in much less contamination than other nanolithography techniques that require spincoat of resist.

2.5 References

[1] D. M. Eigler and E. K. Schweizer, "Positioning single atoms with a scanning tunnelling microscope," *Nature,* vol. 344, pp. 524-526, 1990.

[2] H. Gobel and P. Vonblanckenhagen, "Atomic-Force Microscope as a Tool for Metal-Surface Modifications," *Journal of Vacuum Science & Technology B,* vol. 13, pp. 1247-1251, May-Jun 1995.

[3] J. A. Dagata, "Device Fabrication by Scanned Probe Oxidation," *Science,* vol. 270, pp. 1625-1626, Dec 8 1995.

[4] D. Hwang*, et al.*, "Nanoscale laser processing and diagnostics," *Applied Physics a-Materials Science & Processing,* vol. 96, pp. 289-306, Aug 2009.

[5] R. D. Piner*, et al.*, ""Dip-pen" nanolithography," *Science,* vol. 283, pp. 661-663, Jan 29 1999.

[6] P. Sheehan*, et al.*, "Nanoscale deposition of solid inks via thermal dip pen nanolithography," *Applied Physics Letters,* vol. 85, pp. 1589-1591, 2004.

[7] X. Q. Chen*, et al.*, "Surface potential of ferroelectric thin films investigated by scanning probe microscopy," *Journal of Vacuum Science & Technology B,* vol. 17, pp. 1930-1934, Sep-Oct 1999.

[8] I. W. Rangelow*, et al.*, "“NANOJET”: Tool for the nanofabrication," *Journal of Vacuum Science & Technology B,* vol. 19, pp. 2723-2726, 2001.

[9] R. V. Martinez, *et al.*, "Silicon nanowire circuits fabricated by AFM oxidation nanolithography," *Nanotechnology,* vol. 21, Jun 18 2010.

[10] M. Villarroya, *et al.*, "AFM lithography for the definition of nanometre scale gaps: application to the fabrication of a cantilever-based sensor with electrochemical current detection," *Nanotechnology,* vol. 15, pp. 771-776, Jul 2004.

[11] J. Martinez, *et al.*, "Silicon Nanowire Transistors with a Channel Width of 4 nm Fabricated by Atomic Force Microscope Nanolithography," *Nano Letters,* vol. 8, pp. 3636-3639, Nov 2008.

[12] S. Minne, *et al.*, "Fabrication of 0.1 μm metal oxide semiconductor field-effect transistors with the atomic force microscope," *Applied Physics Letters,* vol. 66, pp. 703-705, 1995.

[13] K. Matsumoto, *et al.*, "Room temperature operation of a single electron transistor made by the scanning tunneling microscope nanooxidation process for the TiO/Ti system," *Applied Physics Letters,* vol. 68, pp. 34-36, 1996.

[14] R. Held, *et al.*, "In-plane gates and nanostructures fabricated by direct oxidation of semiconductor heterostructures with an atomic force microscope," *Applied Physics Letters,* vol. 73, pp. 262-264, 1998.

[15] M. Fuechsle, *et al.*, "A single-atom transistor," *Nature Nanotechnology,* vol. 7, pp. 242-246, Apr 2012.

[16] L. Pellegrino, *et al.*, "SrTiO3 based side gate field effect transistor realized by submicron scale AFM induced local chemical reactions," *Journal of electroceramics,* vol. 13, pp. 331-337, 2004.

[17] G. P. Lopinski, *et al.*, "Self-directed growth of molecular nanostructures on silicon," *Nature,* vol. 406, pp. 48-51, Jul 6 2000.

[18] B. Klehn and U. Kunze, "Nanolithography with an atomic force microscope by means of vector-scan controlled dynamic plowing," *Journal of Applied Physics,* vol. 85, pp. 3897-3903, Apr 1 1999.

[19] D. Pires*, et al.*, "Nanoscale Three-Dimensional Patterning of Molecular Resists by Scanning Probes," *Science,* vol. 328, pp. 732-735, May 7 2010.

[20] M. Rolandi*, et al.*, "A new scanning probe lithography scheme with a novel metal resist," *Advanced Materials,* vol. 14, pp. 191-+, Feb 5 2002.

[21] D. A. Weinberger*, et al.*, "Combinatorial generation and analysis of nanometer- and micrometer-scale silicon features via "dip-pen" nanolithography and wet chemical etching," *Advanced Materials,* vol. 12, pp. 1600-+, Nov 2 2000.

[22] L. Pellegrino*, et al.*, "(Fe,Mn)(3)O-4 nanochannels fabricated by AFM local-oxidation nanolithography using Mo/poly(methyl methacrylate) nanomasks," *Advanced Materials,* vol. 18, pp. 3099-+, Dec 4 2006.

[23] K. S. Salaita*, et al.*, "DPN-generated nanostructures as positive resists for preparing lithographic masters or hole arrays," *Nano Letters,* vol. 6, pp. 2493-2498, 2006.

[24] P. Avouris*, et al.*, "Atomic force microscope tip-induced local oxidation of silicon: Kinetics, mechanism, and nanofabrication," *Applied Physics Letters,* vol. 71, pp. 285-287, Jul 14 1997.

[25] J. R. Felts*, et al.*, "Nanometer-scale flow of molten polyethylene from a heated atomic force microscope tip," *Nanotechnology,* vol. 23, p. 215301, Jun 1 2012.

[26] S. Somnath*, et al.*, "Improved nanotopography sensing via temperature control of a heated atomic force microscope cantilever," *Sensors Journal, IEEE,* vol. 11, pp. 2664-2670, 2011.

[27] Z. P. Huang, *et al.*, "Metal-Assisted Chemical Etching of Silicon: A Review," *Advanced Materials,* vol. 23, pp. 285-308, Jan 11 2011.

[28] X. L. Li, "Metal assisted chemical etching for high aspect ratio nanostructures: A review of characteristics and applications in photovoltaics," *Current Opinion in Solid State & Materials Science,* vol. 16, pp. 71-81, Apr 2012.

[29] K. Balasundaram, *et al.*, "Porosity control in metal-assisted chemical etching of degenerately doped silicon nanowires," *Nanotechnology,* vol. 23, Aug 3 2012.

CHAPTER 3: SILICON NANO-MECHANICAL RESONATORS FABRICATED USING TIP-BASED NANOFABRICATION

3.1. Introduction

Mechanical resonator devices with nanometer-scale features have promising applications including sensitive mass detection [1-3], single electron spin detection, and RF communications [4, 5]. Standard techniques for fabricating the nano-mechanical features of these devices include electron beam lithography (EBL) [6] and focused ion beam (FIB) patterning [7, 8]. Both EBL and FIB require expensive equipment, and the serial nature of these techniques can limit throughput. It is also possible to fabricate nano-mechanical resonators from nanomaterials such as carbon nanotubes (CNTs), nanowires (NWs), or graphene [9-13]. These materials-based approaches have limitations on materials compatibility, and the shape of the resonator is limited by the pre-grown nanomaterial. While all of the above approaches can be used to fabricate nano-mechanical resonators, there is still a need for the rapid and simple fabrication of nanostructures, particularly those having complex shapes. This paper presents tip-based nanofabrication (TBN) of nano-mechanical resonators, a relatively fast and simple approach for nanolithography.

TBN is a promising nanofabrication technology that can fabricate nearly any shape of nanostructure, with features as small as several nanometers [14-17]. While there have been a large number of articles published on the fabrication capabilities of TBN, only a few published

---

This work previously published: H. Hu, H. Cho, S Somnath, A. F Vakakis, W. P. King, Nanotechnology, 25:275301, 2014

articles report the fabrication of functional nanodevices using TBN. These include nano-transistors [18-21], nano-fluid channels [22], nano-wires [23], and nano-gaps [24]. Two major challenges hinder the use of TBN for nanodevice fabrications. The first challenge is the difficulty of using TBN for fabricating solid-state nano-mechanical structures that are integrated with other micro/nanofabrication processes. For example tip-based liquid deposition deposits chemicals that may not be directly compatible with other nanofabrication process [24], while oxidation-based TBN relies on specific electrochemical reactions that works for a limited number of substrate materials [25]. The second challenge is the difficulty of achieving nanometer-scale resolution in the alignment overlay of TBN-fabricated nanostructures. For example, if photolithography is used for alignment between features fabricated during different process steps, the overlay may be no better than about 2 µm [26]. In another example, electron beam lithography can be used to fabricate metal contact pads aligned silicon nanowires, with high precision; however, TBN has its largest advantage when it replaces EBL [21]. The present chapter reports a TBN technique that addresses both of these challenges in both process integration and also high resolution alignment, through the fabrication of nano-mechanical resonator devices using TBN.

3.2 Experiments and Results

Figure 3.1 shows the five major steps for fabricating the silicon nano-mechanical resonators using TBN. The process starts with a silicon-on-insulator (SOI) wafer having a 400 nm thick top silicon layer and a 2 µm thick buried silicon oxide layer. First, aluminum structures were fabricated by sputtering a 25 nm thick aluminum layer followed by conventional optical lithography and aluminum wet etching. Next, a heated AFM tip deposited polystyrene (PS) nanowires while the cantilever heater was held at 260 °C. Polymer flowed from the tip onto the substrate as the tip scanned the surface at a speed of 150 nm/sec [17]. The scanning speed does

not affect the width of the deposited PS structure; however it does affect the thickness of the PS structure. Next, Bosch etching transferred the patterns into the top silicon layer. The PS nanowires were removed using acetone and oxygen plasma etching. Finally, the silicon oxide layer was etched for 40 minutes using buffered hydrofluoric acid (BHF), which released the devices. For successful release of free-standing structures, we used a supercritical point dryer (Tousimis Automegasamdri@915-B) that employs liquid carbon dioxide for releasing soft structures such as our free-standing spiral-shaped resonators.

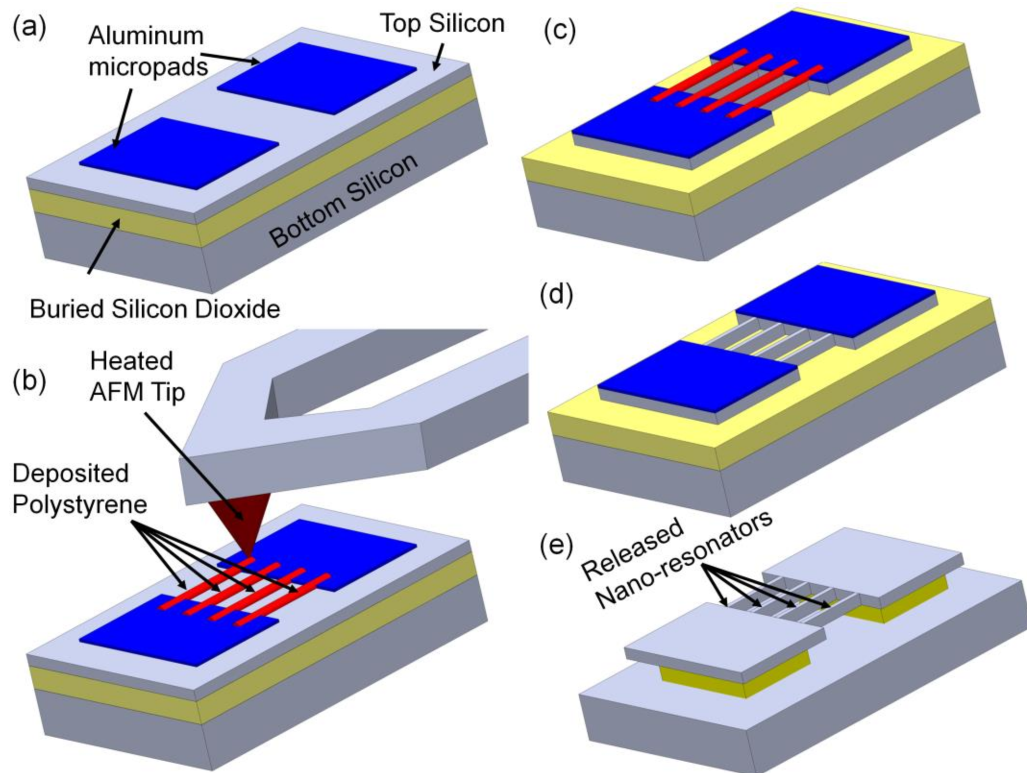

Figure 3.1 Schematic drawings showing the major steps for fabricating silicon nano-mechanical resonators using TBN: (a) Fabricate aluminum micropads using conventional optical lithography and wet etching. (b) Deposit polystyrene (PS) nanowires using the heated AFM tip across aluminum micropads. (c) Bosch silicon etching of top silicon layer of the silicon-on-insulator (SOI) wafer. (d) Remove PS nanowires using acetone and oxygen plasma etching. (e) Etching the buried silicon oxide layer to release the silicon nanobeams.

Figure 3.2 shows an array of double-clamped silicon nano-mechanical resonators fabricated using the above process. Figure 3.2(a) shows the key nanolithography step, an SEM image of six PS nanowires across two aluminum micropads. The thickness of the aluminum pads, 25 nm in this case, can be adjusted by varying sputtering deposition time. The PS nanowires are 500 nm wide and 200 nm thick. We found that the PS nanowires are thicker than the aluminum micropads to ensure continuous PS nanowires across the aluminum boundaries. During polymer deposition, the heated AFM tip scanned at a speed of 150 nm/sec, which was sufficiently slow to allow molten PS to flow to the substrate to form continuous 200 nm thick PS nanowires, which was much thicker than the aluminum micropads. Figure 3.2(b) shows that the PS nanowire is continuous across the edge of the aluminum pad. Figure 3.2(c) shows an array of released double-clamped nano-mechanical resonators fabricated using PS nanowires as etch mask. The nano-mechanical resonators have a width of 500 nm, a length of 18 μm, and a thickness of 400 nm and are suspended approximately 2 μm above the substrate. The particle residue observed in Figure 3.2(b) resulted from the wet aluminum etching and Bosch silicon etching. This residue sits on top of the buried oxide layer, and is removed once the buried oxide layer is etched away during the release step.

Figure 3.3 shows an example of a double-clamped spiral-shaped silicon nano-mechanical resonator fabricated using the above process. Figure 3.3(a) shows a spiral-shaped silicon nano-mechanical resonator underneath PS nanowires after Bosch etching between two aluminum micropads. Figure 3.3(b) shows a zoomed-in view of a section of the PS nanowires protecting the underlying silicon nanostructures. Figure 3.3(c) shows a released free-standing spiral-shaped silicon nano-mechanical resonator fabricated using PS nanowires as an etch mask. The spiral-shaped nano-mechanical resonator has a beam width of 300 nm and a thickness of 400 nm. The

inset image of Figure 3.3(c) shows a zoomed-in view of a section of the spiral-shaped resonator, showing the roughness on the edge is less than 10 nm. The edge roughness is affected mostly by the edge of the polymer mask.

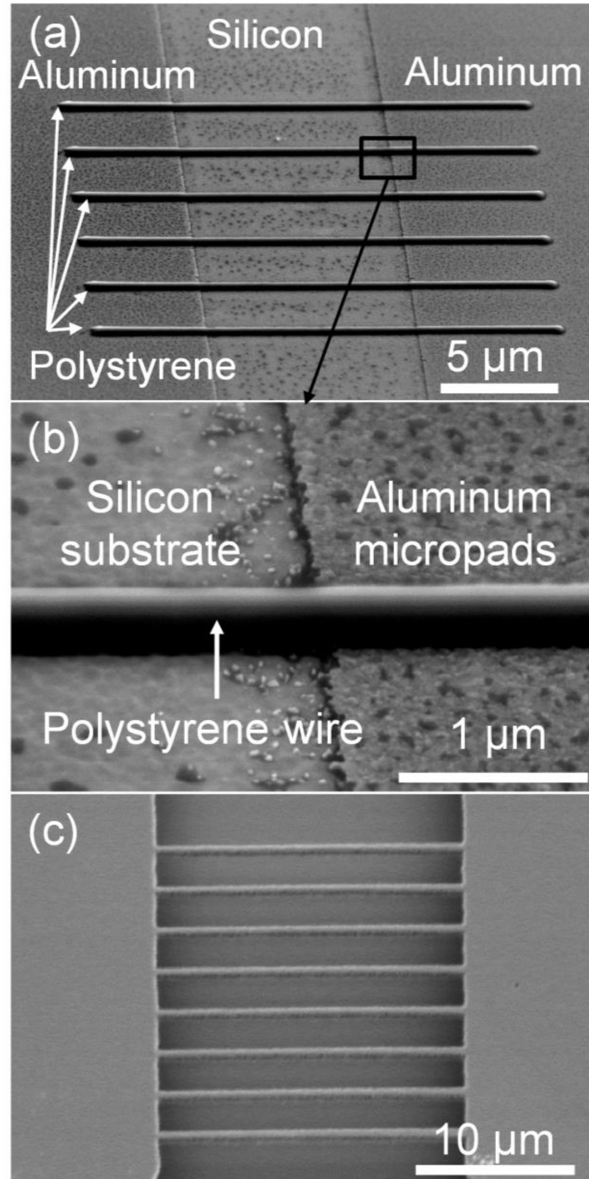

Figure 3.2 (a) SEM image showing an array of six PS nanowires deposited from the heated AFM tip across two 25nm thick aluminum micropads. (b) Zoomed-in view of a PS nanowire across the boundary of one aluminum micropad. (c) SEM image of an array of double-clamped silicon nano-mechanical resonators fabricated using PS nanopatterns.

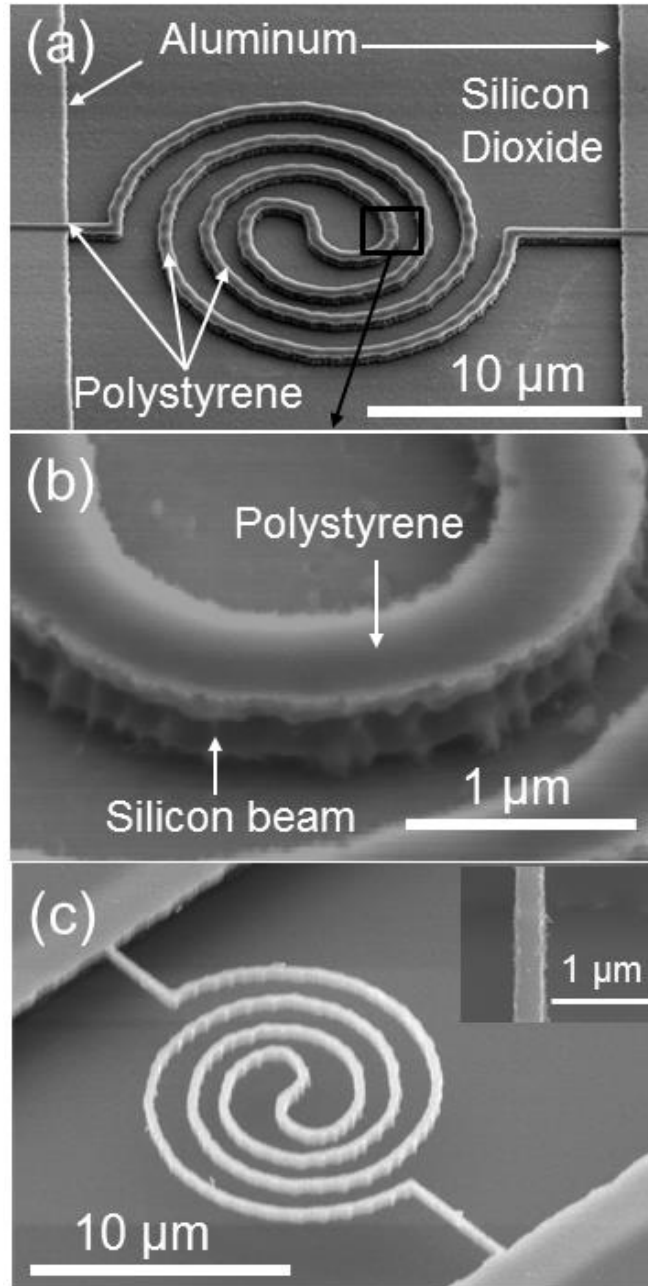

Figure 3.3 (a) SEM image showing the results of top silicon etching using spiral-shaped PS nanopatterns as well as two aluminum micropads as etch mask. (b) Zoomed-in view of a section of the spiral-shaped PS nanopatterns as well as the underneath spiral-shaped silicon nanostructures. (c) SEM image of a free-standing spiral-shaped silicon nano-mechanical resonator fabricated using PS nanopatterns as etch mask. The inset image shows a zoomed-in view of a section of the straight silicon beam of the spiral-shaped resonator. The width is about 300 nm and the edge roughness is less than 10 nm.

Figure 3.4(a) shows a SEM image of six linear single-clamped silicon nano-mechanical resonators. We measured the thermal vibration displacement of one of these devices at room temperature and ambient pressure using a laser vibrometer system (Polytec, UHF-120). Figure 3.4(b) shows the measured thermal response transformed to the frequency domain using Fast Fourier transform labeled as hollow circles. We estimated the resonant frequency of 1.5 MHz and the quality factor of 115 by fitting a Lorentzian function to the response. The inset image shows a prediction from finite element simulations for this resonator in the resonant mode.

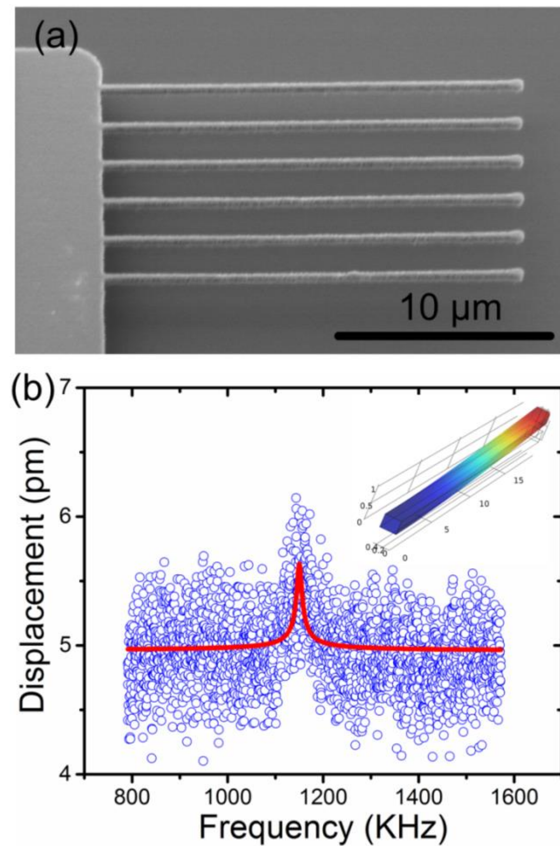

Figure 3.4 (a) SEM image of an array of six single-clamped silicon nano-mechanical resonators. (b) Measured displacement at different frequencies using a laser interferometer as shown in blue empty circle. The fitted data as shown in the red solid line shows a resonant frequency of 1.5 MHz and a quality factor of 115. The predicted frequency is 1.2MHz. The inset image shows the simulated nano-mechanical resonator in the resonant mode.

In order to better understand the fabricated devices, we used a finite element simulation in COMSOL to estimate the resonant frequency for comparison with the measured value. The simulation used 2329 kg/m^3 for the density, 170 GPa for the Young's modulus, and 0.28 for the Poisson's ratio for the material properties of silicon. The geometry of the resonator devices was taken from SEM images. In the case of the device from Figure 3.4, the length was 19.3 μm, width was 500 nm and the thickness was 400 nm. We assigned a fixed boundary condition to one end of the device and used 174 tetrahedral elements to form the mesh. COMSOL used an eigenfrequency simulation to predict a resonant frequency of 1.5 MHz, which is close to the measured value of 1.2 MHz. Because the simulation does not account for air damping, we expect the simulation to slightly overpredict the measured value [27].

Figure 3.5(a) shows a SEM image of the fabricated spider-like nano-mechanical resonator, consisting of a suspended silicon micropad in the center as the proof mass, defined by the optical lithography, and four silicon beams, defined by TBN. We measured the thermal vibration displacement of the resonator using a laser vibrometer with the laser focused on the central micropad. Figure 3.5(b) shows the measured displacement as hollow circles and the Lorentzian function fit as the solid red curve. The estimated fundamental resonant frequency is 2.2 MHz and the quality factor is 124. The inset image shows the simulated nano-mechanical resonator in the resonant mode.

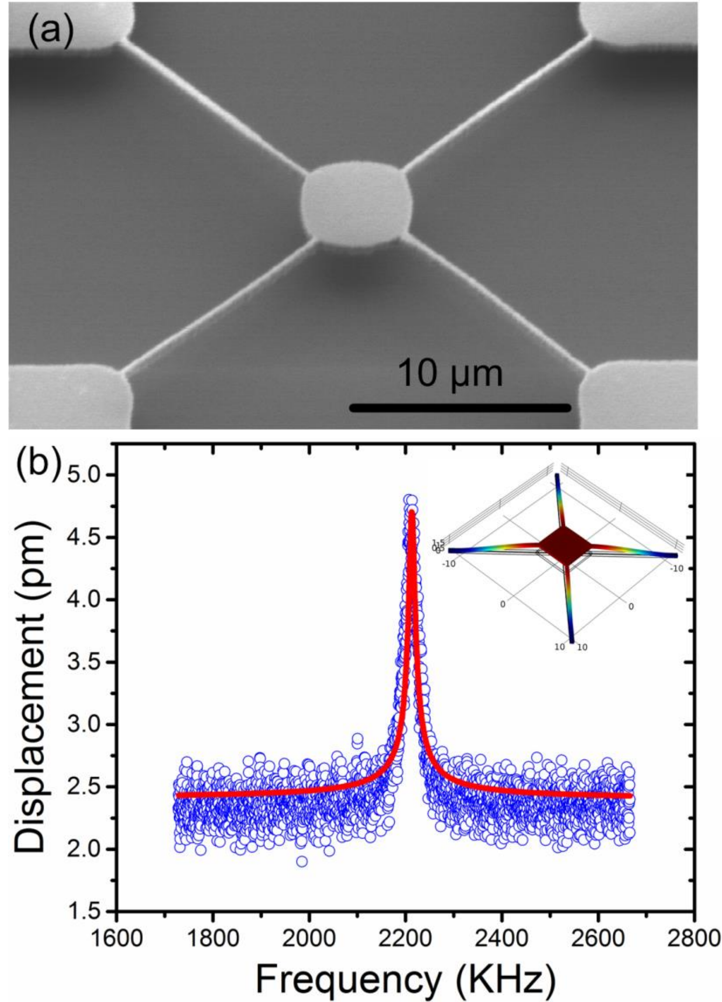

Figure 3.5 (a) A SEM image of a spider-like silicon nano-mechanical resonator. The center micropad is defined by optical lithography and is 4.3 μm in size. The four silicon nanobeams are defined by TBN and are 500nm in width. (b) Measured displacement of the center silicon micropad at different frequencies using a laser interferometer shown as blue empty circles. The fitted data shown as a red solid line shows a resonant frequency of 2.2 MHz and a quality factor of 124. The predicted frequency is 2.7 MHz. The inset image shows the simulated nano-mechanical resonator in the resonant mode.

We simulated the resonant characteristics of spider-like nano-mechanical resonator using COMSOL. We used the geometry derived from SEM images for the simulation. The length of the four beams is 15.4 μm, the width is 500 nm, and the thickness is 400 nm. The micropad suspended in the center was approximated as a square with 5.42 μm sides. We used the same

material properties of silicon as mentioned above. We used 4420 tetrahedral mesh elements in total. We assigned a fixed boundary condition to the fixed end of each silicon beam. The COMSOL simulation solved for the eigenfrequencies of the model. The predicted resonant frequency of 2.7 MHz is close to the measured resonant frequency 2.2 MHz. Again, the predicted value is higher than the measured value.

Figure 3.6 shows six different types of silicon nano-mechanical resonators fabricated using TBN. Figure 3.6(a) shows an array of eight linear double-clamped resonators. Figure 3.6(b) shows an array of linear single-clamped resonators with lengths ranging from 5 to 20 μm. Figure 3.6(c) shows three different types of spider-like resonators. The top silicon nano-mechanical resonator has a circular silicon micropad supported by four silicon beams not parallel to each other. The bottom two nano-mechanical resonators have two different sizes of rectangular micropads supported by four parallel silicon beams. Figure 3.6(d) shows three double-armed nano-mechanical resonators, with different shapes such as rectangle, U-shape, or V-shape. Figure 3.6(e) shows an array of two identical free-standing spiral-shaped resonators. Since this spiral-shaped resonator is soft and easily stuck to the substrate if directly dried in air, we used a supercritical point drier to obtain the free-standing spiral-shaped resonators. Figure 3.6(f) shows an array of four serpentine-shaped and double-clamped resonators. These nano-mechanical resonators all have a beam width around 500 nm and a thickness of 400 nm determined by the top silicon layer thickness of the SOI wafer.

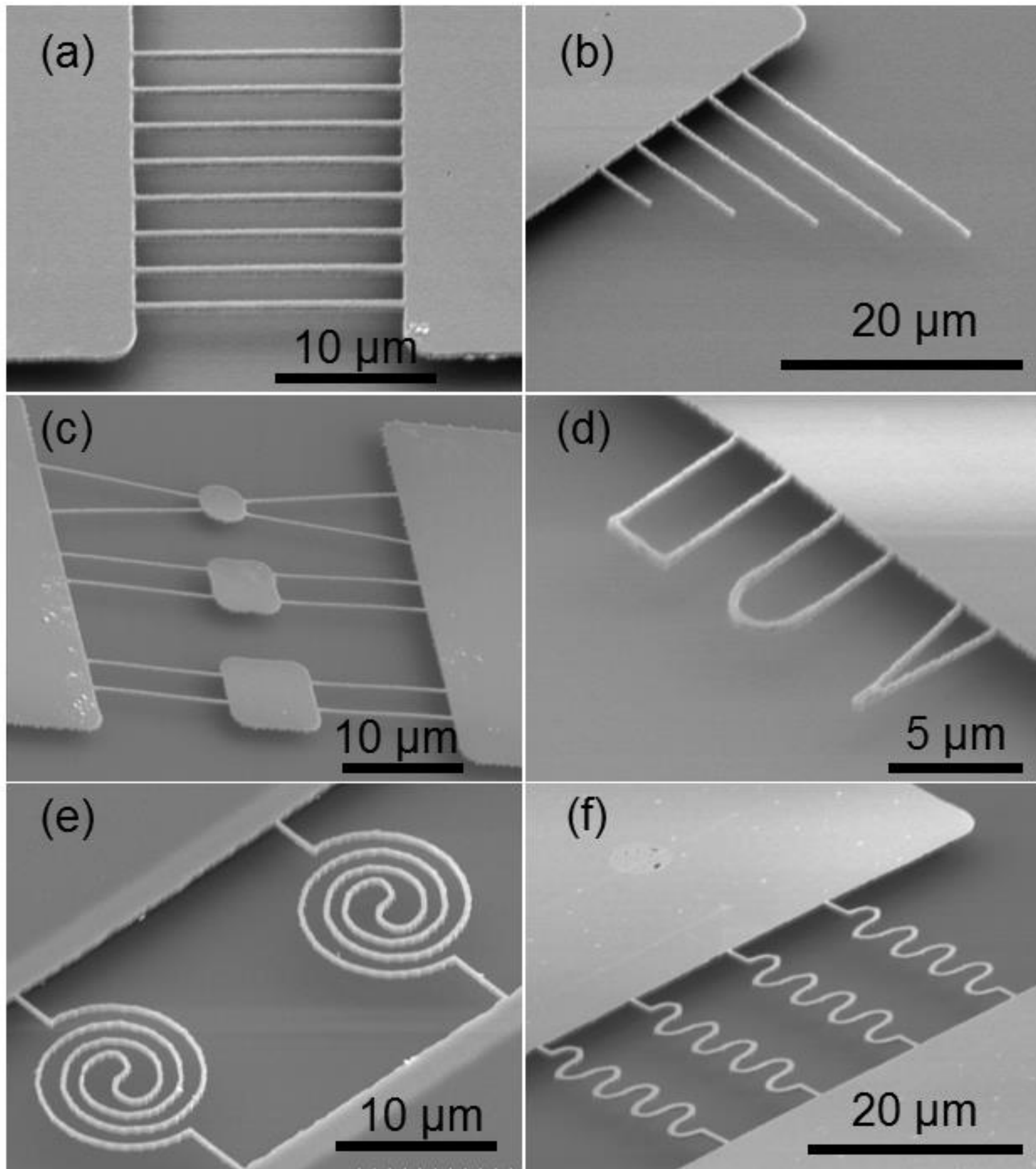

Figure 3.6 SEM images of different types of silicon nano-mechanical resonators fabricated using TBN. (a) Array of double-clamped silicon nano-mechanical resonators. (b) Array of single-clamped silicon nano-mechanical resonators with different lengths. (c) Spider-like nano-mechanical resonators with different pad shapes and sizes. (d) Double-armed silicon nano-mechanical resonators: U-shaped, V-shaped and rectangular-shaped. (e) Array of two free-standing spiral-shaped silicon nano-mechanical resonators released using critical point drying method. (f) Array of four serpentine-shaped and double-clamped silicon nano-mechanical resonators.

3.3 Discussion

The TBN technique described here has several advantages over existing TBN techniques and other nanofabrication techniques. First, our TBN method is additive and nearly free of any contamination since we deposit PS only where needed. This is in contrast to fabrication techniques such as EBL that require photoresist to completely cover the entire working substrate. The PS nanowires that are deposited can easily be removed using common methods for removing organic materials such as soaking in acetone or oxygen plasma etching. Second, our TBN method is compatible with existing nanofabrication processes. PS nanowires can serve as an etch mask either by themselves or together with other common masking materials such as silicon oxide, aluminum and photoresist. Third, our TBN method is compatible with a wide variety of substrate materials such as silicon, silicon oxide, silicon nitride, and metals. In contrast, other TBN methods that rely on electrochemical reactions only work on special substrates. Finally, our TBN method provides high precision feature alignment which is essential for fabricating nanoscale devices. Our TBN method uses the unheated tip in standard AFM operation to acquire the substrate topography. This topography information is used to precisely deposit the PS nanowires within the resolution of the closed-loop AFM scanner, less than 5 nm.

The width of the fabricated silicon nanowires is determined by the width of the polymer nanowires deposited from the heated AFM tip. The size and shape of the PS nanowires are determined by the molten PS droplet flow to the substrate. For the experiments described here, the PS nanowires are typically 500 nm wide. This is governed mainly by tip radius, polymer viscosity, wetting behavior of the substrate to the molten polymer and also substrate temperature [28]. The nanostructures could be made smaller by decreasing the tip radius, using a lower

viscosity polymer, or changing the substrate temperature. Based on exiting literature, we estimate the minimum resolution can be at least 10 nm [29].

We choose PS as the deposited polymer for three reasons [17]. First, PS is easily removed by acetone or oxygen plasma etching, either of which is commonly used in micro/nanofabrication process; therefore, PS results in very little contamination. Second, PS is found to mask silicon well during the Bosch silicon process in our experiment. Third, PS adheres to silicon and silicon oxide very well.

The advantages of TBN include total process time as well as process flexibility. First, the turnaround time of tip-based nanofabrication can be shorter than EBL or FIB. The tip scanning speed reported by TBN reached 100 mm/s, faster than the scanning speed of a commercial high resolution Gaussian e-beam lithography system [30]. Second, TBN can be parallelized. Several multi-probe lithography systems have been demonstrated including a 4096 tip array individually addressed [31-33]. Finally, TBN can be an additive fabrication process, while EBL is typically a subtractive fabrication process.

There are several advantages of using our TBN method particularly for fabricating silicon nano-mechanical resonators. First, TBN enables the fabrication of very small resonators having high resonance frequencies that can be used for applications such as frequency filtering and small mass sensing. Second, our TBN method can fabricate arbitrary-shaped nano-mechanical resonators; therefore, it is capable of tuning the spring constant of nano-mechanical resonators, reducing the footprint of nano-mechanical resonators, and creating non-linear resonance. For example, spiral-shaped nano-mechanical resonators can reduce the device footprint area and increase the integrating density [34]. Third, our TBN method is capable of alignment with nanometer resolution and therefore is suitable for fabricating three-terminal non-linear nano-

mechanical resonators [35] that are typically fabricated using expensive methods such as EBL or FIB.

3.4 Conclusions

In conclusion, we have presented the fabrication of silicon nano-mechanical resonators using TBN and characterization of the resonant frequency of two fabricated nano-mechanical resonators. We used a heated AFM tip to deposit polystyrene nanowires on substrate and employed the PS nanowires as etch mask to transfer the nanopatterns to silicon through one step of etching. We integrated our TBN method seamlessly with a standard surface micromachining process in an SOI wafer. Moreover, we demonstrated various types of silicon nano-mechanical resonators such as single-clamped, double-clamped, and novel resonator shapes such as spirals and spider shapes. Our TBN method is particularly suitable for nanodevice fabrication due to its simple operation in ambient conditions, compatibility with existing nanofabrication process, easy alignment functionality, and its in-situ scanning capability.

3.5 References

[1] H. G. Craighead, "Nanoelectromechanical systems," *Science,* vol. 290, pp. 1532-1535, Nov 24 2000.

[2] M. S. Hanay*, et al.*, "Single-protein nanomechanical mass spectrometry in real time," *Nature Nanotechnology,* vol. 7, pp. 602-608, Sep 2012.

[3] K. Jensen*, et al.*, "An atomic-resolution nanomechanical mass sensor," *Nature Nanotechnology,* vol. 3, pp. 533-537, Sep 2008.

[4] K. Jensen*, et al.*, "Nanotube radio," *Nano Letters,* vol. 7, pp. 3508-3511, Nov 2007.

[5] H. C. Kim and K. Chun, "RF MEMS technology," *IEEE Transactions on Electrical and Electronic Engineering,* vol. 2, pp. 249-261, May 2007.

[6] L. Yu*, et al.*, "Tunable, Dual-Gate, Silicon-on-Insulator (SOI) Nanoelectromechanical Resonators," *IEEE Transactions on Nanotechnology,* vol. 11, pp. 1093-1099, Nov 2012.

[7] N. Chekurov*, et al.*, "Dry fabrication of microdevices by the combination of focused ion beam and cryogenic deep reactive ion etching," *Journal of Micromechanics and Microengineering,* vol. 20, Aug 2010.

[8] J. Sulkko*, et al.*, "Strong Gate Coupling of High-Q Nanomechanical Resonators," *Nano Letters,* vol. 10, pp. 4884-4889, Dec 2010.

[9] X. L. Feng*, et al.*, "Very high frequency silicon nanowire electromechanical resonators," *Nano Letters,* vol. 7, pp. 1953-1959, Jul 2007.

[10] H. N. Cho*, et al.*, "Tunable, Broadband Nonlinear Nanomechanical Resonator," *Nano Letters,* vol. 10, pp. 1793-1798, May 2010.

[11] M. W. Li*, et al.*, "Bottom-up assembly of large-area nanowire resonator arrays," *Nature Nanotechnology,* vol. 3, pp. 88-92, Feb 2008.

[12] C. Y. Chen*, et al.*, "Performance of monolayer graphene nanomechanical resonators with electrical readout," *Nature Nanotechnology,* vol. 4, pp. 861-867, Dec 2009.

[13] A. Eichler*, et al.*, "Nonlinear damping in mechanical resonators made from carbon nanotubes and graphene," *Nature Nanotechnology,* vol. 6, pp. 339-342, Jun 2011.

[14] P. Avouris*, et al.*, "Atomic force microscope tip-induced local oxidation of silicon: Kinetics, mechanism, and nanofabrication," *Applied Physics Letters,* vol. 71, pp. 285-287, Jul 14 1997.

[15] A. A. Tseng, *et al.*, "Recent developments in tip-based nanofabrication and its roadmap," *Journal of Nanoscience and Nanotechnology,* vol. 8, pp. 2167-2186, May 2008.

[16] A. P. Malshe, *et al.*, "Tip-based nanomanufacturing by electrical, chemical, mechanical and thermal processes," *CIRP Annals-Manufacturing Technology,* vol. 59, pp. 628-651, 2010.

[17] H. Hu, *et al.*, "Fabrication of arbitrarily shaped silicon and silicon oxide nanostructures using tip-based nanofabrication," *Journal of Vacuum Science & Technology B,* vol. 31, pp. -, 2013.

[18] R. V. Martinez, *et al.*, "Silicon nanowire circuits fabricated by AFM oxidation nanolithography," *Nanotechnology,* vol. 21, Jun 18 2010.

[19] E. S. Snow and P. M. Campbell, "AFM Fabrication of Sub-10-Nanometer Metal-Oxide Devices with in-Situ Control of Electrical-Properties," *Science,* vol. 270, pp. 1639-1641, Dec 8 1995.

[20] F. J. Ruess, *et al.*, "Toward atomic-scale device fabrication in silicon using scanning probe microscopy," *Nano Letters,* vol. 4, pp. 1969-1973, Oct 2004.

[21] J. Martinez, *et al.*, "Silicon Nanowire Transistors with a Channel Width of 4 nm Fabricated by Atomic Force Microscope Nanolithography," *Nano Letters,* vol. 8, pp. 3636-3639, Nov 2008.

[22] L. Pellegrino, *et al.*, "(Fe,Mn)(3)O-4 nanochannels fabricated by AFM local-oxidation nanolithography using Mo/poly(methyl methacrylate) nanomasks," *Advanced Materials,* vol. 18, pp. 3099-+, Dec 4 2006.

[23] R. Held, *et al.*, "Fabricating tunable semiconductor devices with an atomic force microscope," *Applied Physics Letters,* vol. 75, pp. 1134-1136, Aug 23 1999.

[24] H. Zhang, *et al.*, "Fabrication of sub-50-nm solid-state nanostructures on the basis of dip-pen nanolithography," *Nano Letters,* vol. 3, pp. 43-45, Jan 2003.

[25] A. A. Tseng, *et al.*, "Nanofabrication by scanning probe microscope lithography: A review," *Journal of Vacuum Science & Technology B,* vol. 23, pp. 877-894, May-Jun 2005.

[26] S. Lenhert, *et al.*, "Massively parallel dip-pen nanolithography of heterogeneous supported phospholipid multilayer patterns," *Small,* vol. 3, pp. 71-75, Jan 2007.

[27] Z. J. Davis, *et al.*, "Monolithic integration of mass sensing nano-cantilevers with CMOS circuitry," *Sensors and Actuators A: Physical,* vol. 105, pp. 311-319, 2003.

[28] J. R. Felts, *et al.*, "Nanometer-scale flow of molten polyethylene from a heated atomic force microscope tip," *Nanotechnology,* vol. 23, Jun 1 2012.

[29] P. E. Sheehan, *et al.*, "Nanoscale deposition of solid inks via thermal dip pen nanolithography," *Applied Physics Letters,* vol. 85, pp. 1589-1591, Aug 30 2004.

[30] P. C. Paul, *et al.*, "Rapid turnaround scanning probe nanolithography," *Nanotechnology,* vol. 22, p. 275306, Jul 8 2011.

[31] A. Pantazi, *et al.*, "Probe-based ultrahigh-density storage technology," *Ibm Journal of Research and Development,* vol. 52, pp. 493-511, Jul-Sep 2008.

[32] S. Somnath, *et al.*, "Parallel nanoimaging and nanolithography using a heated microcantilever array," *Nanotechnology,* vol. 25, Jan 10 2014.

[33] K. Salaita, *et al.*, "Massively parallel dip-pen nanolithography with 55 000-pen two-dimensional arrays," *Angew Chem Int Ed Engl,* vol. 45, pp. 7220-3, Nov 6 2006.

[34] T. Galchev, *et al.*, "A Piezoelectric Parametric Frequency Increased Generator for Harvesting Low-Frequency Vibrations," *Journal of Microelectromechanical Systems,* vol. 21, pp. 1311-1320, Dec 2012.

[35] I. Kozinsky, *et al.*, "Tuning nonlinearity, dynamic range, and frequency of nanomechanical resonators," *Applied Physics Letters,* vol. 88, Jun 19 2006.

CHAPTER 4: NANOFLUIDIC CHANNELS OF ARBITRARY SHAPES FABRICATED BY TIP-BASED NANOFABRICATION

4.1 Introduction

Nanofluidic channels provide nanometer-scale physical confinement to biomolecules, and therefore are suitable for manipulation and analysis of DNA [1-5], proteins [6] and single molecules [7, 8]. Nanofluidic channels also exhibit unique ion transport behavior when at least one dimension of the channel is close to the Debye length [9-13]. Conventional fabrication methods for nanofluidic channels only provide one nanometer-scale dimension, which is the height of the channel [14-17]. To achieve nanometer-scale physical confinement on lateral dimension, advanced nanofabrication techniques such as electron beam lithography (EBL) [18] and focused ion beam (FIB) [19] are required. However, EBL and FIB are expensive and are difficult for massive production of nanofluidic channels. Moreover, EBL and FIB are both serial processes and are not easily scalable. Nanoimprint requires a master mold that is usually expensive to prepare and can only replicate the design of the mold [20]. Several novel nanofluidic channel fabrication methods that rely on certain mechanisms such as elastomeric collapse [21] and wrinkling [22] have the advantages of low-cost and simplicity in fabrication, but the design flexibility is relatively limited.

This work previously submitted: H. Hu, Y. Zhuo, M. E. Oruc, B. T. Cunningham and W. P. King, submitted to Nanotechnology, 2014

Tip-based nanofabrication (TBN) uses a nanometer scale tip to interact with substrate to define nanoscale features through a number of mechanisms such as manipulation, mechanical scratch, chemical diffusion, thermal indentation, thermal deposition, electrochemical reaction, plasma, etc. TBN employs either scanning tunneling microscopy (STM) [23-25] or atomic force microscopy (AFM) [26], either of which cost much lower than EBL and FIB. Moreover, TBN has the potential of achieving parallelization through using an array of tips [27]. However, very few publications reported the use of TBN for fabricating nanofluidic channels [28, 29]. One essential reason is that most TBN methods are not compatible with existing nanofabrication methods and are not easily suitable for fabricating solid-state material nanostructures.

This chapter presents a tip-based nanofabrication (TBN) method for fabricating arbitrary shapes of nanofluidic channels. We used a heated AFM tip to deposit dense polymer nanowires that served directly as an etch mask to fabricate silicon nanostructures through one step of etching [30]. The silicon nanostructures were used as a mold for replicating PDMS nanofluidic channels. This TBN process is compatible with existing nanofabrication methods

4.2 Experiment

Figure 4.1 shows the major steps in the fabrication process of the nanofluidic channels. The first step (Figure 4.1a) was to fabricate micro-patterned silicon dioxide. Starting with a [100] silicon wafer, 70 nm thick silicon dioxide layer was grown in a 1000 °C oxidation furnace for 2 hours, followed by patterning photoresist using conventional optical lithography, and then etching the silicon dioxide unprotected by the photoresist using buffered hydrofluoric acid (BHF). The second step (Figure 4.1b) was to deposit polystyrene (PS) nanowires using the heated AFM tip. A closed-loop feedback circuit kept the heated AFM tip at 260 °C while the molten PS

flowed from the tip to the silicon substrate [31, 32]. The third step (Figure 4.1c) was to etch silicon using Bosch process for 1 minute with micro-patterned silicon dioxide and deposited PS nanowires. The PS nanowires and the silicon dioxide together served as etch mask [30]. To reduce the scallops present on the sidewalls of the silicon structures fabricated by the Bosch process, we tuned the etching step to be 2.5 seconds and the passivation step to be 1.5 seconds. After etching, the remaining silicon was used later as a mold for replicating PDMS nanofluidic channels. The fourth step (Figure 4.1d) was to mold PDMS with the fabricated silicon mold. We mixed PDMS (sylgard 184) base with a curing agent at a mass ratio of 4:1. After degassing the mixture, we poured the mixture on top of the silicon master and heated on a 60 °C hotplate for 12 hours to cure the PDMS. To facilitate the PDMS demolding process, we deposited 15 nm thick amorphous fluorocarbon film on the silicon mold using sputtering before pouring PDMS on the silicon mold [33]. The fifth step (Figure 4.1e) was to peel the PDMS channel layer off and manually punch four through-holes on the cured PDMS channel later serving as liquid inlets and outlets. The last step (Figure 4.1f) was to bond this PDMS channel to a glass slide. Before bonding, the glass slide surface was cleaned with acetone, isopropyl alcohol (IPA), water, IPA in sequence and finally blown dry. Then the glass slide and the PDMS channels were both treated using 100 W oxygen plasma for 20 seconds. Then PDMS surface was brought into contact with glass slide surface and baked on a 90 °C hotplate for 20 minutes.

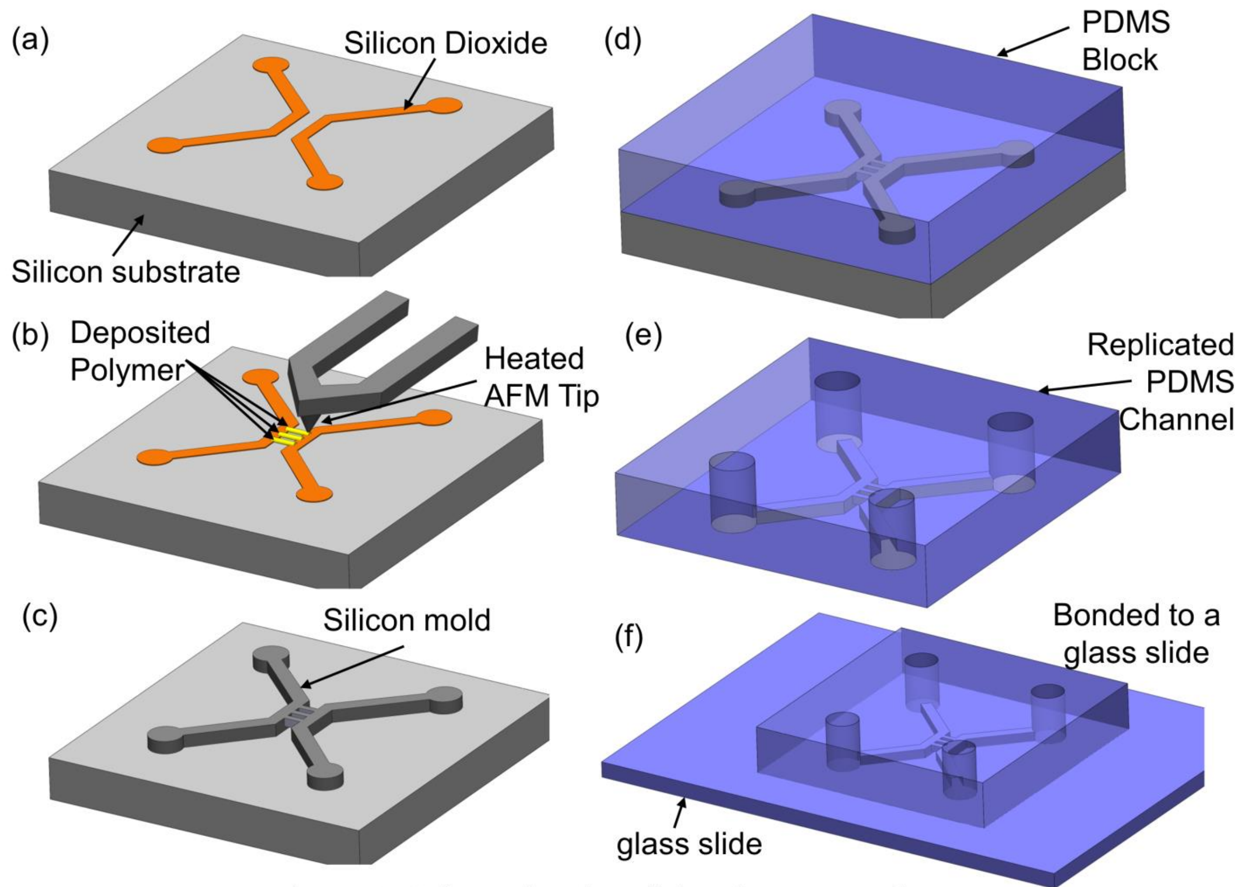

Figure 4.1 Schematics of major steps in the TBN process for fabricating nanofluidic channels. (a) Fabricate silicon dioxide micropatterns using conventional optical microlithography and wet hydrofluoric acid etching; (b) Deposit polymer nanowires across the silicon dioxide micropatterns using a heated AFM tip; (c) Bosch silicon etching using both micropatterned silicon dioxide and polymer nanowires as etch mask; (d) Cast PDMS on the fabricated silicon mold; (e) Peel off PDMS layer from the silicon mold and punch four through-hole vias as the solution inlets and outlets; (f) Bond PDMS channel to a glass slide.

Figure 4.2 shows the fabrication results for a single nanofluidic channel using the above-described process. Figure 4.2(a) is a SEM image of a silicon mold and the inset image shows a zoomed-in view of the silicon mold. The silicon mold has a length of 10 µm, a width of 380 nm, and a height of 900 nm. Figure 4.2(b) is a microscopic image of the PDMS nanofluidic channel

replicated from the silicon mold shown in Figure 4.2(a). Figure 4.2(c) shows a SEM image of the nanofluidic channel. To avoid electron charging effect and obtain good SEM images, we coated the PDMS nanofluidic channel with 2.5 nm thick gold coating by sputtering. The wrinkles shown at the PDMS surface are due to the swelling of PDMS during the sputtering [34, 35]. Figure 4.2(d) is the zoomed-in view of the PDMS nanofluidic channel. The nanofluidic channel is 10 μm long, 300 nm wide and 500 nm deep.

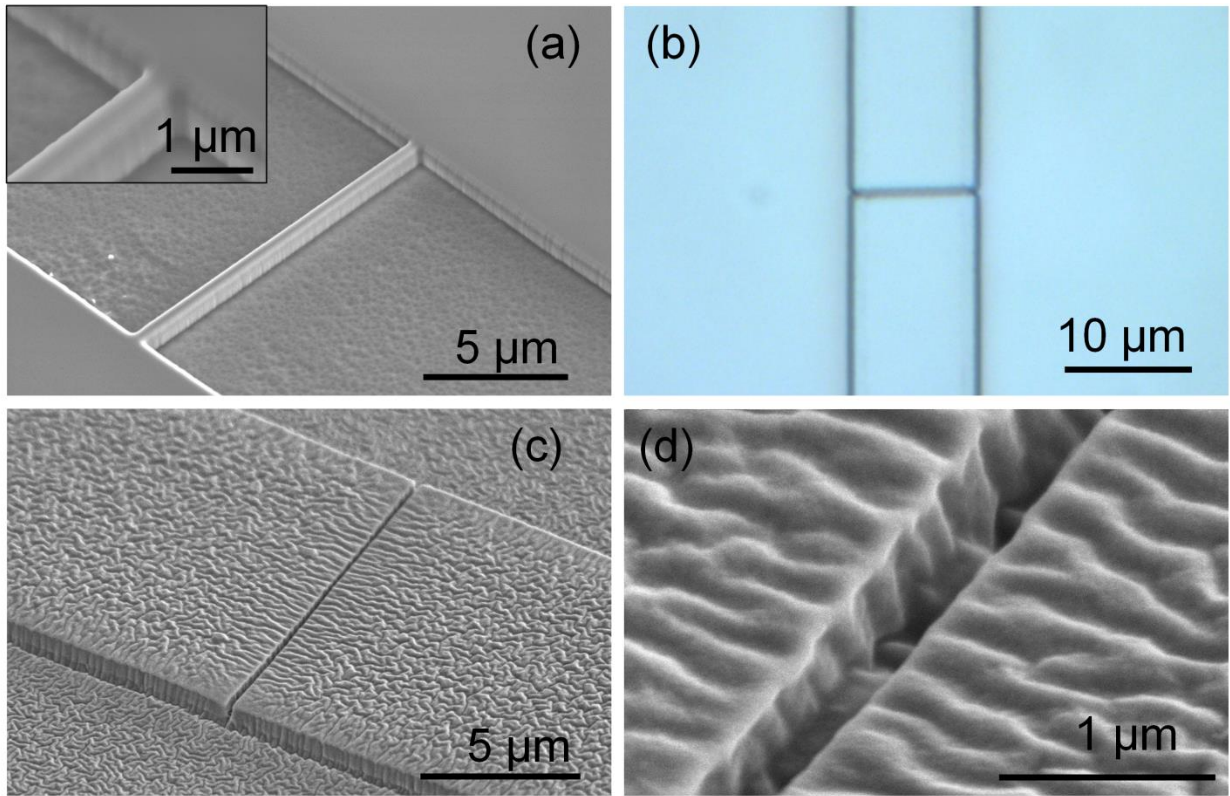

Figure 4.2 (a) SEM image of a silicon single linear nanochannel mold; the inset image shows the zoomed-in view of a section of the nanochannel mold; (b) A microscopic image of the PDMS nanofluidic channel replicated from the silicon mold as shown above; (c) A SEM image of the PDMS nanofluidic channel replicated; (d) A zoomed-in view of a section of the PDMS nanofluidic channel replicated.

Figure 4.3 shows the fabrication results of two different nanofluidic channel arrays using the present TBN process. Figure 4.3(a) shows a SEM image of the silicon mold used for producing an array of 10 linear nanofluidic channels and Figure 4.3(b) shows a microscope image of the corresponding replicated PDMS nanofluidic channel array. Figure 4.3(c) shows a SEM image of silicon mold used for fabricating an array of 10 curved nanofluidic channels while Figure 4.3(d) shows a microscope image of the corresponding replicated PDMS nanofluidic channel array. The length of the nanofluidic channel is 10 μm, the width is 300 nm and the depth is about 500 nm.

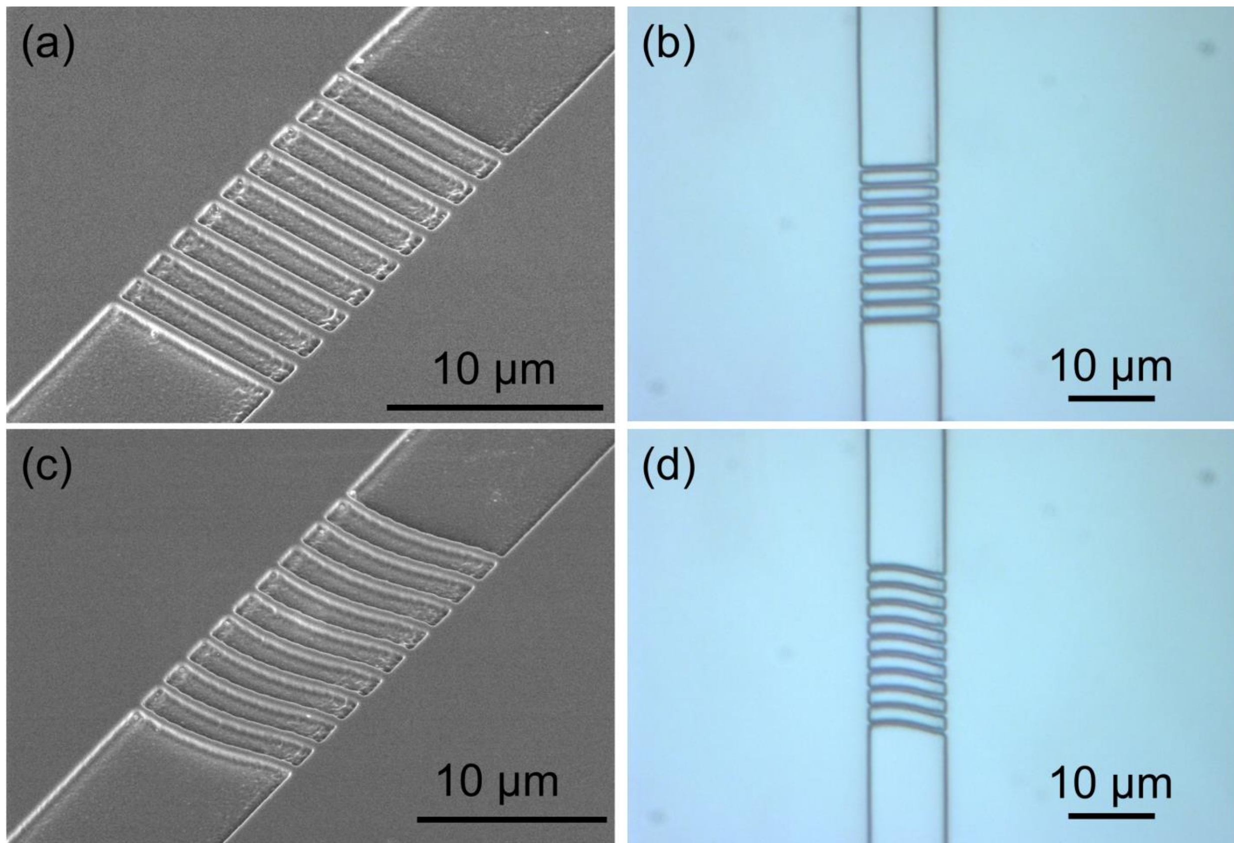

Figure 4.3 (a) SEM image of the silicon mold used for an array consisting of 10 linear nanofluidic channel array; (b) Microscope image of a replicated PDMS nanofluidic channel array consisting of 10 linear nanofluidic channels; (c) SEM image of the silicon mold used for an array consisting of 10 curvy nanofluidic channels; (d) Microscope image of a replicated PDMS nanofluidic channel array consisting of 10 curvy nanofluidic channels.

To show the flexibility of this TBN fabrication process, we fabricated two nanofluidic channel arrays with more complex shapes using the TBN process. Figure 4.4(a) shows a SEM image of the silicon mold for an array of three spiral-shaped nanofluidic channels while Figure 4.4(b) shows a zoomed-in view of a section of a spiral-shaped silicon mold. Figure 4.4(c) shows a SEM image of the silicon mold for an array of four wavy-shaped nanofluidic channels while Figure 4.4(d) shows a zoomed-in view of one wavy-shaped silicon mold. The nanofluidic channel width is 250 nm and the channel depth is about 800 nm.

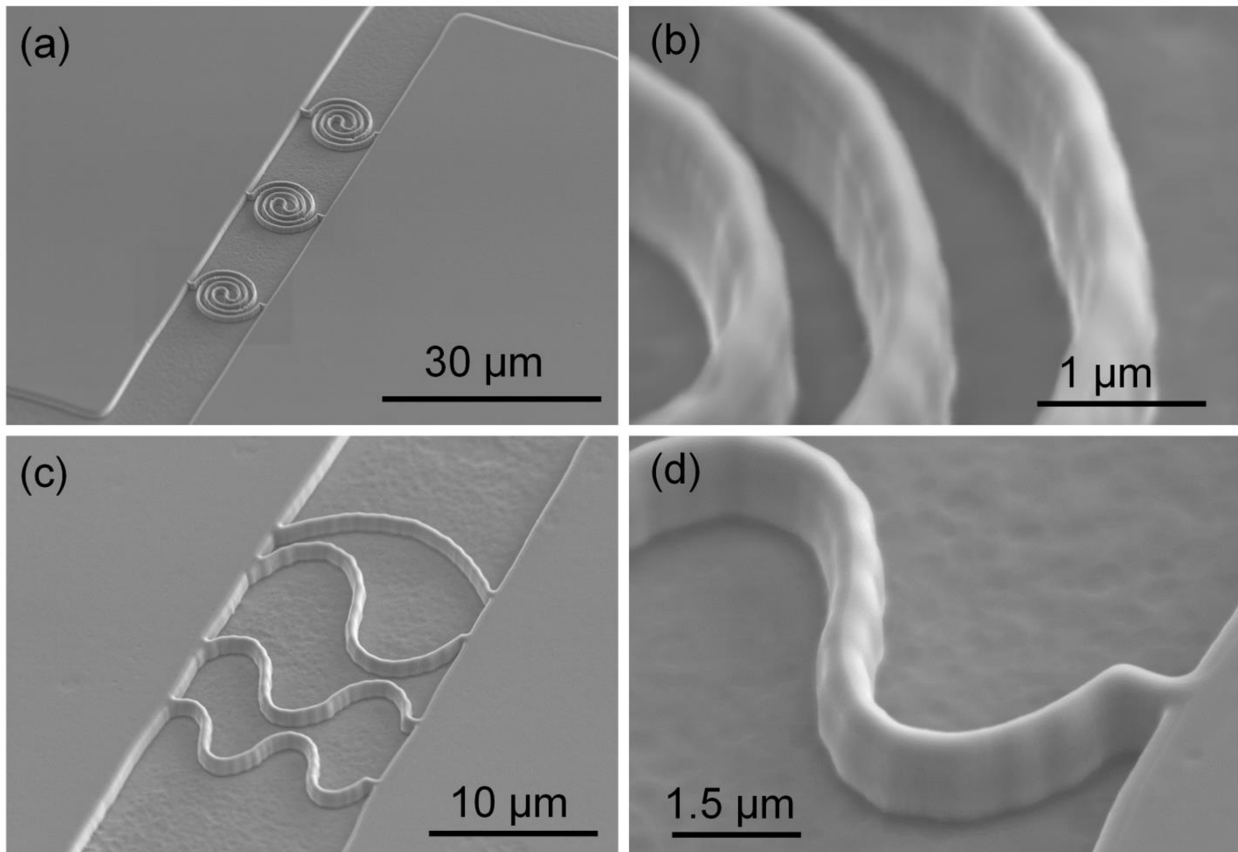

Figure 4.4 (a) SEM image of silicon mold for three spiral-shaped nanofluidic channel array fabricated by TBN; (b) Zoomed-in view of a section of one spiral-shaped nanofluidic channel mold; (c) SEM image of silicon mold for an array of four wavy shapes of nanofluidic channel with half, one, one and a half, and two full waves; (d) Zoomed-in view of the silicon mold for the wavy shapes of nanofluidic channel.

4.3 Results and Discussion

In this TBN process, the nanofluidic channel depth is determined by the silicon mold height, which can be adjusted by changing the etching duration. The nanofluidic channel width is determined by the width of the PS nanowires deposited using the heated AFM tip, which is usually in the range of several hundred nanometers [30]. To reduce the nanofluidic channel width, we thinned the silicon features using thermal oxidation of the silicon followed by BHF etching. This thinning process also helps reduce the sidewall roughness of the silicon structure etched by the Bosch process. Figure 4.5 shows the silicon mold structure before and after the thinning down. Figure 4.5(a, b) shows the SEM image of the silicon mold after DRIE etching; the silicon mold has a width about 500 nm and scallops are clearly visible. Figure 4.5(c, d) shows the SEM image of the silicon mold after 20 min oxygen plasma treatment, 200 nm thermal oxidation, and BHF etching. The silicon mold width reduced to about 370 nm, and the sidewall surface roughness was significantly reduced.

One important characteristic of the nanofluidic channel is the ion transport behavior, particularly the influence of surface charges on the conductance of the nanofluidic channel [36-38]. We used a single curvy PDMS nanofluidic channel for the measurement of ion transport. First, potassium chloride (KCl) solutions were filled into channels via a plastic tube inserted on one of the through-hole on the PDMS channel with the use of a syringe pump. This filling process ended when both microfluidic channels and the nanofluidic channel were filled. Then we inserted two platinum wires into two through-holes residing on opposite sides of nanofluidic channel for electrical connections. We measured the current at different voltages stepping from -5 volts to 5 volts with a potentiostat (Gamry potentiostat Reference 600) as shown in Figure 4.6(a). In the experiment, KCl solutions with concentration ranging from 10 nM to 1 M were

used for different sets of current-voltage (I-V) measurements. By fitting the I-V curves, conductances of the nanofluidic channel at different KCl concentrations can be derived. Figure 6(b) shows the derived conductances of the nanofluidic channel at different KCl concentrations represented by the black triangles.

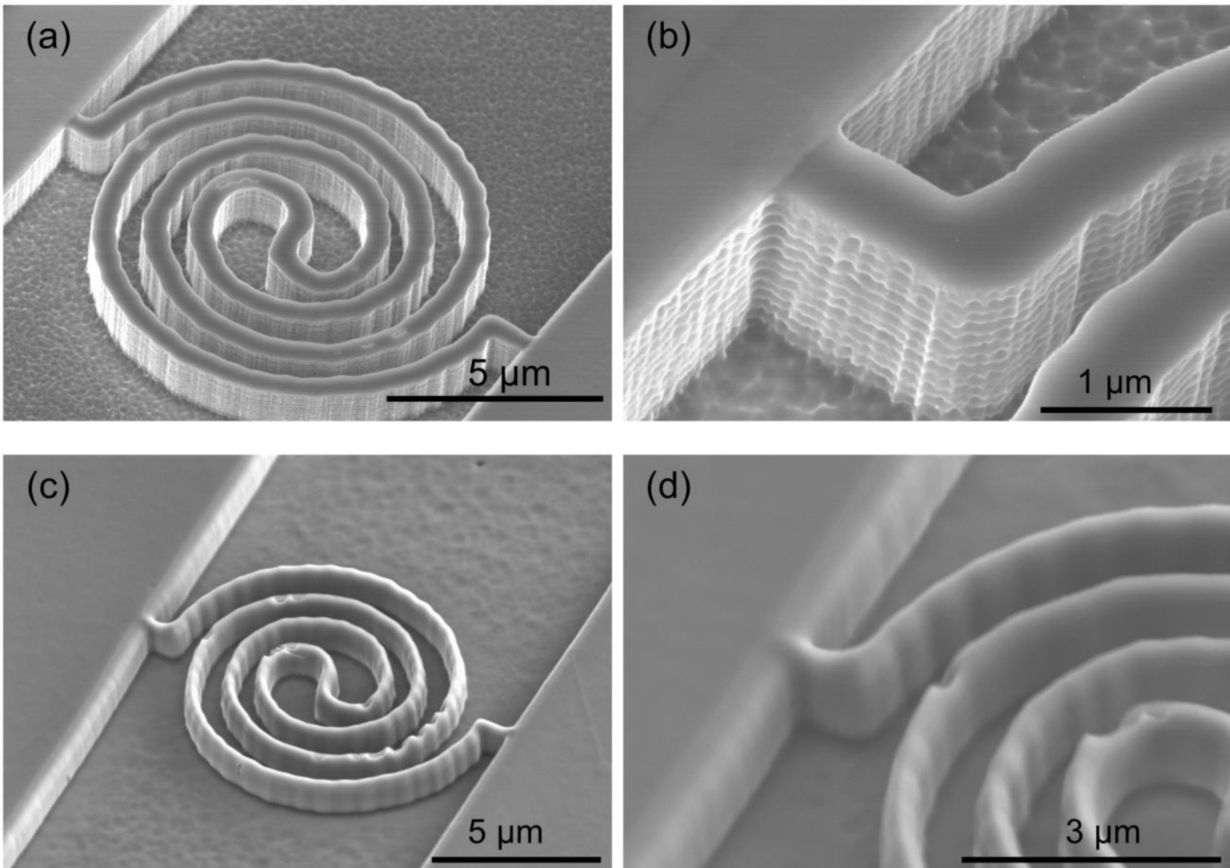

Figure 4.5 (a) SEM of a spiral-shaped silicon mold that was fabricated using TBN and Bosch etch; (b) A zoomed-in view of a section of the silicon mold. The scallops are visible on the sidewall of the silicon mold; the width of the silicon mold is about 500 nm; (c) SEM image of the same spiral-shaped silicon mold that is thinned down using 200 nm oxidation and BHF etching; (d) Zoomed-in view of a section of the silicon mold. The scallops are removed by the thinning down process. The width of the silicon mold after thinning down reduces to 300 nm.

In our experiment, I-V measurement started after both microfluidic channels sitting at opposite ends of the nanofluidic channel were filled and fluidic flow through the nanofluidic channel stopped. Therefore, the electric current was mostly contributed by the ion migrations inside the nanofluidic channel. The conductance G of a nanofluidic channel can be simplified as Equation 4.1 as shown below [39]:

$$G = q(\mu_k + \mu_{Cl})n_b \frac{WH}{L} + 2\mu_K \sigma_s \frac{W}{L} \tag{4.1}$$

where μ_k and μ_{Cl} are the mobility of potassium ion and chloride ion, σ_s is the nanofluidic channel surface charge density. W, H, and L are the nanofluidic channel width, height and length, and n_b is the ion density of the solutions. The first term in Equation 4.1 is due to bulk ion concentration while the second term is due to ions induced by the channel surface charges. At high ion concentrations, the surface charges in a nanofluidic channel are shielded by the mobile ions and have negligible influence on the ion conductance; therefore, the conductance is determined by the bulk concentration. At low ion concentrations, surface charge governs the ion concentration inside the nanofluidic channel, thus dominating the ion conductance.

The nanofluidic channel used in this I-V measurement has a width of 400 nm, a height of 400 nm and a length of 12 μm. To calculate the surface charge density, we chose μ_k to be 7.619×10^{-8} $m^2/V\cdot s$ and μ_{Cl} to be 7.912×10^{-8} $m^2/V\cdot s$ [39]. Based on the experiment data, we derived the surface charge density σ_s to be 0.22 C/m^2, close to the reported values of surface charge density of 0.1 C/m^2 for silicon dioxide [11, 36]. Figure 4.6(b) shows the simulation curve based on Equation 4.1 as represented by the solid black dash dot curve. As the KCl concentration decreases from 1 M to 1 mM, the nanofluidic channel conductance decreases proportionally to the KCl concentration. As the KCl concentration keeps on decreasing below 10 μM, the nanofluidic channel conductance stops decreasing proportionally to the KCl concentration and

starts to saturate, which is a typical behavior widely observed in nanofluidic channels due to the influence of surface charges on the channel walls [9, 10, 39].

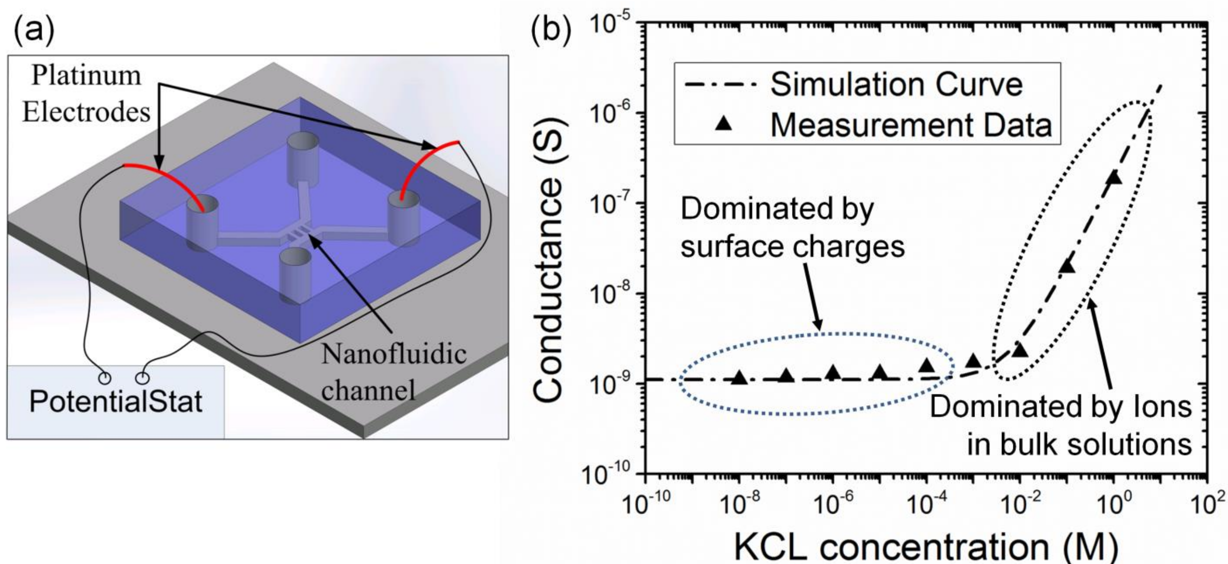

Figure 4.6 (a) Schematic showing the measurement setup for the current-voltage measurement of PDMS nanofluidic channels; (b) Measured and modeled nanofluidic channel conductance at different KCl concentrations.

Fluorescence microscopy on the single curved PDMS nanofluidic channel was employed to verify the functionality of the nanofluidic channel. First, nanofluidic channel was manually filled with a fluorescent dye (LD-700, Exciton, Inc.) that was diluted with deionized water to a concentration of the 0.5 mg/mL using a syringe. The fluorescence dye has a peak absorption wavelength of 647 nm and a peak emission wavelength of 673 nm. Then we used a HeNe laser with wavelength of 655 nm as the excitation laser and used an inverted microscope (Carl Zeiss Axio Observer Z1) imaging system equipped with a CCD camera (Photometrics Cascade) to capture the fluorescence microscopy images and then processed the images with a computational software (Matlab, Mathworks). Figure 4.7(a, b) shows the bright field microscope images of the

nanofluidic channel interfacing two microfluidic channels. Figure 4.7(c, d) are the fluorescence images of the nanofluidic channel showing that the nanofluidic channel was filled with fluorescence dyes, demonstrating the integrity of the nanofluidic channel fabricated by our TBN process.

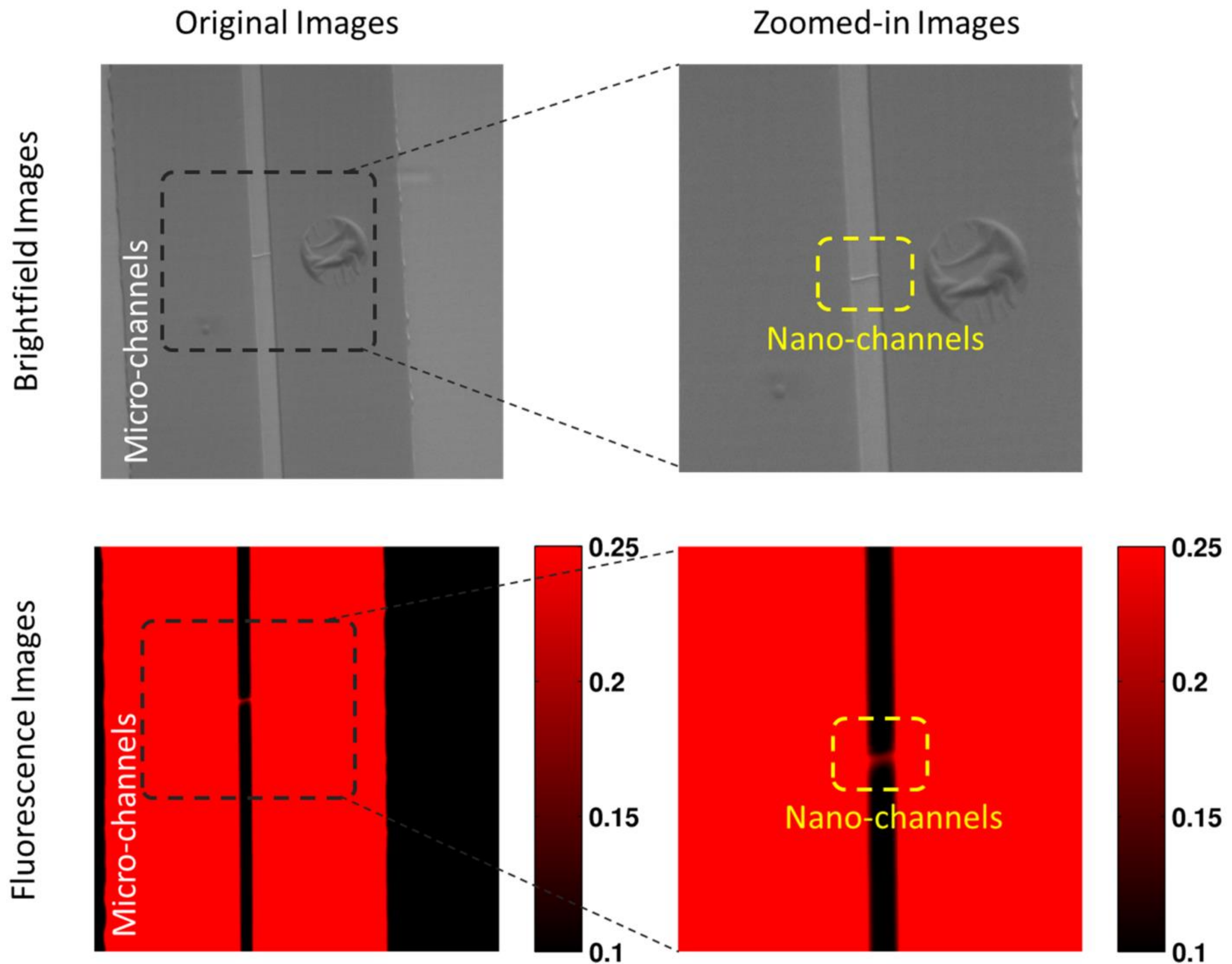

Figure 4.7 Bright field microscope images and corresponding fluorescence images of a single curved PDMS nanofluidic channel interfacing with two microfluidic channels.

4.4 Conclusions

In conclusion, this chapter presents the fabrication of PDMS nanofluidic channels using a heated AFM tip. The heated AFM tip deposited PS nanowires on silicon to serve as etch mask to

fabricate silicon molds for nanofluidic channels through one step of dry etching. Then PDMS nanofluidic channels were fabricated using the silicon mold through replicate molding. We integrated this TBN method with standard nanofabrication process seamlessly to fabricate nanofluidic channel with two interfacing microfluidic channels defined by conventional optical lithography. Both ion conductance measurement and fluorescence imaging were carried out on one of the fabricated nanofluidic channels for demonstrating the functionality. This TBN method of fabricating nanofluidic channels is rapid, low-cost and has the potential of scaling up for massive production of nanofluidic channels. Moreover, this TBN method can create arbitrary shapes of nanofluidic channels and is seamlessly compatible with existing nanofabrication processes, which makes this method suitable for producing highly-integrated lab-on-chip nanofluidic devices with complex structures such as a funnel [40].

4.5 References

[1] J. Han and H. G. Craighead, "Separation of long DNA molecules in a microfabricated entropic trap array," *Science,* vol. 288, pp. 1026-1029, May 12 2000.

[2] R. Riehn*, et al.*, "A nanofluidic railroad switch for DNA," *Nano Letters,* vol. 6, pp. 1973-1976, Sep 13 2006.

[3] J. Han and H. G. Craighead, "Entropic trapping and sieving of long DNA molecules in a nanofluidic channel," *Journal of Vacuum Science & Technology a-Vacuum Surfaces and Films,* vol. 17, pp. 2142-2147, Jul-Aug 1999.

[4] L. J. Guo*, et al.*, "Fabrication of size-controllable nanofluidic channels by nanoimprinting and its application for DNA stretching," *Nano Letters,* vol. 4, pp. 69-73, Jan 2004.

[5] D. J. Bonthuis, *et al.*, "Conformation and dynamics of DNA confined in slitlike nanofluidic channels," *Physical Review Letters,* vol. 101, Sep 5 2008.

[6] Y. C. Wang, *et al.*, "Million-fold preconcentration of proteins and peptides by nanofluidic filter," *Analytical Chemistry,* vol. 77, pp. 4293-4299, Jul 15 2005.

[7] B. R. Cipriany, *et al.*, "Single Molecule Epigenetic Analysis in a Nanofluidic Channel," *Analytical Chemistry,* vol. 82, pp. 2480-2487, Mar 15 2010.

[8] W. Reisner, *et al.*, "Single-molecule denaturation mapping of DNA in nanofluidic channels," *Proceedings of the National Academy of Sciences of the United States of America,* vol. 107, pp. 13294-13299, Jul 27 2010.

[9] H. Daiguji, *et al.*, "Ion transport in nanofluidic channels," *Nano Letters,* vol. 4, pp. 137-142, Jan 2004.

[10] D. Stein, *et al.*, "Surface-charge-governed ion transport in nanofluidic channels," *Physical Review Letters,* vol. 93, Jul 16 2004.

[11] R. Karnik, *et al.*, "Electrostatic control of ions and molecules in nanofluidic transistors," *Nano Letters,* vol. 5, pp. 943-948, May 2005.

[12] I. Vlassiouk and Z. S. Siwy, "Nanofluidic diode," *Nano Letters,* vol. 7, pp. 552-556, Mar 2007.

[13] T. C. Kuo, *et al.*, "Gateable nanofluidic interconnects for multilayered microfluidic separation systems," *Analytical Chemistry,* vol. 75, pp. 1861-1867, Apr 15 2003.

[14] P. Mao and J. Y. Han, "Fabrication and characterization of 20 nm planar nanofluidic channels by glass-glass and glass-silicon bonding," *Lab on a Chip,* vol. 5, pp. 837-844, 2005.

[15] J. Haneveld*, et al.*, "Wet anisotropic etching for fluidic 1D nanochannels," *Journal of Micromechanics and Microengineering,* vol. 13, pp. S62-S66, Jul 2003.

[16] W. Sparreboom*, et al.*, "Rapid sacrificial layer etching for the fabrication of nanochannels with integrated metal electrodes," *Lab on a Chip,* vol. 8, pp. 402-407, 2008.

[17] J. C. T. Eijkel*, et al.*, "1-D nanochannels fabricated in polyimide," *Lab on a Chip,* vol. 4, pp. 161-163, 2004.

[18] C. K. Harnett*, et al.*, "Heat-depolymerizable polycarbonates as electron beam patternable sacrificial layers for nanofluidics," *Journal of Vacuum Science & Technology B,* vol. 19, pp. 2842-2845, Nov-Dec 2001.

[19] D. M. Cannon*, et al.*, "Fabrication of single nanofluidic channels in poly(methylmethacrylate) films via focused-ion beam milling for use as molecular gates," *Applied Physics Letters,* vol. 85, pp. 1241-1243, Aug 16 2004.

[20] X. G. Liang*, et al.*, "Single sub-20 nm wide, centimeter-long nanofluidic channel fabricated by novel nanoimprint Mold fabrication and direct imprinting," *Nano Letters,* vol. 7, pp. 3774-3780, Dec 2007.

[21] S. M. Park*, et al.*, "A method for nanofluidic device prototyping using elastomeric collapse," *Proceedings of the National Academy of Sciences of the United States of America,* vol. 106, pp. 15549-15554, Sep 15 2009.

[22] S. Chung*, et al.*, "Non-lithographic wrinkle nanochannels for protein preconcentration," *Advanced Materials,* vol. 20, pp. 3011-3016, Aug 18 2008.

[23] D. M. Kolb*, et al.*, "Nanofabrication of small copper clusters on gold(111) electrodes by a scanning tunneling microscope," *Science,* vol. 275, pp. 1097-1099, Feb 21 1997.

[24] I. W. Lyo and P. Avouris, "Field-Induced Nanometer-Scale to Atomic-Scale Manipulation of Silicon Surfaces with the STM," *Science,* vol. 253, pp. 173-176, Jul 12 1991.

[25] S. W. Hla*, et al.*, "Inducing all steps of a chemical reaction with the scanning tunneling microscope tip: Towards single molecule engineering," *Physical Review Letters,* vol. 85, pp. 2777-2780, Sep 25 2000.

[26] A. A. Tseng, "Advancements and challenges in development of atomic force microscopy for nanofabrication," *Nano Today,* vol. 6, pp. 493-509, Oct 2011.

[27] S. Somnath*, et al.*, "Parallel nanoimaging and nanolithography using a heated microcantilever array," *Nanotechnology,* vol. 25, Jan 10 2014.

[28] S. A. Harfenist*, et al.*, "Direct drawing of suspended filamentary micro- and nanostructures from liquid polymers," *Nano Letters,* vol. 4, pp. 1931-1937, Oct 2004.

[29] L. Pellegrino*, et al.*, "(Fe,Mn)3O4 Nanochannels Fabricated by AFM Local-Oxidation Nanolithography using Mo/Poly(methyl methacrylate) Nanomasks," *Advanced Materials,* vol. 18, pp. 3099-3104, 2006.

[30] H. Huan*, et al.*, "Fabrication of arbitrarily shaped silicon and silicon oxide nanostructures using tip-based nanofabrication," *Journal of Vacuum Science & Technology B,* vol. 31, p. 06FJ01, 2013.

[31] R. F. Jonathan*, et al.*, "Nanometer-scale flow of molten polyethylene from a heated atomic force microscope tip," *Nanotechnology,* vol. 23, p. 215301, 2012.

[32] S. Somnath*, et al.*, "Improved Nanotopography Sensing via Temperature Control of a Heated Atomic Force Microscope Cantilever," *Sensors Journal, IEEE,* vol. 11, pp. 2664-2670, 2011.

[33] H. Huan, *et al.*, "Nano-fabrication with a flexible array of nano-apertures," *Nanotechnology,* vol. 23, p. 175303, 2012.

[34] E. P. Chan and A. J. Crosby, "Fabricating Microlens Arrays by Surface Wrinkling," *Advanced Materials,* vol. 18, pp. 3238-3242, 2006.

[35] D. Breid and A. J. Crosby, "Surface wrinkling behavior of finite circular plates," *Soft Matter,* vol. 5, pp. 425-431, 2009.

[36] D. Stein, *et al.*, "Surface-Charge-Governed Ion Transport in Nanofluidic Channels," *Physical Review Letters,* vol. 93, p. 035901, 2004.

[37] H. Daiguji, *et al.*, "Ion Transport in Nanofluidic Channels," *Nano Letters,* vol. 4, pp. 137-142, 2004/01/01 2003.

[38] J. C. T. Eijkel and A. van den Berg, "Nanofluidics: what is it and what can we expect from it?," *Microfluidics and Nanofluidics,* vol. 1, pp. 249-267, Jul 2005.

[39] L.-J. Cheng, *Ion and molecule transport in nanochannels*: ProQuest, 2008.

[40] J. M. Perry, et al., "Ion Transport in Nanofluidic Funnels," ACS Nano, vol. 4, pp. 3897-3902, Jul 2010.

CHAPTER 5: SILICON METAL-SEMICONDUCTOR FIELD EFFECT TRANSISTORS FABRICATED BY TIP-BASED NANOFABRICATION

5.1 Introduction

Field effect transistors (FET) are the basic components for modern electronics. Shrinking the size of the FET has been going on for many years following Moore's law. The state-of-the-art FETs are fabricated using very expensive equipment such as deep-UV lithography system. However, even with these advanced lithography tools, the dimensions of the FET are still limited by the optical diffraction, currently 50 nm for the deep UV. As Moore's law continues, it is possible that the optical lithography technology might reach its limit. Therefore, it is important to look for alternative methods for fabricating FET devices.

Tip-based nanofabrication (TBN) uses a nanometer scale tip to interact with the substrate to define nanoscale features through a number of mechanisms such as manipulation, mechanical scratch, chemical diffusion, thermal indentation, thermal deposition, electrochemical reaction, plasma, etc. Up to now, there are only a few reports of using TBN for fabricating FET devices such as oxidation-based TBN [1-3]. However, one challenge of oxidation-based TBN is that the feature size is dependent on many factors such as humidity, force between the tip and substrate, voltages etc. It is difficult to scale up for volume production of transistors due to the uniformity issue.

Here, we present a reliable tip-based nanofabrication (TBN) method for fabricating silicon metal-semiconductor field effect transistor (MESFET) devices using a heated AFM tip. We used a heated AFM tip to deposit dense polymer nanowires that served directly as etch mask to

fabricate silicon fin through one step of etching. Then source, drain and gate were fabricated using conventional optical lithography. This TBN process is seamlessly compatible with existing nanofabrication methods because the deposited polymer can be combined with optical lithography patterned silicon oxide together to serve as etch mask. Moreover, we measured the I-V curves of the TBN-fabricated MESFET and obtained reasonable performance.

5.2 Experiment

MESFETs use a Schottkey metal-semiconductor junction for modulating the conducting channel. They are widely used for microwave frequency communications [4-7] and radar applications. In contrast to the MOSFET, MESFETs have no insulator between the gate and the active region.

Figure 5.1 shows the major fabrication process for the silicon MESFET using TBN. First, we fabricated 150 nm thick silicon oxide doping windows for source and drain region on top of a silicon-on-insulator (SOI) wafer using conventional lithography and wet etching (step a). Then we doped the source and drain region through the doping windows using boron diffusion. The boron diffusion was performed for 15 min in a 950 °C furnace with N_2 atmosphere, followed up by 40 seconds etching of borosilicate glass using 10:1 DI water to HF, 10 min oxidation using 1:1 H_2SO_4: HNO_3, and finally 40 s dipping into 10:1 DI water to HF.

Then we deposited 200 nm thick PECVD silicon oxide on top of the sample and patterned the etch mask for source and drain region using conventional lithography and wet etching of PECVD silicon oxide (step b). We then deposited polystyrene (PS) nanowires across the etch mask of source and drain using the heated AFM tip at 260°C with a tip scan speed of 150 nm/s (step c). After deposition of PS, we etched the top silicon using the patterned PECVD oxide as

well as the PS nanowires as etch mask, and transferred the patterns to the top silicon (step e). This step defines the geometry of source, drain and the fin. We then fabricated aluminum source and drain contact pads using metal lift-off process (step f). To ensure good ohmic contact, we annealed the sample at 400 °C furnace for 10 min in a N_2 atmosphere. The last step is to fabricate aluminum gate electrode using metal lift-off method. Because a Schottkey contact is desired between the silicon fin and the aluminum gate, so there is no annealing step after the metal lift-off step.

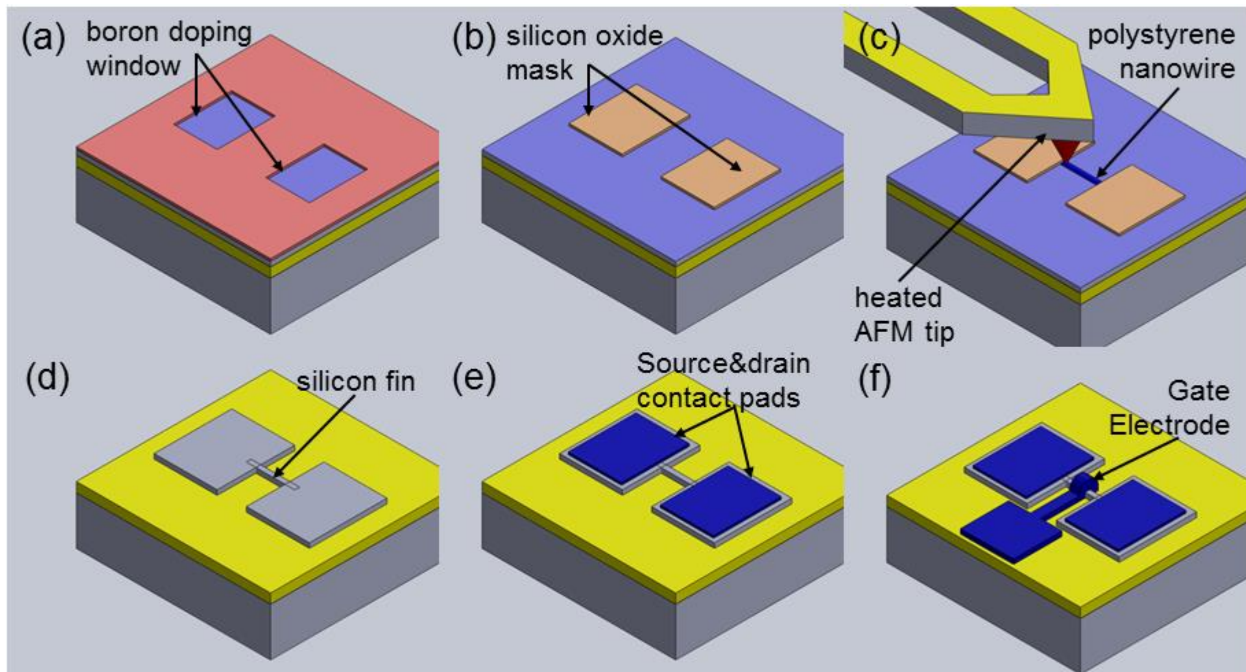

Figure 5.1 Schematics of major steps in the TBN process for fabricating nanofluidic channels. (a) Fabricate doping windows of source and drain on top silicon using conventional optical microlithography and wet hydrofluoric acid etching; (b) Define silicon oxide mask for source and drain area using 2nd optical lithography BHF etching; (c) Deposit polystyrene (PS) nanowires using a heated AFM tip across two oxide mask for source and drain area; (d) Etch top silicon using both silicon oxide and PS nanowires as etch mask; (e) Fabricate source and drain contact pads using the 3th lithography, aluminum sputtering and lift off; (f) Fabricate gate electrode using the 4th lithography, aluminum evaporating and lift off.

5.3 Results and Discussion

Figure 5.2 shows the SEM image of first generation of fabricated silicon MESFET. From (a) to (d), MESFETS with one, two, four, eight fins were fabricated.

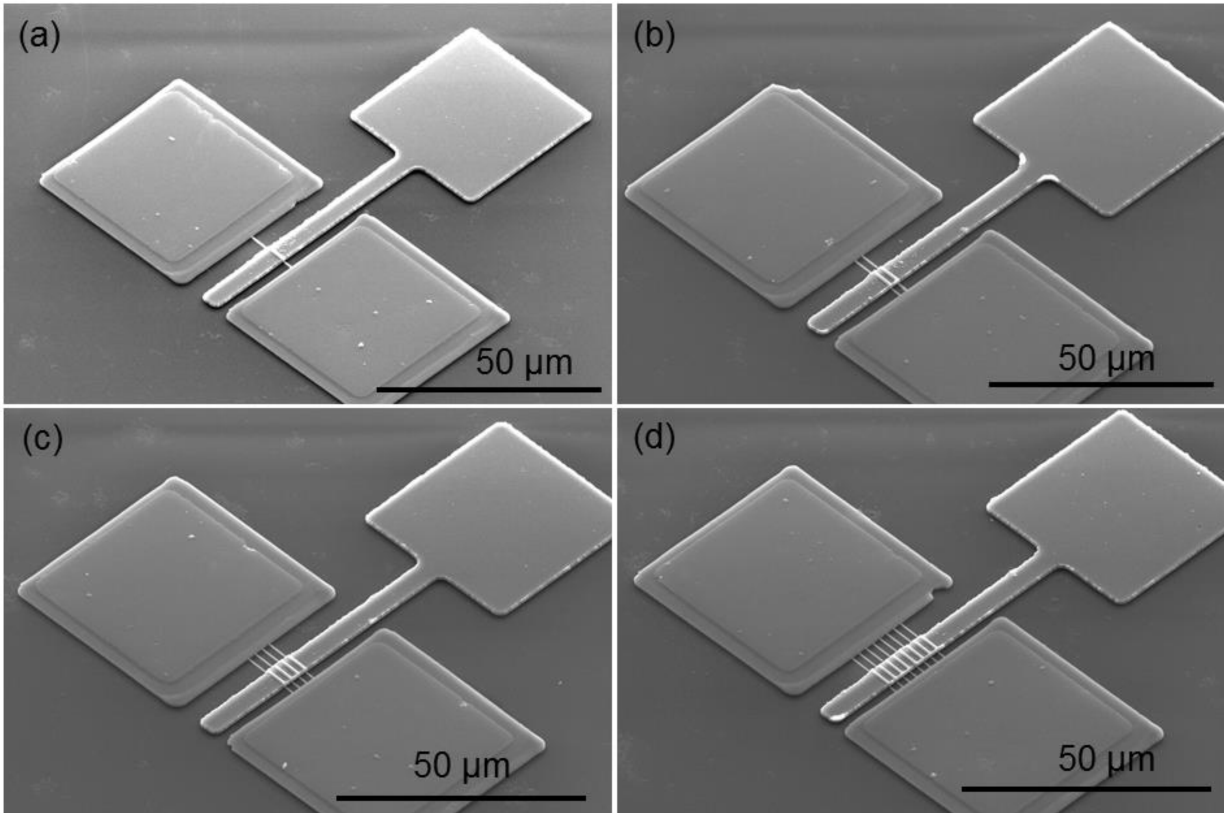

Figure 5.2 SEM images of TBN-fabricated MESFETs with one, two, four and eight fins.

The first generation of transistors exhibited very poor performance. The source-drain current was very small. Figure 5.3 shows the zoomed-in view of the gate electrode. Voids were observed between the aluminum gate and the silicon fin. Because the silicon fin is almost rectangular, and we used evaporation of aluminum at a pressure of 10^{-6} Torr, the aluminum film was not conformal on top of the silicon fins; therefore, some gaps formed between the aluminum and the silicon fin.

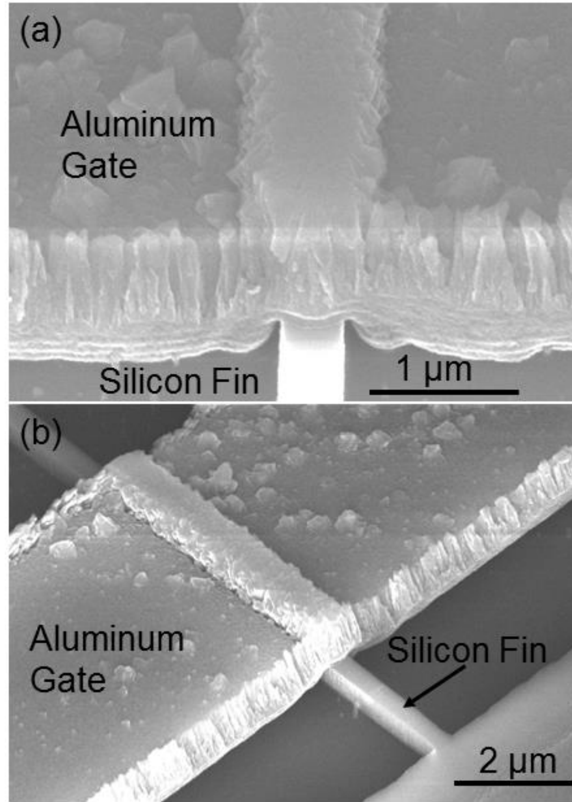

Figure 5.3 (a) Zoomed-in view of the aluminum gate on top of the silicon fin; (b) titled view of the aluminum gate on top of the silicon fin.

To solve this issue, we optimized the process conditions. First, we added a step of silicon fin oxidation and BHF etching step before gate electrode fabrication, which reduced the fin width and rounded the rectangular shape to facilitate conformal coating; second, we replaced aluminum evaporation with physical sputtering, in which aluminum atoms more uniformly coated the silicon fin due to the shorter mean free path length because of the higher pressure.

Figure 5.4 shows the SEM images of the second generation of TBN-fabricated silicon MESFET devices with single and dual fins. Figure 5.4(a,b) shows a single-fin MESFET. The length of the fin is about 13.6 μm, the width is 400 nm and the height is 500 nm. Figure 5.4(c,d) shows SEM images of a dual-fin MESFET. The geometry of the two-fin transistors is the same

as the single-fin MESFET. MESFET devices in this second generation have better gate coverage on the silicon fins.

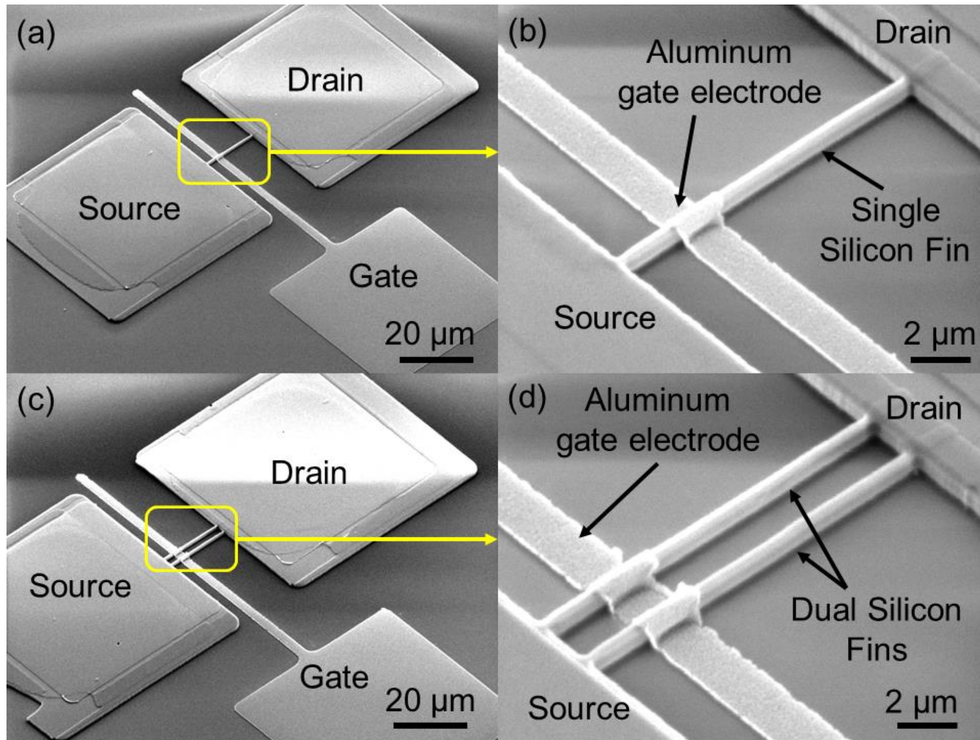

Figure 5.4 SEM images of TBN-fabricated devices with better aluminum gate coverage over silicon fins.

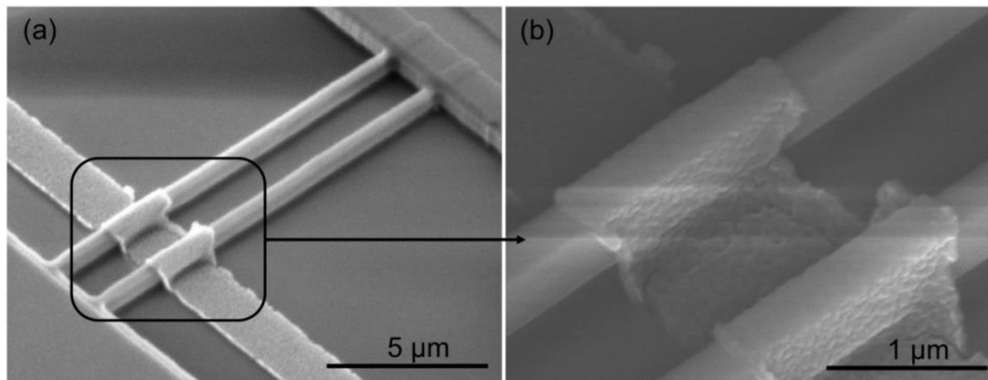

Figure 5.5 zoomed-in view of SEM images of aluminum gates atop silicon fins.

Figure 5.6 shows the measurement of both gate leak current and source and drain current versus different gate-source bias for a single-fin TBN-fabricated MESFET as shown in Figure 5.4(a). Black curves represent gate leak current and blue curves represent source-drain current. The two

currents changes with gate-source bias V_{gs} at different V_{ds} values. The V_{ds} values for the four curves are -2. -1.5, -1, and -0.5 V. The black curve shows that the threshold voltage V_{gon}, defined as the voltage at which the gate starts to leak current, is measured to be around -0.4 volts for the aluminum and silicon Schottky contact. The threshold voltage V_{th}, defined as the voltage at which the channel starts to conduct current, is measured to be around -0.3 V. When V_{gs} decreases below -0.3 V, the channel starts to conduct current. As V_{gs} decreases, the channel starts to have more holes for conduct current, so the magnitude of I_{ds} increases. When V_{gs} reaches -0.6 V, the gate leak current increases so much that it takes over the current from the drain, which limits the working range of the MESFET.

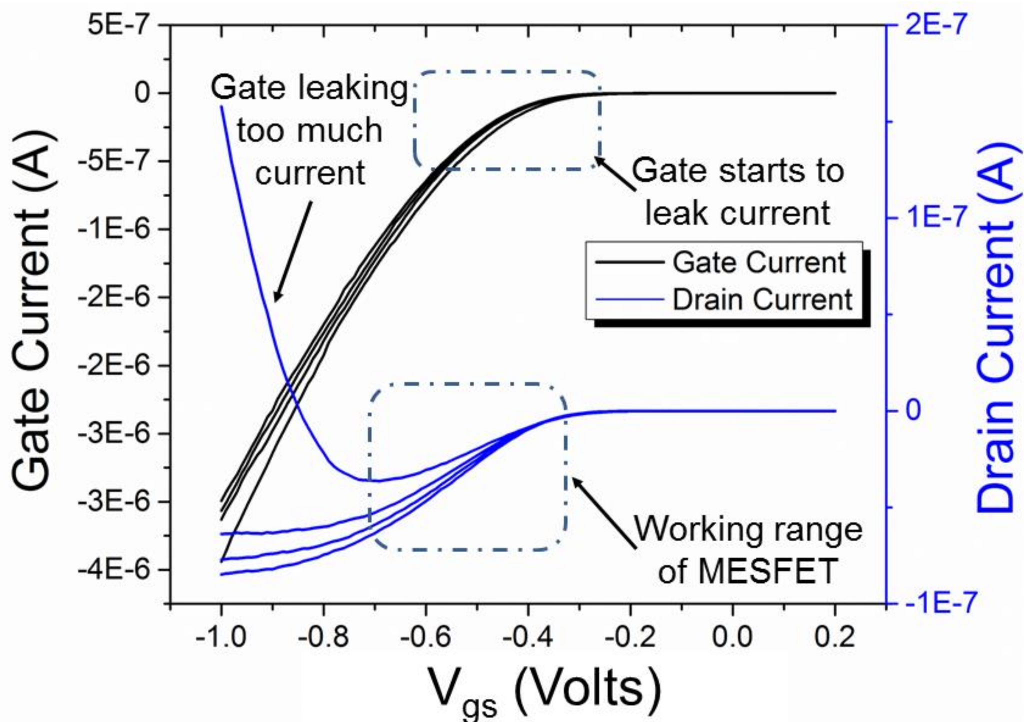

Figure 5.6 Measurement of Gate current represented by black curves and drain current represented by blue curves versus gate source bias V_{gs} at different V_{ds} settings for a single-fin MESFET. The black curve shows that the threshold voltage V_{gon}, defined as the voltage value under which the gate starts to leak current.

To improve the performance of the MESFET in terms of dynamic range, it is necessary to shift the V_{th} to the right, so V_{gs} within the normal operating range cannot cause the gate current to leak much. Since V_{gon} is a fixed value for a fixed metal to silicon, we can only shift the V_{th} to the right. V_{th} is given as equation 5.1, where q is the single electron charge, N_A is the doping concentration of the silicon fin, W_{fin} is the silicon fin width, and V_{bi} is the built-in potential at zero bias for the aluminum-silicon Schottky contact.

$$V_{th} = \frac{qN_A W_{fin}^{2}}{8\varepsilon_s} - V_{bi} \tag{5.1}$$

So either increasing the doping concentration N_A or increasing the width W_{fin} can increase V_{th}, Figure 5.7 shows the simulation of threshold voltage V_{th} at different doping concentrations N_A. The current doping concentration is around 3×10^{15} /cm^3, the simulated V_{th} is around -0.3 volts, matching the observed V_{th}. According to the simulation curve, to increase the V_{th} to 0.5 volts, we need about 3×10^{16} /cm^3 boron-doping concentration.

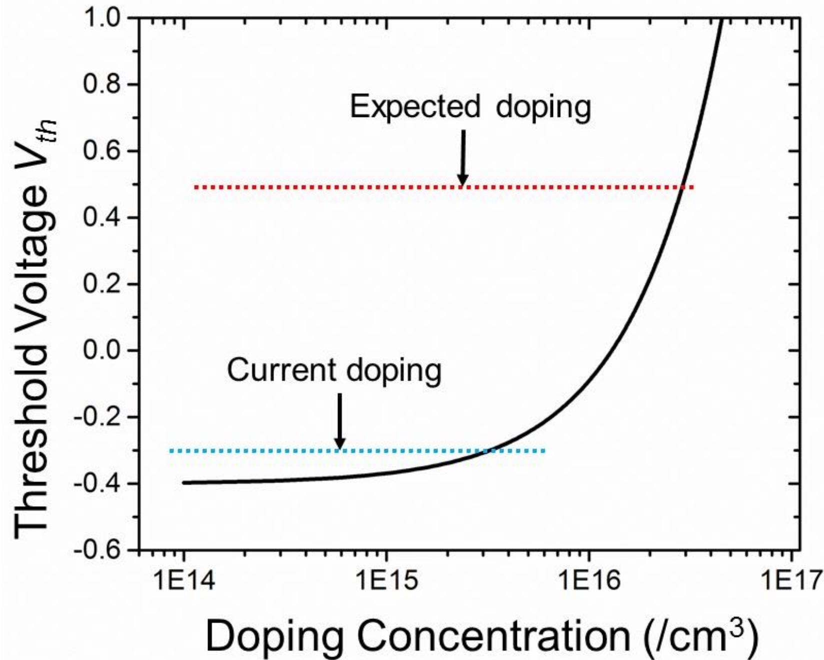

Figure 5.7 Simulation curves for threshold voltage versus different boron doping concentrations.

5.4 Conclusions

We have presented a TBN method for fabricating MESFET devices. In this TBN method, a heated AFM tip deposits polymer nanowires that serve as mask for transferring the geometry of polymer nanowires into silicon nanowires through one step of dry etching. This TBN method is seamlessly compatible with existing nanofabrication process for FET device applications. To demonstrate the capability of this TBN method, we fabricated MESFET devices with one, two, four, and eight silicon fins. I-V measurement showed the FET behavior of fabricated MESFET devices.

5.5 References

[1] R. V. Martinez*, et al.*, "Silicon nanowire circuits fabricated by AFM oxidation nanolithography," *Nanotechnology,* vol. 21, Jun 18 2010.

[2] J. Martinez*, et al.*, "Silicon Nanowire Transistors with a Channel Width of 4 nm Fabricated by Atomic Force Microscope Nanolithography," *Nano Letters,* vol. 8, pp. 3636-3639, Nov 2008.

[3] P. Campbell*, et al.*, "Fabrication of nanometer-scale side-gated silicon field effect transistors with an atomic force microscope," *Applied Physics Letters,* vol. 66, pp. 1388-1390, 1995.

[4] W. Lepkowski*, et al.*, "45 GHz silicon MESFETs on a 0.15 μm SOI CMOS process," in *SOI Conference, 2009 IEEE International*, 2009, pp. 1-2.

[5] S. A. Maas, "A GaAs MESFET mixer with very low intermodulation," *Microwave Theory and Techniques, IEEE Transactions on,* vol. 35, pp. 425-429, 1987.

[6] L. Yin*, et al.*, "Improved breakdown voltage in GaAs MESFETs utilizing surface layers of GaAs grown at a low temperature by MBE," *Electron Device Letters, IEEE,* vol. 11, pp. 561-563, 1990.

[7] T. Kimura*, et al.*, "Subhalf-Micron Gate GaAs Mesfet Process Using Phase-Shifting-Mask Technology," in *Gallium Arsenide Integrated Circuit (GaAs IC) Symposium, 1991. Technical Digest 1991., 13th Annual*, 1991, pp. 281-284.

CHAPTER 6: CONCLUSIONS AND FUTURE WORK

This dissertation explores the use of a heated AFM tip for fabrication of NEMS devices. Two critical challenges hindering TBN from NEMS fabrication are addressed in this thesis. First, we demonstrated reliable fabrication of nanostructures of solid-state materials such as silicon and silicon oxide, paving the first step for NEMS fabrication using TBN; second, we developed a process that makes this TBN method seamlessly compatible with conventional nanofabrication process.

After solving the two critical challenges, we demonstrated various types of silicon NEMS mechanical resonators such as single-clamped, double-clamped, wavy-shaped, spider-like and spiral-shaped using this TBN method with a heated AFM tip. Laser interferometer measured two NEMS resonators to have resonance frequency of 1.2MHz and 2.2 MHz, close to the simulated resonance frequency.

Moreover, we demonstrated PDMS nanofluidic channels with arbitrary shapes using this TBN method with a heated AFM tip. Both ion conductance measurement and fluorescence measurement confirmed the functionality of the TBN-fabrication nanofluidic channels.

Finally, we demonstrated a MESFET transistor using this TBN method with a heated AFM tip. MESFET device with one, two, four and eight fins are fabricated, demonstrating the capability of this TBN method. I-V measurements proved the functionality of the transistor.

6.1 Future Work

This thesis presented reliable fabrication of NEMS device using a single heated AFM tip. In order to use this TBN method as a commercial fabrication method for NEMS devices, additional work needs to be done in at least two directions.

The first direction is to improve the automation and throughput of this TBN method. Currently, the inking process of adding the polymer to the heated AFM tip is manual. After using up the polymer on the tip, the heated AFM tip needs to be removed from the AFM equipment and loaded to a manual stage for polymer inking. This manual inking process reduces the degree of automation of this TBN method and limits the throughput. One possible solution to this problem might be to develop a new generation of heated AFM tip with automatic inking function. Figure 6.1 shows a conceptual design of this auto-inking heated AFM tip. Instead of a regular double-armed design, a third delivering arm is added. The delivering arm is designed to have a thermal gradient that drives molten polymer from high temperature at the base to the low temperature at the tip using thermal marangoni force [1, 2].

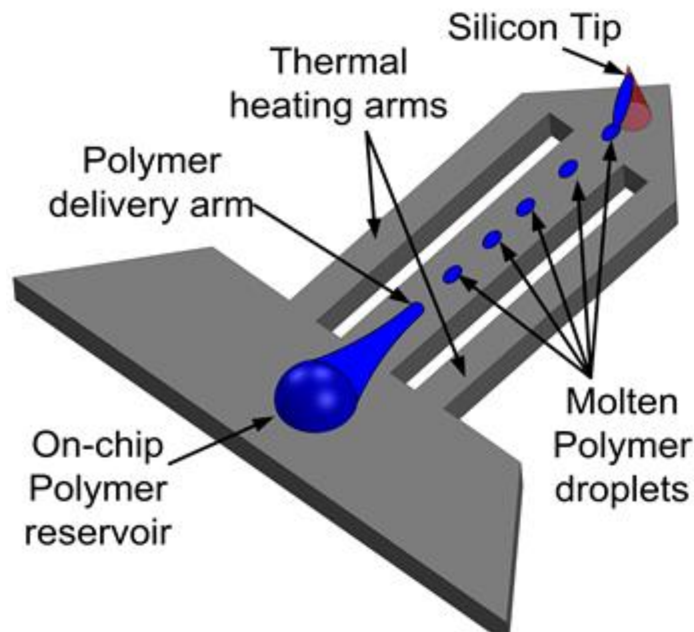

Figure 6.1 Schematics showing a heated AFM tip with automatic inking function.

The second direction is to address the scalability. Several multi-tip TBN systems have been demonstrated [3-6]. However, in order to use TBN for mass-production of NEMS devices, thousands or even millions of tips need to be operating individually to deposit polymers. Figure

6.2 shows a conceptual design of millions of thermal AFM tips arrayed for depositing polymer nanowires. The AFM tip is not made of silicon but of polymer such as PDMS. Au tip is fabricated on each of the polymer tip [6]. Laser beams shooting from the base of the polymer tip can induce plasmonic heating on the Au tip, thus melting the polymer on the tip, and depositing polymer nanowires. The laser beam can address each tip from the base.

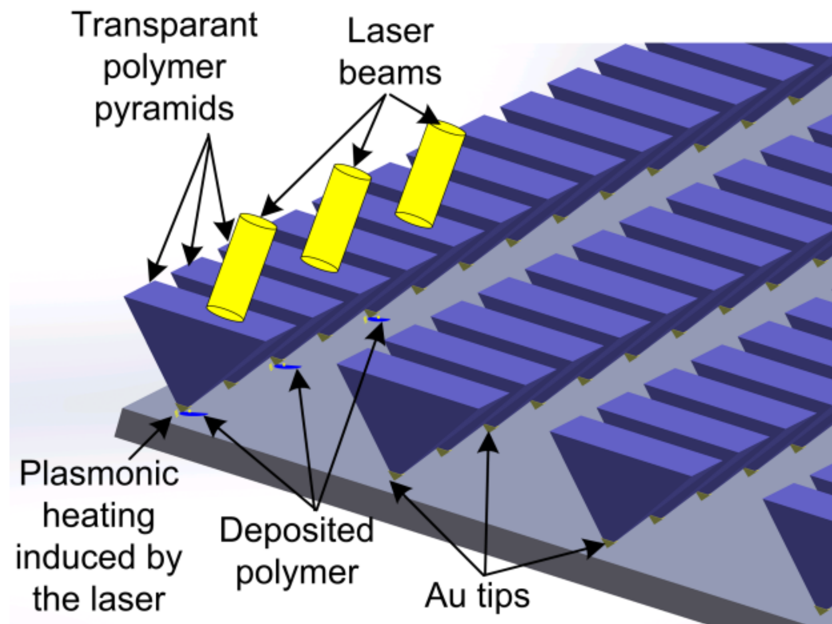

Figure 6.2 Schematics of million tips heated by laser induced plasmon resonance in Au tip.

Another important future direction is to explore the use of heated AFM tip for patterning on non-flat substrate. For example, the AFM tip is able to deposit on top of a curved substrate or patterned substrate. Figure 6.3 shows an AFM topography image of a deposited polystyrene nanodot on a photonic crystal surface [7]. This additive method has advantages over EBL because no contamination can be introduced. EBL requires ebeam resist covering everywhere on the surface, which is not desired for many applications that require clean surfaces.

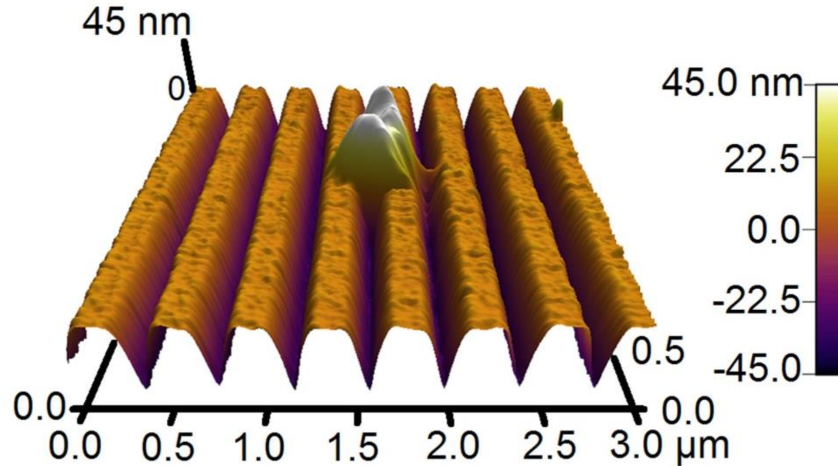

Figure 6.3 AFM topography image of a polystyrene nanodot deposited by a heated AFM tip on top of a photonic crystal surface.

6.2 References

[1] R. Farahi, A. Passian, T. Ferrell and T. Thundat, "Microfluidic manipulation via Marangoni forces," *Applied physics letters,* vol. 85, pp. 4237-4239, 2004.

[2] R. Farahi, A. Passian, S. Zahrai, A. Lereu, T. Ferrell and T. Thundat, "Microscale Marangoni actuation: all-optical and all-electrical methods," *Ultramicroscopy,* vol. 106, pp. 815-821, 2006.

[3] S. Suhas, K. Hoe Joon, H. Huan and P. K. William, "Parallel nanoimaging and nanolithography using a heated microcantilever array," *Nanotechnology,* vol. 25, p. 014001, 2014.

[4] P. Vettiger, M. Despont, U. Drechsler, U. Durig, W. Haberle, M. I. Lutwyche, H. E. Rothuizen, R. Stutz, R. Widmer, and G. K. Binnig, "The “Millipede”—More than thousand tips for future AFM storage," *IBM Journal of Research and Development,* vol. 44, pp. 323-340, 2000.

[5] F. Huo, Z. Zheng, G. Zheng, L. R. Giam, H. Zhang and C. A. Mirkin, "Polymer pen lithography," *Science,* vol. 321, pp. 1658-1660, 2008.

[6] H. Hu, J. Yeom, G. Mensing, Y. Chen, M. A. Shannon and W. P. King, "Nano-fabrication with a flexible array of nano-apertures," *Nanotechnology,* vol. 23, p. 175303, 2012.

[7] Y. Zhuo, H. Hu, W. Chen, M. Lu, L. Tian, H. Yu, K. D. Long, E. Chow, W. P. King, S. Singamaneni, and B. T. Cunningham, "Single nanoparticle detection using photonic crystal enhanced microscopy," *Analyst,* vol. 139, pp. 1007-1015, 2014.